

INTERNATIONAL ATOMIC ENERGY AGENCY

INDC(BLR)-019
Distr. J+TU/EL

I N D C

INTERNATIONAL NUCLEAR DATA COMMITTEE

Neutron Data Evaluation of ^{231}Pa

V.M. Maslov¹, M. Baba²,
A. Hasegawa³, N.V. Kornilov^{1*}, A.B. Kagalenko^{1*},
N.A. Tetereva¹

- ¹⁾ Joint Institute of Nuclear and Energy Research – SOSNY
220109, Minsk-Sosny, Belarus
 - ²⁾ Cyclotron and Radioisotope Center, Tohoku University,
Sendai, Japan
 - ³⁾ Department of Nuclear Energy System, Tokai Research
Establishment, Japan Atomic Energy Research Institute,
Tokai-mura, Naka-gun, Ibaraki-ken
- *) Permanent address: Institute of Physics and Power Engineering,
249020, Obninsk, Russia

February 2004

Documents in the EL series are available in only limited quantities in hardcopy form. They may be downloaded in electronic form from http://www-nds.iaea.or.at/indc_sel.html or sent as an e-mail attachment. Requests for hardcopy or e-mail transmittal should be directed to services@iaeand.iaea.org or to:

Nuclear Data Section
International Atomic Energy Agency
PO Box 100
Wagramer Strasse 5
A-1400 Vienna
Austria

Produced by the IAEA in Austria
February 2004

Neutron Data Evaluation of ^{231}Pa

V.M. Maslov¹, M. Baba²,
A.Hasegawa³,N.V. Kornilov^{1,*}, A. B. Kagalenko^{1,*},
N.A. Tetereva¹

¹⁾ Joint Institute for Nuclear and Energy Research,
220109, Minsk-Sosny, Belarus

²⁾ Cyclotron and Radioisotope Center, Tohoku
University, Sendai, Japan

³⁾ Department of Nuclear Energy System, Tokai
Research Establishment, Japan Atomic Energy
Research Institute,Tokai-mura, Naka-gun, Ibaraki-ken

Abstract

Consistent evaluation of ^{231}Pa measured data base is performed. Hauser-Feshbach-Moldauer theory, coupled channel model and double-humped fission barrier model are employed. Total, differential scattering, fission and (n,xn) data are calculated, using fission cross section data description as a major constraint. The direct excitation of ground state band levels is calculated within rigid rotator model. Average resonance parameters are provided, which reproduce evaluated cross sections in the range of 115 eV -78 keV.

This work is performed under the Project Agreement B-404 with the International Science and Technology Center (Moscow). The Financing Party for the Project is Japan.

^{*}) Permanent address: Institute of Physics and Power Engineering, 249020, Obninsk, Russia

Contents

1	Introduction	5
2	Resolved resonance energy range	5
3	Unresolved resonance region	7
3.1	Average resonance parameters	7
3.1.1	Neutron resonance spacing	7
3.1.2	Neutron width	8
3.1.3	Radiative capture width	8
3.1.4	Neutron inelastic width	8
3.1.5	Fission width	8
3.2	Average cross sections in the region .115-77 keV	9
3.2.1	Total cross section	9
3.2.2	Elastic scattering cross section	9
3.2.3	Fission cross section	9
3.2.4	Capture cross section	10
3.2.5	Inelastic scattering cross section	10
3.2.6	Comparison of average resonance parameters	10
4	Optical Potential	11
4.1	Total and elastic cross sections	11
5	Statistical Model	12
5.1	Level Density	13
5.2	Fission Cross Section	15
5.3	Fission Channel	15
5.3.1	Fission transmission coefficient, level density and transition state spectrum	16
5.4	Fission Data Analysis	17
5.5	Inelastic Scattering	18
5.6	Neutron Channel	18
5.7	Ground State Rotational Band	19
5.8	Total inelastic cross section	20
6	Capture cross section	20
7	Cross sections above emissive fission threshold	21
7.1	Fission cross section	22
7.2	$^{231}\text{Pa}(n,xn)$ cross section	24

8 Neutron emission spectra	24
8.1 Prompt fission neutron number ν_p	24
8.2 Prompt fission neutron spectra	25
8.2.1 Model for PFNS evaluation	25
8.2.2 Pre-fission (n, x_{nf}) neutron spectra	27
8.2.3 Comparison with previous evaluations	28
8.3 Neutron emission spectra comparison	28
9 Conclusions	30
10 Acknowledgments	30
11 Figure captions	34

1 Introduction

Protactinium-231 can initiate ^{232}U production in uranium- and uranium-thorium-fueled nuclear reactors by capture of neutrons and subsequent β -decay. This chain also could be initiated after capture and $(n,2n)$ reactions on ^{230}Th ($^{230}\text{Th}(n,\gamma) ^{231}\text{Th}(\beta^-) ^{231}\text{Pa}(n,\gamma) ^{232}\text{Pa}(\beta^-) ^{232}\text{U}$) or ^{232}Th ($^{232}\text{Th}(n,2n) ^{231}\text{Th}(\beta^-) ^{231}\text{Pa}(n,\gamma) ^{232}\text{Pa}(\beta^-) ^{232}\text{U}$) nuclides, respectively. It turns out that fission data description maintains almost the only constraint for the ^{231}Pa capture, neutron elastic and inelastic scattering, $(n,2n)$, $(n,3n)$ cross sections and secondary neutron spectra evaluation. Current approach was validated recently in case of ^{238}U , ^{232}U , ^{233}U , ^{234}U and ^{232}Th neutron data description [1, 2, 3, 4].

2 Resolved resonance energy range

Here we will briefly review the status of resolved neutron resonance parameters of ^{231}Pa .

Time-of-flight measurements of ^{231}Pa total cross section were carried out in the energy range of 0.01 to 10000 eV by Hussein et al. [5]. Resonance and neutron widths were obtained for 137 s -wave resonances up to 120 eV by transmission data analysis. Average neutron resonance spacing of 0.47 ± 0.05 eV was obtained for the resonances up to 23 eV, while estimate of $\langle \Gamma_\gamma \rangle = 40$ eV was assumed. The s -wave strength $S_o = \langle \Gamma_n^o \rangle / D$ function of $(0.90 \pm 0.10) \times 10^{-4}$ for the resonances up to 70 eV was obtained.

Wagemans et al. [6] have measured thermal fission cross section of $^{231}\text{Pa}(n,f)$, it equals 19 ± 4 mbarn, $^{235}\text{U}(n,f)$ thermal cross section of 587.6 ± 26 barns was used as a monitor. Wagemans et al. [7] have measured thermal fission cross section of $^{231}\text{Pa}(n,f)$, it equals 20 ± 1 mbarn, $^{235}\text{U}(n,f)$ thermal cross section of 587.6 ± 26 barns was used as a monitor.

Leonard and Odegaard [8] have measured $^{231}\text{Pa}(n,f)$ reaction cross section at 20 points in the vicinity of first resonance, i.e., from 0.37 to 0.52 eV.

^{231}Pa fission cross section was measured from 0.1 eV to 10 keV and between 0.1 and 12 MeV by Plattard [9, 10]. Narrow fission resonances were observed above 1.3 eV. Resonance energies are compatible with those derived by Simpson et al. [11].

Thermal capture cross section was measured by Aleksandrov et al. [12], it equals 260 ± 13 barn, resonance capture integral was estimated as 1180 ± 120 barn. Thermal capture cross section was measured also by Grintakis et al. [13], it equals 201 ± 22 barn, resonance capture integral was estimated as 1432 ± 187 barn. The latter thermal capture cross section is compatible with measured value by Smith et al. [14], which equals 200 ± 15 barns. Thermal capture cross section was measured by Elson et al. [15], which equals 293 ± 44 barns.

Resolved resonance region of ENDF/B-VI [16] data file extends up to 14.3

eV. Resolved resonance parameters were adopted from BNL-325 [17], resolved resonance parameters are assumed to be single-level Breit-Wigner parameters. Thermal capture and fission cross sections are shown in Table 1.

Region of resolved resonances in JENDL-3.3 [18] extends up to 115 eV, neutron and radiative widths were adopted from Hussein et al. [5]. Fission width were fitted to the fission areas, measured by Plattard [9], in case fission resonance was not observed, $\langle \Gamma_f \rangle = 40 \mu\text{eV}$ was adopted. A bound level was added at $E_r = -0.00949$ eV to reproduce thermal total, fission, elastic and capture cross sections, recommended in BNL-325 [17].

In present evaluation basically resonance parameters of JENDL-3.3 [18] are adopted, fission width of bound resonance is varied to fit recent thermal fission cross section by Wagemans et al. [7] of 20 ± 1 mbarn.

The resonance parameters of JENDL-3.3 [18], basically accepted in present data file of ^{231}Pa , might provide a test of neutron width and resonance spacing distributions. We performed a resonance parameter analysis based on maximum likelihood estimates [19] both of mean level spacing $\langle D_{l=0} \rangle$ and neutron strength function S_o . Correction for the missing of levels based on simultaneous analysis of level spacing distribution and neutron width distribution gives estimates of average s -wave neutron resonance spacing $\langle D_{l=0} \rangle = 0.45 \pm 0.05$ eV and strength function estimate $S_o = (0.90 \pm) \times 10^{-4}$. This estimate is compatible with that of Reference Input Parameter Library File [20] ($\langle D_{l=0} \rangle = 0.45 \pm 0.05$ eV), and $\langle D_{l=0} \rangle = 0.47$ eV, adopted in JENDL-3.3 [18] data file (see Fig. 1), missing of levels is evidenced above ~ 23 eV. Cumulative sum of reduced neutron widths of s -resonances Γ_n^o is compared with present strength function estimate of $S_o = (0.7804 \pm 0.13) \times 10^{-4}$ on Fig. 2.

The resolution function parameters as well as $\langle \Gamma_n^o \rangle$ and $\langle D_{l=0} \rangle$ are obtained by maximum likelihood method when comparing experimental distributions of reduced neutron width and resonance spacing with Porter-Thomas and Wigner distributions, modified for the resonance missing. The latter distributions will be called expected distributions. Figures 3 and 4 demonstrate the comparison of predicted level spacing $D_{l=0}$ and reduced neutron width Γ_n^o distributions with present resonance parameter set. Quantiles on Fig. 3 show eight equal probability intervals ($P(x \leq x_{0.125} = \int p(x)dx = 0.125)$ for expected level spacing distribution of s -wave resonances $D_{l=0}$. Expected level spacing distribution, which takes into account missing of weak resonances and unresolved doublets, is compatible with experimental distribution. Expected distribution is qualitatively similar to the Wigner distribution. Quantiles on Fig. 4 show six equal probability ($P(x \leq x_{0.125} = \int p(x)dx = 0.125)$ intervals for Γ_n^o expected distribution. It demonstrates that reduced neutron width distribution with account of missing is compatible with observed distribution also in the range of small reduced neutron width values. We estimate that no more than $\sim 87\%$ of levels is observed up to 117.6 eV.

Figure 5 shows a comparison of experimental distribution of reduced neutron

widths with cumulative Porter-Thomas distribution of reduced neutron widths with (expected distribution) and without resonance missing correction. Cumulative Porter-Thomas distribution of reduced neutron widths without resonance missing correction (solid line on Fig. 5) is plotted for the number of resonances $N = 175$, which takes into account present estimate of missing 27.7% levels.

Table 1
Thermal cross sections and resonance integrals

Reaction	σ^{th} , barns	RI	σ^{th} , barns	RI	σ^{th} , barns	RI	σ^{th} , barns	RI
	Present			JENDL-3.3 [18]	ENDF/B-VI [16]		BNL-325 [17]	
Total	210.69	-	210.69	-				
Elastic	9.95	-	9.954					
Fission	0.0197	4.55	0.0196	4.61	0.01		0.01±0.005	6.5
Capture	200.72	587.38	200.72	596	227	1237	210±20	1500±100

3 Unresolved resonance region

Here we will briefly review the status of unresolved neutron resonance parameters of ^{231}Pa and provide a cross section parameterization of total, capture, elastic and inelastic scattering cross sections.

The unresolved resonance energy region of ENDF/B-VI [16] extends from 14.3 eV up to 1 keV. Provided are energy independent average s -wave resonance parameters $\langle D_{J=1} \rangle = 0.11676$ eV, $\langle D_{J=2} \rangle = 0.56043$ eV, which give $\langle D \rangle = 0.097$ eV, $\langle \Gamma_\gamma \rangle = 0.045$ eV and $\langle \Gamma_f \rangle = 7$ μeV .

In JENDL-3.3 [18] unresolved resonance region extends from 115 eV up to 40 keV. Provided are energy independent average resonance parameters for s - and p -wave neutrons, fission width $\langle \Gamma_f \rangle$ being equal to zero, while estimate of $\langle \Gamma_\gamma \rangle = 0.040$ eV is adopted. Background cross section was adopted for the capture cross section, to connect smoothly at $E_n = 40$ keV with higher energy data.

We assume that lower energy of unresolved resonance energy region in present evaluation is the end-point of resolved resonance region, i.e. 115 eV, the upper energy is 77 keV, twice lower, than in our recent evaluations of ^{238}U and ^{232}Th [2, 3]. We suppose s -, p - and d -wave neutron-nucleus interactions to be effective.

3.1 Average resonance parameters

Average resonance parameters $S_o = 0.7804 \times 10^{-4}$, $\langle D_{l=0} \rangle = 0.47$ eV, $\langle \Gamma_\gamma \rangle = 40$ meV are applied for the cross section calculation from 115 eV up to 77 keV.

3.1.1 Neutron resonance spacing

Neutron resonance spacing $\langle D_J \rangle$ was calculated with the phenomenological model [21], which takes into account the shell, pairing and collective effects. The main

parameter of the model, asymptotic value of level density parameter \tilde{a} , was normalized to the observed neutron resonance spacing $\langle D_{l=0} \rangle = 0.47$ eV.

3.1.2 Neutron width

Average neutron width is calculated as follows

$$\langle \Gamma_n^{lJ} \rangle = S_l \langle D_J \rangle E_n^{1/2} P_l \nu_n^{lJ}, \quad (1)$$

where E_n is the incident neutron energy, P_l is the transmission factor for the l -th partial wave, which was calculated within black nucleus model, ν_n^{lJ} is the number of degrees of freedom of Porter-Thomas distribution (see Table 2). The p -wave neutron strength function $S_1 = 1.567 \times 10^{-4}$ at 115 eV was calculated with the optical model, using the deformed optical potential, described below.

3.1.3 Radiative capture width

Energy and angular momentum dependence of radiative capture width are calculated within a two-cascade γ -emission model with allowance for the $(n,\gamma n')$ [22] and $(n,\gamma f)$ [23] reactions competition to the $(n,\gamma\gamma)$ reaction. The $(n,\gamma\gamma)$ reaction is supposed to be a radiative capture reaction. The radiative capture width was normalized to the value of $\langle \Gamma_\gamma \rangle = 40$ meV.

3.1.4 Neutron inelastic width

Average neutron inelastic width is calculated as follows

$$\langle \Gamma_{n'}^{lJ} \rangle = S_l \langle D_J \rangle (E_n - E')^{1/2} P_l (E_n - E') \nu_{n'}^{lJ}, \quad (2)$$

where $\nu_{n'}^{lJ}$ is number of degrees of freedom of Porter-Thomas distribution (see Table 2).

3.1.5 Fission width

Fission widths are calculated within a double-humped fission barrier model. Energy and angular momentum dependence of fission width is defined by the transition state spectra at inner and outer barrier humps. We constructed transition spectra by supposing the axiality of inner saddle and mass asymmetry at outer saddle [20, 24]. Number of degrees of freedom ν_f^{lJ} of Porter-Thomas distribution is defined in Table 2. They will be described below.

Table 2.
Number of degrees of freedom

l, J	$\nu_{n'}^{lJ}$	ν_n^{lJ}	ν_f^{lJ}
0,1	1	1	2
0,2	2	1	2
1,0	1	1	1
1,1	2	2	2
1,2	1	2	2
1,3	2	1	2
2,0	1	1	1
2,1	1	2	2
2,2	2	2	2
2,3	1	2	2
2,4	1	1	2

3.2 Average cross sections in the region .115-77 keV

3.2.1 Total cross section

Up to 2 keV calculated cross section is compatible with measured data by Simpson et al. [11]. Above 10 keV total cross section was estimated assuming a decreasing trend of S_o and S_1 strength function values, since the latter and potential radius, which was adopted from optical calculations, define total cross section up $E_n = 77$ keV. To reproduce total cross section, calculated with optical model, we assume S_o value linearly decreasing starting from 10 keV to 0.7294×10^{-4} (see Fig. 6). The d -wave neutron strength function was assumed to be equal to $S_2 = 1.0668 \times 10^{-4}$. In JENDL-3.3 [18] evaluation potential scattering radius is $R = 9.05$ fm, while in ENDF/B-VI [16] $R = 8.3333$ fm, we assumed $R = 9.527$ fm, that is consistent with the results of coupled channel optical model calculations (see Fig. 6).

3.2.2 Elastic scattering cross section

Elastic scattering cross section estimate is rather insensitive to the fission cross section estimate. The discrepancy of present, ENDF/B-VI [16] and JENDL-3.3 [18] estimates from ~ 115 eV and up to ~ 78 keV, shown on Fig. 7, appears to be correlated with the different estimates of potential scattering radius.

3.2.3 Fission cross section

Fission cross section of $^{231}\text{Pa}(n,f)$ was measured by Kobayashi et al. [25] below 10 keV relative to that of $^{235}\text{U}(n,f)$ with a lead slowing-down spectrometer. Relative to $^{10}\text{B}(n,\alpha) ^{231}\text{Pa}(n,f)$ cross section was measured below 1 keV, it was normalized

to the relative to $^{235}\text{U}(\text{n},\text{f})$ reaction cross section between 200 eV and 1 keV. The mean value of the fission cross section between 0.37 and 0.52 eV, i.e., in the vicinity of the first resonance of ~ 0.4 eV, measured by Leonard and Odegaard [8], is compatible with data by Kobayashi et al. [25]. Data of JENDL-3.3 [18] and ENDF/B-VI [16] are incompatible with this measurement above ~ 100 eV, though total uncertainty of the measured data ranges from ~ 5 % to ~ 40 % (see Fig. 8).

3.2.4 Capture cross section

We adopted here s -wave radiative strength function $S_{\gamma 0} = 8.5106 \times 10^{-2}$ ($\Gamma_\gamma = 40$ meV and $\langle D_{l=0} \rangle = 0.47$ eV). The important peculiarity of the calculated $^{238}\text{U}(\text{n},\gamma)$ capture cross section, Wigner cusp above first excited level threshold, is not pronounced in case of calculated $^{231}\text{Pa}(\text{n},\gamma)$ reaction cross section, because first level is at very low position ~ 9 keV (see Fig. 9). The pattern of s -, p -and d -wave channel contributions to the capture cross section in the energy range of 0.115 - 77 keV is rather similar to that of ^{234}U target nuclide of similar fission probability. In case of $^{234}\text{U}(\text{n},\gamma)$ reaction main contribution comes from p -wave neutrons above ~ 10 keV. The p -wave contribution to the $^{231}\text{Pa}(\text{n},\gamma)$ reaction cross section is higher than that of s -wave above ~ 30 keV, while that of d -wave neutrons is the lowest. Capture cross sections in present data file and those of JENDL-3.3 [18] are rather similar, while that of ENDF/B-VI [16] is much higher (see Fig. 9). The discrepancies could be attributed mostly to the different radiative strength function estimates.

3.2.5 Inelastic scattering cross section

Calculated inelastic scattering cross section is very much different from previous evaluations of ENDF/B-VI [16] and JENDL-3.3 [18]. Conventional ENDF/B processing codes (i.e. RECENT [26], NJOY [27]) exemplify Hauser-Feshbach-Moldauer formalism. Figure 10 shows partial contributions to the inelastic scattering coming from different (l, J) -channels. Major contribution, like in case of $^{238}\text{U}+\text{n}$ interaction, comes from p -wave channels, the intermediate comes from s -wave channels, the lowest contribution comes from d -wave neutrons. Evaluated inelastic scattering cross section of ENDF/B-VI [16] JENDL-3.3 [18] are much different from present calculation.

3.2.6 Comparison of average resonance parameters

Figures 11-14 compare average neutron resonance spacings of present and previous evaluations. Reduced neutron widths $\langle \Gamma_n^{lJ} \rangle$ are compared on Figs. 15-20. Differences are pronounced either in s -wave and p -wave reduced neutron widths. Figures 21, 22 compare present and ENDF/B-VI average fission widths for the compound states, formed by s -wave neutrons.

Table 3
Average resonance parameters for ^{231}Pa

	$D_{l=0, \text{eV}}$	$\Gamma_\gamma, \text{meV}$	$S_0 \times 10^{-4}$	$S_1 \times 10^{-4}$	R, fm
JENDL-3.3	0.47	40	.90	1.24	9.05
ENDF/B-VI	0.097				
RIPL	$0.45 \pm 0.05(44)$	40 ± 2	0.78 ± 0.08		
Present	0.47	40	.7804	1.5567	9.527

The advantage of present evaluation is that it provides average energy dependent resonance parameters which reproduce cross sections, calculated with optical and statistical models, using conventional ENDF/B processing codes [26, 27] up to 77 keV.

4 Optical Potential

A coupled channel model is employed for estimating differential scattering and total cross sections. Another important application of coupled channel model is calculation of direct inelastic scattering contribution of discrete levels. The direct excitation of ground state rotational band levels $3/2^- - 5/2^- - 7/2^-$ is estimated within rigid rotator model, three levels of ground state band are assumed coupled.

We adopted here the optical potential parameters obtained for ^{232}Th [28] by fitting total cross section data, angular distributions and s -wave strength function. Then we fitted ^{231}Pa s -wave strength function $S_o = 0.7804 \times 10^{-4}$ with β_2 and β_4 deformation parameters. The optical potential parameters are as follows:

$$W_D = \begin{cases} V_R = 45.722 - 0.334E_n, \text{ MeV}, r_R = 1.2668 \text{ fm}, a_R = 0.6468 \text{ fm} \\ 3.145 + 0.455E_n, \text{ MeV}, E_n \leq 8 \text{ MeV}, r_D = 1.25 \text{ fm}, a_D = 0.5246 \text{ fm} \\ 6.785 \text{ MeV}, \quad \quad \quad 8 < E_n < 20 \text{ MeV} \\ V_{SO} = 6.2 \text{ MeV}, r_{SO} = 1.120 \text{ fm}, a_{SO} = 0.47 \text{ fm}, \\ \beta_2 = 0.165, \beta_4 = 0.070 \end{cases} \quad (3)$$

4.1 Total and elastic cross sections

Present total cross section is compared with JENDL-3.3 [18] and ENDF/B-VI [16] evaluated cross section on Fig. 23. Present and JENDL-3.3 [18] estimates are not much different, while shape of ENDF/B-VI [16] cross section is rather discrepant from both evaluations up to ~ 20 MeV. Figure 24 compares elastic cross sections estimates of present coupled channels optical potential and estimates of JENDL-3.3 [18] and ENDF/B-VI [16], obtained as a difference of total and partial reaction cross sections.

5 Statistical Model

As distinct from the previous evaluations JENDL-3.3 [18] and ENDF/B-VI [16] we calculated all neutron cross sections within Hauser-Feshbach theory, coupled channel optical model and double-humped fission barrier model, only fission cross section in the 0.2 - 1 MeV energy range was eventually normalized to measured data to reproduce vibrational resonance structure.

Hauser-Feshbach-Moldauer [29] statistical theory is employed for partial cross section calculations below emissive fission threshold. Fissioning and residual nuclei level densities as well as fission barrier parameters are key ingredients, involved in actinide neutron-induced cross section calculations. First, level density parameters are defined, using neutron resonance spacing $\langle D_{l=0} \rangle$ estimate for ^{231}Pa target nuclide. Constant temperature level density parameters T_o , E_o , U_c are defined by fitting cumulative number of low-lying levels of ^{231}Pa (see Fig. 25) [19]. Fig. 26 shows the estimate of cumulative number of low-lying levels of ^{232}Pa , obtained using systematic of constant temperature level density parameters T_o , E_o , U_c [19].

In case of fast neutron ($E_n \leq 6$ MeV) interaction with ^{231}Pa target nucleus, the main reaction channel is fission, fission cross section description serves as a major constraint for the neutron inelastic scattering and radiative neutron capture cross section estimate. Below there is an outline of the statistical model [30, 31, 32] employed.

Neutron-induced reaction cross section (n, x) for excitation energies up to emissive fission threshold is defined as

$$\sigma_{nx}(E_n) = \frac{\pi \lambda^2}{2(2I+1)} \sum_{ljJ\pi} (2J+1) T_{lj}^{J\pi}(E_n) P_x^{J\pi}(E_n) S_{nx}^{ljJ\pi}, \quad (3)$$

the compound nucleus decay probability $P_x^{J\pi}$ ($x = n, f, \gamma$) is

$$P_x^{J\pi}(E_n) = \frac{T_x^{J\pi}(U)}{T_f^{J\pi}(U) + T_n^{J\pi}(U) + T_\gamma^{J\pi}(U)}, \quad (4)$$

where $U = B_n + E_n$ is the excitation energy of the compound nucleus, B_n is the neutron binding energy, $T_{lj}^{J\pi}$ are the entrance neutron transmission coefficients for the channel ($ljJ\pi$), I is the target nucleus spin. Decay probability $P_x^{J\pi}(E_n)$ of the compound nucleus with excitation energy U for given spin J and parity π , depends on $T_f^{J\pi}$, $T_n^{J\pi}(U)$ and $T_\gamma^{J\pi}(U)$, transmission coefficients of the fission, neutron scattering and radiative decay channels, $S_{nx}^{ljJ\pi}$ denotes partial widths Porter-Thomas fluctuation factor. Below incident neutron energy equal to the cut-off energy of discrete level spectrum, neutron cross sections are calculated within Hauser-Feshbach approach with correction for width fluctuation by Moldauer [29]. For width fluctuation correction calculation only Porter-Thomas fluctuations are taken into account. Effective number of degrees of freedom for

fission channel is defined at the higher fission barrier saddle as $\nu_f^{J\pi} = T_f^{J\pi}/T_{f\max}^{J\pi}$, where $T_{f\max}^{J\pi}$ is the maximum value of the fission transmission coefficient $T_f^{J\pi}$. At higher incident neutron energies the Tepel et al. [33] approach is employed, it describes cross section behavior in case of large number of open channels correctly.

5.1 Level Density

Level density is the main ingredient of statistical model calculations. Level density of fissioning, residual and compound nuclei define transmission coefficients of fission, neutron scattering and radiative decay channels, respectively. We will briefly discuss here level densities of odd-even ^{231}Pa and odd-odd ^{232}Pa nuclides.

The level densities were calculated with a phenomenological model by Ignatyuk et al. [21], which takes into account shell, pairing and collective effects in a consistent way

$$\rho(U, J, \pi) = K_{rot}(U, J)K_{vib}(U)\rho_{qp}(U, J, \pi), \quad (5)$$

where quasiparticle level density

$$\rho_{qp}(U, J, \pi) = \frac{(2J+1)\omega_{qp}(U)}{4\sqrt{2\pi}\sigma_{\perp}^2\sigma_{\parallel}} \exp\left(-\frac{J(J+1)}{2\sigma_{\perp}^2}\right), \quad (6)$$

$\omega_{qp}(U, J, \pi)$ is state density, $K_{rot}(U, J)$ and $K_{vib}(U)$ are factors of rotational and vibrational enhancement of the level density. The collective contribution of the level density of deformed nuclei is defined by the nuclear deformation order of symmetry. The actinide nuclei at equilibrium deformation are axially symmetric. The order of symmetry of nuclear shape at inner and outer saddles were adopted from calculations within shell correction method (SCM) by Howard & Möller [34], protactinium nuclei of interest ($A \leq 232$) are assumed to be axially symmetric, then

$$K_{rot}(U) = \sigma_{\perp}^2 = F_{\perp}t, \quad (7)$$

where σ_{\perp}^2 is the spin cutoff parameter, F_{\perp} is the nuclear momentum of inertia (perpendicular to the symmetry axis), which equals the rigid-body value at high excitation energies, where the pairing correlations are destroyed, experimental value at zero temperature and is interpolated in between, using the pairing model, $F_{\parallel} = 6/\pi^2 \langle m^2 \rangle (1 - 2/3\varepsilon)$, where $\langle m^2 \rangle$ is the average value of the squared projection of the angular momentum of the single-particle states, and ε is quadrupole deformation parameter. At outer saddle deformations mass asymmetry, which doubles the level density, is assumed. The closed-form expressions for thermodynamic temperature and other relevant equations which one needs to calculate $\rho(U, J, \pi)$ are provided by Ignatyuk et al. model [21].

To calculate the residual nucleus level density at the low excitation energy, i.e. just above the last discrete level excitation energy where $N^{exp}(U) \sim N^{theor}(U)$,

we employ a Gilbert-Cameron-type approach. The constant temperature approximation of

$$\rho(U) = dN(U)/dU = T^{-1} \exp((U - U_o)/T) \quad (8)$$

is extrapolated up to the matching point U_c to the $\rho(U)$ value, calculated with a phenomenological model by Ignatyuk et al. [21] with the condition

$$U_c = U_o - T \ln(T\rho(U_c)). \quad (9)$$

In this approach $U_o \simeq -n\Delta_o$, where Δ_o is the pairing correlation function, $\Delta_o = 12/\sqrt{A}$, A is the mass number, $n = 2$ for odd-odd, 1 for odd-even nuclei, i.e. U_o has the meaning of the odd-even energy shift. The value of nuclear temperature parameter T is obtained by the matching conditions at the excitation energy U_c .

In present approach the modelling of total level density

$$\rho(U) = K_{rot}(U)K_{vib}(U) \frac{\omega_{qp}(U)}{\sqrt{2\pi\sigma}} = T^{-1} \exp((U - U_o)/T) \quad (10)$$

in Gilbert-Cameron-type approach looks like a simple renormalization of quasiparticle state density $\omega_{qp}(U)$ at excitation energies $U < U_c$. The cumulative number of observed levels for odd-even ^{231}Pa [35] and odd-odd ^{238}Np [36, 37] are compared with constant temperature approximation on Figs. 25 and 26. In case of ^{231}Pa missing of levels above ~ 0.35 MeV is markedly pronounced. In case of ^{232}Pa nuclide missing seems to start much earlier.

Few-quasiparticle effects which are due to pairing correlations are essential for state density calculation at low intrinsic excitation energies only for equilibrium ^{231}Pa deformations. Few-quasiparticle effects in fissioning nuclide ^{232}Pa are unimportant because of its odd-odd nature.

The partial n -quasiparticle state densities for odd ^{231}Pa , which sum-up to intrinsic state density of quasiparticle excitations could be modelled using the Bose-gas model prescriptions [38, 39]. The intrinsic state density of quasiparticle excitations $\omega_{qp}(U)$ could be represented as a sum of n -quasiparticle state densities $\omega_{nqp}(U)$:

$$\omega_{qp}(U) = \sum_n \omega_{nqp}(U) = \sum_n \frac{g^n (U - U_n)^{n-1}}{((n/2)!)^2 (n-1)!}, \quad (11)$$

where $g = 6a_{cr}/\pi^2$ is a single-particle state density at the Fermi surface, n is the number of quasiparticles. The important model parameters are threshold values U_n for excitation of n -quasiparticle configurations $n = 1, 3\dots$ for odd- A nuclei [39]. The detailed treatment of this approach and approximations employed, as applied for fission, inelastic scattering or capture reaction calculations, is provided in [40, 41].

In case of odd-odd nucleus ^{232}Pa Gilbert-Cameron-type approximation of $\rho(U)$ is employed. Nuclear level density $\rho(U)$ of odd nuclide ^{231}Pa at equilibrium

deformation, as compared with the Gilbert-Cameron-type approximation of $\rho(U)$ is shown on Fig. 27. The arrows on the horizontal axis of Fig. 27 indicate the excitation thresholds of odd n -quasiparticle configurations.

Main parameters of the level density model for equilibrium, inner and outer saddle deformations are as follows: shell correction δW , pairing correlation functions Δ and Δ_f , at equilibrium deformations $\Delta = 12/\sqrt{A}$, quadrupole deformation ε and momentum of inertia at zero temperature F_0/\hbar^2 are given in Table 4. For ground state deformations the shell corrections were calculated as $\delta W = M^{exp} - M^{MS}$, where M^{MS} denotes liquid drop mass (LDM), calculated with Myers-Swiatecki parameters [42], and M^{exp} is the experimental nuclear mass. Shell correction values at inner and outer saddle deformations $\delta W_f^{A(B)}$ are adopted following the comprehensive review by Bjornholm and Lynn [43].

Table 4

Level density parameters of fissioning nucleus and residual nucleus

Parameter	inner saddle	outer saddle	neutron channel
δW , MeV	1.5	0.6	LDM
Δ , MeV	$\Delta_o + \delta^*$	$\Delta_o + \delta^*$	Δ_o
ε	0.6	0.8	0.24
F_0/\hbar^2 , MeV $^{-1}$	100	200	73

*) $\delta = \Delta_f - \Delta$ value is defined by fitting fission cross section in the plateau region.

5.2 Fission Cross Section

Fission data fit is used as a major constraint for capture, elastic and inelastic scattering, (n,2n) and (n,3n) cross sections as well as secondary neutron spectrum estimation. Description of measured fission cross section might justify a validity of level density description and fission barrier parameterization.

5.3 Fission Channel

Fission barrier of Pa is three-humped [34], that is, the outer barrier has one more shallow well. However, inner barrier height is rather low as compared with the outermost one [34]. That means in the first "plateau" region and at higher energies we can use double-humped barrier model and relevant barrier parameters. Even at lower energies we could describe the the general shape of the fission cross section starting from ~ 0.01 keV.

Neutron-induced fission in a double humped fission barrier model could be viewed as a two-step process, i.e. a successive crossing over the inner hump A and over the outer hump B . Hence, the transmission coefficient of the fission channel $T_f^{J\pi}(U)$ can be represented as

$$T_f^{J\pi}(U) = \frac{T_{fA}^{J\pi}(U)T_{fB}^{J\pi}(U)}{(T_{fA}^{J\pi}(U) + T_{fB}^{J\pi}(U))}. \quad (12)$$

The transmission coefficient $T_{fi}^{J\pi}(U)$ is defined by the level density $\rho_{fi}(\epsilon, J, \pi)$ of the fissioning nucleus at the inner and outer humps ($i = A, B$, respectively):

$$T_{fi}^{J\pi}(U) = \sum_{K=-J}^J T_{fi}^{JK\pi}(U) + \int_0^U \frac{\rho_{fi}(\epsilon, J, \pi)d\epsilon}{(1 + \exp(2\pi(E_{fi} + \epsilon - U)/\hbar\omega_i))}, \quad (13)$$

where the first term denotes the contribution of low-lying collective states and the second term that from the continuum levels at the saddle deformations, ϵ is the intrinsic excitation energy of fissioning nucleus. The first term contribution due to discrete transition states depends upon saddle symmetry. The total level density $\rho_{fi}(\epsilon, J, \pi)$ of the fissioning nucleus is determined by the order of symmetry of nuclear saddle deformation.

Inner and outer fission barrier heights and curvatures as well as level densities at both saddles are the model parameters. They are defined by fitting fission cross section data at incident neutron energies below emissive fission threshold. Fission barrier height values and saddle order of symmetry are strongly inter-dependent. The order of symmetry of nuclear shape at saddles was defined by Howard and Möller [34] within shell correction method (SCM) calculation. We adopt the saddle point asymmetries from SCM calculations. According to shell correction method (SCM) calculations of Howard and Möller [34] both inner and outer saddles were assumed axially symmetric. This helped to interpret the non-threshold fission cross section behavior of $^{232}\text{U}(\text{n},\text{f})$ [44] assuming a lowered height of axially symmetric inner hump of ^{233}U , as anticipated by Howard and Möller [34] with SCM calculations. Outer barrier for protactinium nuclei is assumed mass-asymmetric.

5.3.1 Fission transmission coefficient, level density and transition state spectrum

Adopted level density description allows to describe shape of measured fission cross section data of ^{231}Pa (see Figs. 8, 28 and 29). One- and two-quasiparticle states in odd residual nuclide ^{231}Pa could be excited. The transition state spectra of odd-odd ^{232}Pa nuclide for the band-heads of Table 5 were constructed using values of F_0/\hbar^2 at the inner and outer saddles shown in Table 4.

We construct the discrete transition spectra up to ~ 130 keV, using collective states of Table 5. The discrete transition spectra, as well as continuous level contribution to the fission transmission coefficient are dependent upon the order of symmetry for fissioning nucleus at inner and outer saddles. With transition state spectra thus defined the fission barrier parameters are obtained.

Table 5.
Transition spectra band-heads, Z-even, N-odd nuclei

inner saddle		outer saddle	
K^π	E_{K^π} , MeV	K^π	E_{K^π} , MeV
6^-	0.0	6^-	0.0
1^-	0.22	1^-	0.22
0^-	0.05	0^-	0.05
1^+	0.01	1^+	0.01
2^+	0.01	0^+	0.01
0^+	0.01	3^+	0.01
3^+	0.01	2^+	0.01
0^+		1^-	0.21
0^+		6^+	0.24
0^+		6^-	0.24

5.4 Fission Data Analysis

First comprehensive measurement of $^{231}\text{Pa}(\text{n},\text{f})$ reaction cross section was done by Fursov et al. [45]. They covered neutron energy range of $E_n \sim 0.135\text{-}7.4$ MeV (see Figs. 28, 29). Data were obtained relative to the ^{239}Pu fission cross section. Previously, energy dependence of $^{231}\text{Pa}(\text{n},\text{f})$ reaction cross section was measured by Plattard et al. [9, 10] from 0.1 MeV up to 12 MeV. Data on $^{231}\text{Pa}(\text{n},\text{f})$ measured between 0.1 and 12 MeV were normalized to the $^{231}\text{Pa}(\text{n},\text{f})$ cross section, measured between 0.9 and 1.1 MeV by Sicre [46]. Data by Fursov et al. [45] are compatible with data by Plattard et al. [10] at $E_n \gtrsim 1.5$ MeV, but are severely discrepant with data by Dubrovina and Shigin [47].

Dubrovina and Shigin [47] ($E_n \sim 0.15\text{-}1.5$ MeV) have measured fission cross section with ionization chamber and electrostatic generator. The data are rather compatible with the vibration resonance structure, predicted by data by Platterd et al. [9, 10].

Williams [48] has measured $^{231}\text{Pa}(\text{n},\text{f})$ fission cross section from 0.43 up to 3 MeV, they seem to be quite compatible with measured data base up to ~ 2 MeV.

Fission cross section of $^{231}\text{Pa}(\text{n},\text{f})$ was measured by Kobayashi et al. [25] below 10 keV relative to that of $^{235}\text{U}(\text{n},\text{f})$ with a lead slowing-down spectrometer. Relative to $^{10}\text{B}(\text{n},\alpha)$ $^{231}\text{Pa}(\text{n},\text{f})$ cross section was measured below 1 keV, it was

normalized to the relative to $^{235}\text{U}(\text{n},\text{f})$ reaction cross section between 200 eV and 1 keV. The mean value of the cross section between 0.37 and 0.52 eV, i.e., in the vicinity of the first resonance of 0.4 eV, measured by Leonard and Odegaard [8] is compatible with data by Kobayashi et al. [25].

Muir and Veesser [49] ($E_n \sim 0.1\text{-}2.96$ MeV) have measured fission cross section using nuclear explosion as a neutron source. Fission cross section ratio was defined relative to the $^{239}\text{Pu}(\text{n},\text{f})$ reaction cross section. The data are relatively higher than the other measured data.

Iyer et al. [50] ($E_n \sim 0.7\text{-}2.49$ MeV) have measured fission cross section with fission fragment tracks detection and electrostatic generator. The data are drastically discrepant with the data base.

Data on $^{231}\text{Pa}(\text{n},\text{f})$ were measured by Birgul et al. [51] at 3 MeV and 14.8 MeV. Fission cross section was measured relative to that of $^{238}\text{U}(\text{n},\text{f})$ reaction, by comparing activity of selected fission products (^{99}Mo activity and chain yields). At $E_n \sim 3$ MeV data by Birgul et al. [51] are quite compatible with data by Fursov et al. [45]. At 14.8 MeV data seem to be rather low.

Rather peculiar feature of measured data is a change of the cross section shape around ~ 1 MeV and then at ~ 2 MeV incident neutron energy (see Fig. 29). We fit the decreasing trend of fission data above $E_n \sim 2.5$ MeV increasing the correlation function value at outer saddle, which controls the cross section shape, by $\delta \sim 0.1$ MeV. For incident neutron energies up to $E_n \sim 2.5$ MeV the threshold cross section shape is roughly reproduced by varying the density of one- and three-quasiparticle states of residual nuclide ^{231}Pa , as described in [41] (see Figs. 28, 29).

5.5 Inelastic Scattering

Fission data fit defines the compound inelastic neutron scattering contribution to the total inelastic scattering cross section.

5.6 Neutron Channel

The lumped transmission coefficient of the neutron scattering channel (see Eqs. (4), (5)) is given by

$$T_n^{J\pi}(U) = \sum_{l'j'q} T_{l'j'}^{J\pi}(E_n - E_q) + \sum_{l'j'I'} \int_0^{U-U_c} T_{l'j'}^{J\pi}(E'_n) \rho(U - E'_n, I', \pi) dE'_n, \quad (14)$$

where $\rho(U - E'_n, I', \pi)$ is the level density of the residual nucleus. Levels of residual nuclide ^{231}Pa [35] are provided in Table 6. The entrance channel neutron transmission coefficients $T_{lj}^{J\pi}$ are calculated within a rigid rotator coupled channel approach. For the compound nucleus formation cross section calculation, the

cross sections of the direct excitation of ground state band levels were subtracted from the absorption cross section. The compound and direct inelastic scattering components are added incoherently. In case of ^{231}Pa $U_c \sim 0.35$ MeV is assumed.

The exit neutron transmission coefficients $T_{l'j'}^{J\pi}(E'_n)$ were calculated using the re-normalized deformed optical potential of entrance channel without coupling, which describes a neutron absorption cross section.

Table 6
Levels of ^{231}Pa

	E_q , keV	J^π	K^π
1	0.0	$3/2^-$	$3/2^-$
2	0.00921	$1/2^-$	$1/2^-$
3	0.05857	$7/2^-$	$7/2^-$
4	0.077685	$5/2^-$	$3/2^-$
5	0.084216	$5/2^+$	
6	0.101408	$7/2^+$	
7	0.102268	$3/2^+$	
8	0.111653	$9/2^+$	
9	0.13400	$11/2^+$	
10	0.16900	$11/2^-$	
11	0.17416	$5/2^-$	
12	0.183495	$5/2^+$	
13	0.189000	$13/2^+$	
14	0.193200	$9/2^-$	
15	0.21824	$7/2^-$	$3/2^-$
16	0.24732	$7/2^+$	
17	0.27200	$9/2^-$	
18	0.28700	$1/2^+$	
19	0.30400	$9/2^+$	
20	0.31795	$3/2^+$	
21	0.320209	$3/2^-$	
22	0.329100	$15/2^-$	
23	0.340000	$11/2^-$	
24	0.351840	$5/2^-$	
25	0.353000	$13/2^-$	

5.7 Ground State Rotational Band

Predicted discrete level excitation cross sections shapes, calculated within a rigid rotator model, depend upon optical potential used. Calculated compound contribution is controlled mainly by the fission reaction competition (see Figs. 30-49). Figures 32 and 42 show that direct scattering essentially defines the excitation cross section of $J^\pi = 5/2^-$ and $7/2^-$ levels of ground state band levels at $E_n \gtrsim 2$

MeV. Discrepancies with previous evaluation of JENDL-3.3 [18] are due to both compound and direct contributions differences. The compound component tends to be zero above ~ 3 MeV incident neutron energy.

5.8 Total inelastic cross section

Calculated total inelastic cross section is compared with previous evaluated data on Figs. 50 and 51. Lumped contribution of the direct excitation of ground state band levels is shown to attain only $\sim 20\%$ of the total inelastic cross section at $E_n \gtrsim 2$ MeV. The calculated curve is roughly consistent with JENDL-3.3 evaluation [18] up to $E_n \sim 1$ MeV, while at higher energies the increasing and then decreasing discrepancy might be attributed to differences in the models. Our estimate and that of JENDL-3.3 evaluation [18] are incompatible with ENDF/B-VI [16] evaluation (see Figs. 50, 51).

Shape of the calculated continuum inelastic scattering cross section is rather similar to that of JENDL-3.3 [18] evaluated total inelastic scattering cross section (see Fig. 52), but the absolute values at $E_n \lesssim 6$ MeV are rather discrepant. Continuum inelastic scattering cross section of ENDF/B-VI [16] evaluation seems to be too high.

Above emissive fission threshold evaluations of inelastic scattering cross section differ severely, present estimate being the highest (see Fig. 51). In our calculations pre-equilibrium neutron emission contribution is defined by the description of ^{238}U secondary neutron spectra and consistent description of $^{238}\text{U}(\text{n},\text{f})$, $^{238}\text{U}(\text{n},2\text{n})$ and $^{238}\text{U}(\text{n},3\text{n})$ reaction cross sections [40]. Pre-equilibrium neutron emission contribution allowed to reproduce also the observed fission cross section of $^{231}\text{Pa}(\text{n},\text{f})$ up to $E_n \sim 10$ MeV.

6 Capture cross section

We have demonstrated by the analysis of measured capture cross sections of $^{238}\text{U}(\text{n},\gamma)$ and $^{232}\text{Th}(\text{n},\gamma)$ [52] that neutron capture data could be described within a Hauser-Feshbach-Moldauer statistical model. Specifically, in a few-keV energy region calculated capture cross section is defined by the radiative strength function value $S_\gamma = \Gamma_\gamma/D$. At incident neutron energies above ~ 100 keV calculated capture cross section shape is defined by the energy dependence of radiative strength function S_γ . Energy dependence of S_γ is controlled mainly by the energy dependence of the level density of the compound nuclide ^{232}Pa . Rather low fission threshold for the ^{232}Pa nuclide necessitates the inclusion of the competition of fission [23] alongside with neutron emission [22] at the second γ -cascade, i.e. after first γ -quanta emission. Then "true" capture reaction cross section $(\text{n},\gamma\gamma)$ is defined using transmission coefficient $T_{\gamma\gamma}^{J\pi}(U)$ defined in a two-cascade

approximation as

$$T_{\gamma\gamma}^{J\pi} = \frac{2\pi C_{\gamma 1}}{3(\pi hc)^2} \int \varepsilon_\gamma^2 \sigma_\gamma(\varepsilon_\gamma) \sum_{I=|J-1|}^{I=J+1} \rho(U - \varepsilon_\gamma, I, \pi) \frac{T_f^{I\pi}}{T_f^{I\pi} + T_{n'}^{I\pi} + T_\gamma^{I\pi}} d\varepsilon_\gamma , \quad (15)$$

The last term of the integrand describes the competition of fission, neutron emission and γ -emission at excitation energy ($U - \varepsilon_\gamma$) after emission of first γ -quanta, $C_{\gamma 1}$ is the normalizing coefficient. That means that transmission coefficients $T_\gamma^{I\pi}$, $T_{n'}^{I\pi}$ and $T_f^{I\pi}$ are defined at excitation energy ($U - \varepsilon_\gamma$). The neutron emission after emission of first γ -quanta strongly depends on the ^{231}Pa residual nuclide level density at low excitations. The contribution of $(n, \gamma f)$ -reaction [23] to the fission cross section is defined by $T_{\gamma f}^{J\pi}$ value. The energy dependence of $(n, \gamma f)$ reaction transmission coefficient $T_{\gamma f}^{J\pi}$ was calculated with the expression

$$T_{\gamma f}^{J\pi} = \frac{2\pi C_{\gamma 1}}{3(\pi hc)^2} \int \varepsilon_\gamma^2 \sigma_\gamma(\varepsilon_\gamma) \sum_{I=|J-1|}^{I=J+1} \rho(U - \varepsilon_\gamma, I, \pi) \frac{T_f^{I\pi}}{T_f^{I\pi} + T_{n'}^{I\pi} + T_\gamma^{I\pi}} d\varepsilon_\gamma , \quad (16)$$

The capture cross section is shown on Fig. 53. The $(n, \gamma f)$ reaction competition to the "true" capture $(n, \gamma\gamma)$ reaction competition is appreciable only above $E_n \sim 3$ MeV. The competition of $(n, \gamma n')$ reaction to the "true" capture $(n, \gamma\gamma)$ reaction is essential above $E_n \sim 1$ MeV. We adopted here radiative capture strength function $S_{\gamma o}$, which actually corresponds to $\langle \Gamma_\gamma \rangle = 40$ meV and $\langle D_{l=0} \rangle = 0.47$ eV. Above $E_n \sim 1$ MeV capture cross section decrease is defined by $(n, \gamma f)$ and $(n, \gamma n')$ reactions competition.

Previous evaluated capture cross sections are drastically discrepant with present calculation (see Fig. 53). A consistent description of a most complete set of measured data on the (n, γ) , (n, f) and (n, n') reaction cross sections for the ^{238}U and ^{232}Th target nuclides [1, 2, 3, 52] enables one to consider the statistical theory estimate of $^{231}\text{Pa}(n, \gamma)$ reaction as fairly realistic.

7 Cross sections above emissive fission threshold

At incident neutron energies when fission of ^{231}Pa or ^{230}Pa nuclides is possible after emission of 1 or 2 pre-fission neutrons, the observed $^{231}\text{Pa}(n, f)$ fission cross section is a superposition of non-emissive or first chance fission of ^{232}Pa composite nuclide and x th-chance fission contributions. These contributions are weighted with a probability of x neutron emission before fission. For fixed statistical model parameters of residual nuclei ^{231}Pa and ^{230}Pa , fissioning in $^{231}\text{Pa}(n, nf)$ or $^{231}\text{Pa}(n, 2nf)$ reactions, the behavior of the first-chance fission cross section σ_{nf} should make it possible to reproduce the measured data on observed fission cross

section σ_{nF} of $^{231}\text{Pa}(\text{n,f})$ reaction. A consistent description of a most complete set of measured data on the (n,f), (n,2n), (n,3n) and (n,4n) reaction cross sections for the ^{238}U target nuclide up to 20 MeV enables one to consider the estimates of first neutron spectra of composite ^{232}Pa nuclide as fairly realistic.

7.1 Fission cross section

Above emissive fission threshold contributions of emissive fission to the observed fission cross section coming from $(\text{n},x\text{nf})$, $x = 1, 2, 3\dots X$, fission reactions of relevant equilibrated uranium nuclei, could be calculated as

$$\sigma_{nF}(E_n) = \sigma_{nf}(E_n) + \sum_{x=1}^X \sigma_{n,x\text{nf}}(E_n), \quad (17)$$

emissive fission contributions could be calculated using fission probability estimates $P_{fi}^{J\pi}(U)$ as

$$\sigma_{n,x\text{nf}}(E_n) = \sum_{J\pi} \int_0^{U_{max}} W_x^{J\pi}(U) P_{f(x+1)}^{J\pi}(U) dU, \quad (18)$$

where $W_x^{J\pi}(U)$ is the population of $(x+1)$ -th nucleus at excitation energy U after emission of x neutrons, excitation energy U^{max} is defined by the incident neutron energy E_n and energy, removed from the composite system in $^{231}\text{Pa}(\text{n},x\text{nf})$ reaction neutrons. Fission probabilities $P_{fx}^{J\pi}$ for fissioning nuclei ^{231}Pa and ^{230}Pa could be estimated using fission probability data from transfer reactions $^{230}\text{Th}(\text{He},\text{d})^{231}\text{Pa}$ and $^{230}\text{Th}(\text{He},\text{t})^{230}\text{Pa}$ [53].

Contribution of first-chance fission is defined by the pre-equilibrium emission of first neutron and level densities of fissioning ^{232}Pa and residual ^{231}Pa nuclides. The behavior of the first-chance fission cross section σ_{nf} is obviously related to the energy dependence of the fission probability of the ^{235}U nuclide P_{f1} [54]:

$$\sigma_{nf} = \sigma_r(1 - q(E_n))P_{nf}. \quad (19)$$

Once the contribution of the first neutron pre-equilibrium emission $q(E_n)$ is fixed [1], the first-chance fission probability P_{nf} of the ^{232}Pa composite nuclide depends only on the level density parameters of fissioning and residual nuclei. Actually, it depends on the ratio of shell correction values $\delta W_{fA(B)}$ and δW_n . The results of different theoretical calculations of the shell corrections as well as of the fission barriers vary by $1 \sim 2$ MeV. The same is true for the experimental shell corrections, which are obtained with a smooth component of potential energy calculated according to the liquid-drop or droplet model. However the isotopic changes of $\delta W_{fA(B)}$ and δW_n [43] are such that P_{nf} viewed as a function of the difference $(\delta W_{fA(B)} - \delta W_n)$ is virtually independent on the choice of smooth component of potential energy. Therefore, we shall consider the adopted $\delta W_{fA(B)}$

estimates (see Table 4) to be effective, provided that δW_n are obtained with the liquid drop model. Fission barrier of Pa is three-humped [34], that is, the outer barrier has one more shallow well. However, the inner barrier height is rather low as compared with the outer splitted one [34]. So, in the first "plateau" region and at higher energies we can safely use double-humped barrier model and relevant barrier parameters (see Table. 7).

Neutron-induced fission cross section of $^{231}\text{Pa}(n,f)$ reaction, shown on the Fig. 54 demonstrates strong step-like structures, relevant to the contributions of (n,xnf) reactions to the observed fission cross section. Above (n,nf) reaction threshold calculated curve is compatible with measured data by Fursov et al. [45] - up to 7 MeV, and up to 10 MeV with data by Plattard et al. [10]. Data point by Birgul et al. [51] at ~ 14 MeV seems to be too low. Actually, it could be fitted (see Fig. 54), but for that the contribution of the second chance fission cross section $^{231}\text{Pa}(n,nf)$ should be very low, so that total fission cross section would be discrepant with data by Plattard et al. [10] at $E_n \gtrsim 7$ MeV. Figure 55 shows relative contributions of fission chances to the observed fission cross sections of $^{231}\text{Pa}(n,f)$. The contributions of first-chance fission to the $^{231}\text{Pa}(n,f)$ and $^{238}\text{U}(n,f)$ reaction cross sections are similar functions of incident neutron energy. In both cases a local minimum is observed near the (n,nf) -reaction threshold. The second-chance fission contribution of $^{231}\text{Pa}(n,nf)$ reaction is a smooth increasing function of excitation energy up to $E_n \sim 7$ MeV. The contribution of $^{231}\text{Pa}(n,2nf)$ reaction to the total fission cross section is somewhat lower than in case of $^{238}\text{U}(n,2nf)$ reaction. Figure 56 compares calculated fission cross sections of $^{231}\text{Pa}(n,f)$ and $^{229}\text{Pa}(n,f)$ with simulated fission cross section data obtained by Britt and Wilhelm [53] as $\sigma_f = 3.1P_f$. The discrepancies of calculated curves and simulated data for $E_n \lesssim 2$ MeV is explained by the entrance channel influence for transfer reactions and neutron-induced fission reaction. Figure 57 shows the same for the $^{230}\text{Pa}(n,f)$ reaction. Double-dot dashed curve shows the $^{230}\text{Pa}(n,f)$ fission cross section, decreased to fit the data point by Birgul et al. [51].

Table 7
Fission barrier parameters of Pa nuclei

Nuclide	E_A	E_B	$\hbar\omega_A$	$\hbar\omega_B$	δ	δ_{1f}	δ_{1n}
^{234}Pa	5	6.4	.6	.42	.21		
^{233}Pa	5	5.9	1	.5	.165	2.275	1.5
^{232}Pa	5	6.2	.6	.42	.20		
^{231}Pa	5.25	5.45	1.	.5	.075	2.75	1.75
^{230}Pa	5.0	5.5	.6	.4	.25		
^{229}Pa	4.8	6.0	.7	.5	.075	1.5	1.5

7.2 $^{233}\text{Pa}(\text{n},\text{xn})$ cross section

There is no measurements of $^{233}\text{Pa}(\text{n},2\text{n})$ or $^{233}\text{Pa}(\text{n},3\text{n})$ reaction cross section. These cross sections are estimated using $^{233}\text{Pa}(\text{n,f})$ fission cross section fit up to $E_n = 20$ MeV as the only constraint. Present estimate of $^{233}\text{Pa}(\text{n},2\text{n})$ cross section for $E_n \lesssim 10$ MeV is about twice lower than that of JENDL-3.3 [18], the estimate of ENDF/B-VI [16] shows unrealistic structures around $E_n \sim 10$ MeV (Fig. 58). For $E_n \gtrsim 10$ MeV calculated $(\text{n},2\text{n})$ reaction cross section shape corresponds to pre-equilibrium emission contribution to the first neutron spectrum.

Present estimate of $^{233}\text{Pa}(\text{n},3\text{n})^{232}\text{U}$ cross section is much lower than those of JENDL-3.3 [18] and ENDF/B-VI [16], both are unrealistically high (see Fig. 59), it seems to be the consequence of high absorption cross section.

8 Neutron emission spectra

Neutron emission spectra are inclusive of both fission and scattered neutrons. First we will describe the approach used for the prompt fission neutron number ν_p and prompt fission neutron spectra (PFNS) calculation and then return to the discussion on neutron emission spectra. A brief survey of the model used to estimate prompt fission neutron number ν_p value and PFNS is provided below.

8.1 Prompt fission neutron number ν_p

There are no experimental data for prompt fission neutron spectra and prompt neutron multiplicity ν_p for ^{231}Pa . The evaluated data for JENDL-3.3 [18] and ENDF/B-VI [16] files are based on the systematics by Bois and Frehaut [55], which uses simple linear extrapolation of ν_p from the first chance energy range up to 20 MeV. We applied more complicated approach, which incorporates the pre-fission neutron emission and relevant fission chances. The incident neutron energy dependence of the first chance neutron multiplicity in the energy range $E_n \lesssim 6$ MeV for all fissioning Pa nuclides was taken from the evaluation by Malinovskij [56]. At incident neutron energies above emissive fission threshold the number of prompt fission neutron $\nu_p(E_n)$ was calculated as

$$\begin{aligned} \nu_p(E_n) = & \beta_0 \nu_o(E_n) + \beta_1 (1 + \nu_1(E_n - B_{nA} - \langle E_1 \rangle)) + \\ & \beta_2 (2 + \nu_2(E_n - B_{nA} - B_{nA-1} - \langle E_1 \rangle - \langle E_2 \rangle)). \end{aligned} \quad (20)$$

Here, $\nu_i(E_n)$ is a prompt fission neutron number for i -th fissioning Pa nuclide, B_{nA} - neutron binding energy for the A nucleus, $\langle E_i \rangle$ - average energy of i -th pre-fission neutron. To calculate the ν_p for $^{231}\text{Pa}(\text{n,f})$ reaction up to $E_n = 20$ MeV we need to estimate ν_p values for ^{230}Pa and ^{229}Pa target nuclides, which contribute

to the observed ν_p -value of neutron-induced fission of ^{231}Pa target nuclide via (n,xnf) emissive fission processes. We assumed that excitation energy

$$U_i = E_n - \sum_j (B_{nj} + \langle E_{ij} \rangle), \quad (21)$$

is brought into A_i nucleus with the reaction: $n + (A_i - 1) \rightarrow \text{fission}$. Incident neutron energy in this hypothetical reaction equals to $U_i - B_{nA_i}$. In this way the $\nu_i(E_n)$ functions for all nuclides in the mass chain $A+1, A, A-1$ were calculated.

Energy dependence of ν_p versus incident neutron energy estimated with this equation is compared on Fig. 60 with previous evaluations. Relevant partial contributions are shown on Fig. 61. Bump in ν_p above (n,nf) reaction threshold is due to the pre-fission neutrons, emitted in $^{231}\text{Pa}(n,nf)$ reaction. The similar behavior was evidenced in measured multiplicity data for the $^{232}\text{Th}(n,f)$ and $^{238}\text{U}(n,f)$, it was reproduced with the present model. The delayed neutrons yield and decay parameters were taken to be the same as in JENDL-3.3 [18] evaluated data file, i.e. from [57].

Table 8
The evaluated first chance ν -values for $^{229,230,231}\text{Pa}$ target nuclides.

Target	ν^{th}	$\nu(3 \text{ MeV})$	$\nu(6 \text{ MeV})$
^{229}Pa	2.283	2.669	2.798
^{230}Pa	2.331	2.592	2.850
^{231}Pa	2.298	2.561	2.821

8.2 Prompt fission neutron spectra

Prompt Fission Neutron Spectra (PFNS) for ^{231}Pa have been calculated with the model that was previously applied for ^{238}U and ^{232}Th PFNS data analysis [58, 59]. Here is enclosed a brief description of the PFNS model.

8.2.1 Model for PFNS evaluation

For the first chance fission reaction the PFNS are calculated as a sum of two Watt distributions [60]:

$$S_i(E, E_n) = 0.5 \cdot \sum_{j=1,2} W_i(E, E_n, T_{ij}(E_n), \alpha) \quad (22)$$

where

$$T_{ij} = k_{ij} \cdot \sqrt{E^*} = \sqrt{E_r + E_n + B_n - TKE} \quad (23)$$

is the temperature parameters of light and heavy fragments ($j=1,2$) for nucleus "i", is the ratio of the total kinetic energy (TKE) at the moment of the neutron emission to the TKE value at full acceleration limit. Ratio α was used as a

free parameter to fit PFNS experimental data for a number of actinide nuclei, its values for various nuclei scatter only slightly. The ratio of the "temperatures" for light and heavy fragment was the second semi-empirical fitting parameter, it also varies from one target nucleus to another only slightly, we assumed $r=1.248$ for all actinide nuclei.

Above emissive fission threshold PFNS are described by the equation

$$\begin{aligned}
S(E, E_n) &= \nu^{-1}(E_n)(\nu_o(E_n) \cdot \beta_o(E_n) \cdot S_o(E, E_n) + \\
&\quad \nu_1(E_n) \cdot \beta_1(E_n) \cdot S_1(E, E_n) + \beta_1(E_n) \cdot P_{11}(E, E_n) + \\
&\quad \nu_2(E_n) \cdot \beta_2(E_n) \cdot S_2(E, E_n) + \\
&\quad \beta_2(E_n) \cdot [P_{21}(E, E_n) + P_{22}(E, E_n)] + \dots), \\
\int P_{ik}(E, E_n) dE &= 1, \\
\nu(E_n) &= \sum_{i=0} [\nu_i(E_n) + i] \cdot \beta_i(E_n),
\end{aligned} \tag{24}$$

where subscript i denotes i -th chance fission reaction of the $A+1$, A , $A-1$ nuclei after emission of i pre-fission neutrons, $\beta_i(E_n)$ is the i -th chance fission contribution to the observed fission cross section (see Figs. 54 and 55), $\nu_i(E_n)$ is the number of the prompt fission neutron for relevant nucleus, $S_i(E, E_n)$ is the PFNS spectrum without pre-fission neutrons, $P_{ik}(E, E_n)$ is the spectrum of k -th pre-fission neutron for i -th chance fission. To estimate observed PFNS, $\nu_i(E_n)$, $\beta_i(E_n)$ and T_{ij} values should be calculated.

The pre-fission neutron spectra $P_{ik}(E, E_n)$ were calculated as described in [59]. The pre-equilibrium pre-fission neutron emission was also taken into account.

The excitation energy U_i of the nucleus $A_i = A+1-i$ after emission of i neutrons was calculated as:

$$U_i = B_n + E_n - \sum_j (B_j + \langle E_{ij} \rangle), \tag{25}$$

where B_j is the neutron binding energy. This allows to estimate the excitation energy of fission fragments as $E^* = E_r + U - TKE$ and calculate the $T_{ij}(E_n)$ energy for each nucleus in the mass chain. The equation for the $\nu_i(E_n)$ calculation is given in previous section.

For $E_n \gtrsim 10$ MeV we incorporated an additional correction, used previously to remove a discrepancy between measured and calculated data for PFNS of $^{238}\text{U}(\text{n},\text{f})$ and $^{232}\text{Th}(\text{n},\text{f})$ reactions [58]. We assume that the same correction for CMS energy per nucleon E_{v0} should be introduced for $^{231}\text{Pa}(\text{n},\text{f})$ reaction. The CMS energy was calculated as

$$E_v = \alpha \cdot \alpha_1 \cdot E_{v0}, \tag{26}$$

$\alpha_1=1$ for $E_n \leq 10$ MeV and $\alpha_1=0.8$ for $E_n > 12$ MeV and linearly interpolated for $10 < E_n < 12$ MeV. This correction was made either for non-emissive and emissive fission reactions.

8.2.2 Pre-fission (n,xnf) neutron spectra

Partial neutron energy distributions $P_{ik}(E, E_n)$ of (n,xnf) , $x = 1, 2, 3$, reactions are calculated with Hauser-Feshbach model taking into account fission and gamma-emission competition to the neutron emission, actually neutron spectra are calculated simultaneously with fission and (n,xn) reaction cross sections [59]. The pre-equilibrium emission of the first neutron is fixed by the description of high energy tails of $(n,2n)$ reaction cross sections and (n,f) reaction cross sections for ^{238}U and ^{232}Th target nuclides. First neutron spectrum of the $^{231}\text{Pa}(n,nf)$ reaction is the sum of evaporated and pre-equilibrium emitted neutron contributions. Second and third neutron spectra for $^{231}\text{Pa}(n,xnf)$ fission reactions are assumed to be evaporative. Pre-fission neutron spectrum of $^{231}\text{Pa}(n,nf)$ reaction, especially its hard energy tail, is sensitive to the description of fission probability of ^{231}Pa nuclide near fission threshold (see below).

Partial neutron spectra are shown on Figs. 62-68. Components of first, second and third neutron spectra for $E_n = 20$ MeV are shown on Figs. 62, 63 and 64. Components of first and second neutron spectra for $E_n = 14$ MeV are shown on Figs. 65, 66, for $E_n = 8$ MeV - on Figs. 67, 68.

At $E_n = 20$ and 14 MeV major contributions to the first neutron spectrum come from the $(n,2n)$ and $(n,3n)$ reactions spectra (see Figs. 62, 65), at lower energy $E_n = 8$ MeV major contribution comes from (n,nf) reaction (see Fig. 67). Spectrum of $(n,n\gamma)$ reaction actually is just hard energy tail of ‘pre-equilibrium’ component of first neutron spectrum. Shapes of first neutron spectra of $(n,n\gamma)$ and $(n,2n\gamma)$ reactions at $E_n = 20$ (Fig. 62) and 14 MeV (Fig. 65) are rather similar, soft part being defined by the neutron emission competition in higher neutron multiplicity reactions. This lowering of soft part of first neutron spectrum of $(n,2n\gamma)$ reaction disappears for $E_n = 8$ MeV (see Fig. 67).

At $E_n = 20$ MeV major contribution to the second neutron spectrum (up to $E \sim 8$ MeV) comes from $(n,3n)$ reaction (see Fig. 63). Soft parts of the second neutron spectra of $(n,2n)$ and $(n,2nf)$ reactions are comparable. At lower incident neutron energy $E_n = 14$ MeV major contribution to the second neutron spectrum comes from $(n,2n\gamma)$ reaction (see Fig. 66). At lower energy $E_n = 8$ MeV major contribution to the second neutron spectrum, obviously, comes from $(n,2n\gamma)$ reaction (see Fig. 68)

At $E_n = 20$ MeV most contribution to the third neutron spectrum comes from $(n,3n\gamma)$ reaction (see Fig. 64), that of the $(n,3nf)$ reaction being rather low.

8.2.3 Comparison with previous evaluations

The PFNS for the ^{231}Pa data files of ENDF/B-VI [16] and JENDL-3.3 [18] libraries coincide, they were assumed to be Maxwellian. The PFNS calculated with present model demonstrate more complicated shape as compared with simple Maxwellian estimate for $E_n = 2$ MeV (Fig. 69). The peculiarities similar to ^{238}U , ^{232}Th nuclei [59] for which the experimental data are available, are also noticed.

Above emissive fission threshold at $E_n = 7$ MeV the contribution of the second chance fission reaction $^{231}\text{Pa}(\text{n},\text{f})$ is comparable with that of non-emissive fission (see Figs. 54, 55). The average energy removed by first pre-fission neutron is much smaller than the average energy of the post-fission neutrons. This peculiarity explains appearance of the low energy bump in the spectrum of fission neutrons (Fig. 70). At higher incident neutron energies of $E_n = 14$ and 20 MeV (Figs. 71 and 72), the PFN spectrum also consists of several components. One of them is connected with pre-equilibrium first neutron emission and produces bump at $E_{th} \sim E_n - B_{fA} \sim 7$ MeV prompt fission neutron energy for $E_n = 14$ MeV or $E_{th} \sim 12$ MeV for $E_n = 20$ MeV, B_{fA} is the effective fission barrier of ^{231}Pa fissioning nuclide. Soft neutron component connected with pre-fission neutrons from ($\text{n},2\text{nf}$) reaction is noticed on Fig. 71 for $E_n = 14$ MeV. Irregularity around 7 MeV for PFNS for $E_n = 20$ MeV (see Fig. 72) might be correlated with the first neutron spectrum of $^{231}\text{Pa}(\text{n},2\text{nf})$ reaction, $P_{21}(E, E_n)$ ($(\text{n},2\text{nf})^1$), it is sensitive to the description of fission probability of ^{230}Pa near fission threshold.

The average energy of the fission neutron versus incident energy is shown in fig. 73. At incident neutron energy $E_n \lesssim 6$ MeV, the ν_p -value energy dependence is proportional to $\sqrt{U_i}$, however, at higher excitations we have more complicated excitation energy dependence. At $E_n \sim 7$ MeV the average energy reduces by ~ 300 keV due to the contribution of low energy neutrons from (n,nf) reaction. This tendency, visible in measured data for the $^{238}\text{U}(\text{n},\text{f})$ PFNS, is predicted for the $^{231}\text{Pa}(\text{n},\text{f})$ reaction.

8.3 Neutron emission spectra comparison

There is no measured data on neutron emission spectra for $^{231}\text{Pa}+\text{n}$ interaction. For incident neutron energy higher than emissive fission threshold, emissive neutron spectrum is deconvoluted, components of 1st, 2nd and 3d neutron spectra are provided, where applicable. We have calculated 1st, 2nd and 3d neutron spectra for the ($\text{n},\text{n}\gamma$), ($\text{n},2\text{n}$) and ($\text{n},3\text{n}$) reactions.

According to the ENDF/B-VI format specifications the secondary neutron spectra are included in the following way. Calculated spectra were summed up and tabular spectra for the ($\text{n},\text{n}\gamma$), ($\text{n},2\text{n}$) and ($\text{n},3\text{n}$) reactions were obtained.

Spectrum of ($\text{n},\text{n}\gamma$) reaction actually is just hard energy tail of ‘pre-equilibrium’ component of first neutron spectrum. Spectrum of the first neutron of ($\text{n},2\text{n}$)

reaction is much softer, although 'pre-equilibrium' component still comprise appreciable part of it. First neutron spectrum of (n,3n) reaction is actually of evaporative nature. First neutron spectrum of (n,nf) reaction has rather long pre-equilibrium high-energy tail. First neutron spectrum of (n,2nf) reaction, as that of (n,3n) reaction, is of evaporative nature.

Figures 74-79 compare neutron spectra of (n,n γ) reaction of JENDL-3.3 [18] and ENDF/B-VI [16] with present calculation. Neutron spectra of ENDF/B-VI [16] and JENDL-3.3 [18] are evaporative. At $E_n = 20$ and 14 MeV hard energy tails of 'pre-equilibrium' component of first neutron spectrum of JENDL-3.3 [18] and present evaluation are rather pronounced. Average energies of first neutron spectra for ENDF/B-VI are much lower than that of present evaluation.

Table 9

Average energies of secondary neutron spectra for $^{231}\text{Pa} + \text{n}$

E_n, MeV	1st neutron average energy $\langle E \rangle$, MeV						
	(n,n')			(n,2n)	(n,n'f)	(n,3n)	(n,2n'f)
	Present	B-VI	J-3.3	Present			
6.0	1.263	1.223	0.902	0.000	0.334		
8.0	2.883	-	1.050	.479	1.015		
10.0	5.152	1.531	1.179	1.098	1.561		
14.0	9.288	-	1.400	3.042	2.530	0.661	0.980
20.0	15.159	2.107	1.678	9.057	3.798	3.085	2.962

Table 9 (continued)

Average energies of secondary neutron spectra for $^{231}\text{Pa} + \text{n}$

E_n, MeV	$\langle E \rangle$ for (n,2n), MeV			$\langle E \rangle$ for (n,3n), MeV		
	Present	J-3.3	B-VI	Present	J-3.3	B-VI
8.0	0.420	0.587	-	-	-	-
10.0	0.900	0.937	1.307	-	-	-
14.0	2.048	1.164	-	0.473	0.670	-
20.0	5.099	1.488	2.106	1.770	1.236	2.060

Figures 80-83 show the comparison of (n,2n) reaction spectra of JENDL-3.3, ENDF/B-VI and present evaluation at $E_n = 20, 14, 10$ and 8 MeV. The discrepancies above ~ 5 MeV and ~ 3 MeV, ~ 1 MeV and ~ 0.5 MeV respectively, are due to first neutron spectra of (n,2n) reaction in present calculation being of hard pre-equilibrium nature. Figures 84 and 85 show spectra of (n,3n) reaction for incident neutron energy of 20 and 14 MeV, respectively.

In summary, inclusion of pre-equilibrium emission changes significantly the average energies of emitted neutron spectra. That is shown in Table 9, where the average secondary neutron energies for current, ENDFB-VI and JENDL-3.3 evaluations are compared. The most significant is the change of neutron spectra of ($n,n\gamma$) reaction.

9 Conclusions

The statistical Hauser-Feshbach-Moldauer model calculation of neutron-induced reaction cross sections for ^{231}Pa target nuclide shows the fair description of available data on fission cross section. Statistical calculations were employed for predicting total, capture, inelastic, ($n,2n$) and ($n,3n$) reaction cross sections. Rigid rotator coupled channel model was used to predict inelastic scattering cross sections for the ground state band levels excitation. Prompt fission neutron spectra are predicted with the model, tested on the PFNS description of $^{238}\text{U}(n,f)$ and $^{232}\text{Th}(n,f)$ reactions.

10 Acknowledgments

This work was supported within the Project B-404 "Actinide Nuclear Data Evaluation" of International Science and Technology Center (Funding Party Japan).

References

- [1] Maslov V.M., Porodzinskij Yu. V., Baba M., Hasegawa A., Kornilov N.V., Kagalenko A.B., Proc. International Conference on Nuclear Data for Science and Technology, October 7-12, 2001, Tsukuba, Japan, p. 148, 2002.
- [2] Maslov V.M. , Yu. V. Porodzinskij, M. Baba, A. Hasegawa, Ann. Nucl. Energy, 29, 1707 (2002).
- [3] Maslov V.M., Porodzinskij Yu. V., Baba M., Hasegawa A., Nucl. Sci. Eng. (2003).
- [4] Maslov V.M., Porodzinskij Yu. V., Baba M., Hasegawa A., Ann. Nucl. Energy, 30, 1155 (2003).
- [5] Hussein A.-R.Z., Harvey J.A., Hill N.W., and J.R. Patterson. Nucl. Sci. Eng., 78, 370-376 (1981).

- [6] Wagemans C. , D'Hondt P., Deruytter A.J., Asghar M., Emsallem A. J. Nucl. Physics A285, 32 (1977).
- [7] Wagemans C. , D'Hondt P., Deruytter A.J., Ann. Nucl. Energy, 5, 267 (1978).
- [8] Leonard B.R., Odegaard R.H. Bulletin of American Physical Society, 6, 8 (A8) (1961)).
- [9] Plattard S., Auchampaugh G.F., Hill H.W. et al., in: U. S. National Bureau of Standards Special Publication No. 594, 1980 (unpublished), Proceedings of the Conference on Nuclear Cross Sections for Technology, Knoxville, Tennessee, 1979, p. 491.
- [10] Plattard S., Auchampaugh G.F., Hill H.W. et al. Phys. Rev. Lett., 46, 633 (1981).
- [11] Simpson F.B., Burgus W.H., Evans J.E., Kirby H.W. Nucl. Sci. Eng., 12, 243 (1962).
- [12] Aleksandrov B.M., Back M.A., Krivokhvatskij A.S., Chlyamin E.A. Atomnaya Energiya, 32 (2), 178 (1972).
- [13] Gryntakis E.M. and Kim J.I. J.Inorg. Nucl. Chem. 36, 1447 (1974).
- [14] Smith R.R., Alley N.P., Lewis R.H., VanderDoes A., Phys. Rev., 101,1053 (1956).
- [15] Elson R., Sellers P.A, John E.R Phys., Rev. , 90, (1), 102 (1953).
- [16] Roussin R.W., Young P.G., McKnight R., Proc. Int. Conf. Nuclear Data for Science and Technology, Gatlinburg, USA, May 9-13, 1994, p. 692, J.K. Dickens (Ed.), ANS, 1994.
- [17] Mughabghab S.F.and Garber D.I., BNL-325, VOL. 1, BRookhaven National Laboratory (2973).
- [18] Shibata K., Kawano T., Nakagawa T. et al., J. Nucl. Sci. Technol.,39, 1125 (2002).
- [19] Maslov V.M., Porodzinskij Yu.V. JAERI-Research 98-038, Japan, 1998.
- [20] Handbook for Calculations of Nuclear Reaction Data: Reference input parameter library,IAEA-TECDOC-1034, p.81, 1998, Vienna.
- [21] Ignatjuk A.V., Istekov K.K., Smirenkin G.N. Sov. J. Nucl. Phys. 29, 450 (1979).

- [22] Moldauer P.A., Proc. Conf. on Neutron Cross Sections and Technology, Washington, D.C., USA, March 22-24, 1966, p. 613-622, AEC (1966).
- [23] Stavinskij V.S., Shaker M.O., Nucl. Phys., 62, 667 (1965).
- [24] Maslov V.M., INDC(BLR)-013, IAEA, Vienna, 1998.
- [25] Kobayashi K., Yamamoto S., Lee S. et al, Nucl. Sci. Eng., 139, 273 (2001).
- [26] Cullen D. PREPRO2000: 2000 ENDF/B Pre-Processing Codes.
- [27] NJOY 94.10 Code System for Producing Pointwise and Multigroup Neutron and Photon Cross Sections from ENDF/B Data, RSIC Peripheral Shielding Routine Collection, ORNL, PSR-355, LANL, Los Alamos, New Mexico (1995).
- [28] Maslov V.M., Porodzinskij Yu.V., Baba M., Hasegawa A., Kornilov N.V., Kagalenko A.B. and Tetereva N.A., INDC(BLR)-016, Vienna, 2003.
- [29] Moldauer P.A., Phys. Rev., C11, 426 (1975).
- [30] Maslov V.M., Nuclear Reaction data and Nuclear Reactors, Trieste, Italy, 2000, pp. 231-268, ICTP, 2001.
- [31] Ignatjuk A.V., Maslov V.M., Proc. Int. Symp. Nuclear Data Evaluation Methodology, Brookhaven, USA, October 12-16, 1992, p.440, World Scientific, 1993.
- [32] Maslov V.M., Kikuchi Y., JAERI-Research 96-030, 1996.
- [33] Tepel J.W., Hoffman H.M., Weidenmuller H.A. Phys. Lett. 49, 1 (1974)
- [34] Howard W.M., Möller P. Atomic Data and Nuclear Data Tables, 25, 219 (1980).
- [35] Schmorak M.R. Nucl. Data Sheets 21, 91 (1977).
- [36] Shurshikov E.N., Nuclear Data Sheets, 53, 601 (1988).
- [37] ENSDF: Evaluated Nuclear Structure Data File, BNL/NNDC, 1993.
- [38] Maslov V.M., Zeit. Phys. A, Hadrons & Nuclei, 347, 211 (1994).
- [39] Fu C. Nucl. Sci. Engng. 86, 344 (1984).
- [40] Maslov V.M., Porodzinskij Yu.V., Hasegawa A., Shibata K. JAERI-Research 98-040, Japan, 1998.
- [41] Maslov V.M., Physics of Atomic Nuclei, 63, 161 (2000).

- [42] Myers W.O., Swiatecky W.J., *Ark. Fyzik*, 36, 243 (1967).
- [43] Bjornholm S., Lynn J.E. *Rev. Mod. Phys.*, 52, 725 (1980).
- [44] Maslov V.M. and Kikuchi Ya., *Nucl. Sci. Eng.*, 124, 492 (1996).
- [45] Fursov B.I., Baranov E.Yu, Klemyshev M.P. et al., *Atomnaya Energiya*, 59 (4), 339 (1985).
- [46] Sicre A. Ph. D. Thesis, University of Bordeaux, 1976, Report CENBG 7603.
- [47] Dubrovina S.M., Shigin V.A. *J., DOK*, 157, (3), 561(1964).
- [48] Williams J.H. *Report LA-150* (1944).
- [49] Muir D.W., Vesser L.R. *Proc. conf. on Nucl. Cross Sections and Technology*, March 1971, Knoxville. Washington, vol. 1, 292, (1975).
- [50] Iyer R.H., Sampathkumar R., Chaudhuri N.K. P, *BARC-872*, 106 (1976).
- [51] Birgul O., Lyle S.J. *J., Radiochimica Acta*, 11, 108 (1969).
- [52] V.M. Maslov, Yu. V. Porodzinskij, M. Baba, A. Hasegawa, *Proc. of Eleventh International Symposium on Capture Gamma-Ray Spectroscopy and Related Topics*, September 2-6, Prague, 2002, pp. 757-760.
- [53] Britt H.C., Wilhelmy J.B., *Nucl. Sci. Eng.*, 72, 222 (1979).
- [54] Uhl M., Strohmaier B., *IRK-76/01*, IRK, Vienna (1976).
- [55] Bois, R. , Frehaut, J.: *CEA-R-4791* (1976).
- [56] Malinovskij V.V. *VANT (ser. Yadernye constanty)*, 1987, No.2, 25.
- [57] Tuttle R.J.: *INDC(NDS)-107/G+Special*, p.29 (1979).
- [58] V.M. Maslov, Yu. V. Porodzinskij, M. Baba, A. Hasegawa, N.V. Kornilov, A.B. Kagalenko, Tetereva N.A., *EuroPhysics Journal A*, 18 (2003) 93.
- [59] V.M. Maslov, Yu. V. Porodzinskij, M. Baba, A. Hasegawa, N.V. Kornilov, A.B. Kagalenko, *Proc. X International Seminar on Interaction of Neutrons with Nuclei*, Dubna, Russia, May 17-20, 2002, 2002.
- [60] Kornilov N.V., Kagalenko A.B., Hambach F.-J. *Physics of Atomic Nuclei*, 62, 173 (1999).

11 Figure captions

- Fig. 1 Cumulative sum of levels of ^{231}Pa .
 Fig. 2 Cumulative sum of reduced neutron widths of ^{231}Pa .
 Fig. 3 Level spacing distribution of ^{231}Pa .
 Fig. 4 Reduced neutron width distribution of ^{231}Pa .
 Fig. 5 Cumulative distribution of reduced neutron widths of ^{231}Pa .
 Fig. 6 Total cross section of ^{231}Pa .
 Fig. 7 Elastic cross section of ^{231}Pa .
 Fig. 8 Fission cross section of ^{231}Pa .
 Fig. 9 Capture cross section of ^{231}Pa .
 Fig. 10 Inelastic cross section of ^{231}Pa .
 Fig. 11 Average level spacing of ^{231}Pa , $l = 0, J = 1$.
 Fig. 12 Average level spacing of ^{231}Pa , $l = 0, J = 2$.
 Fig. 13 Average level spacing of ^{231}Pa , $l = 1, J = 0$.
 Fig. 14 Average level spacing of ^{231}Pa , $l = 1, J = 3$.
 Fig. 15 Average reduced neutron width of ^{231}Pa , $l = 0, J = 1$.
 Fig. 16 Average reduced neutron width of ^{231}Pa , $l = 0, J = 2$.
 Fig. 17 Average reduced neutron width of ^{231}Pa , $l = 1, J = 0$.
 Fig. 18 Average reduced neutron width of ^{231}Pa , $l = 1, J = 1$.
 Fig. 19 Average reduced neutron width of ^{231}Pa , $l = 1, J = 2$.
 Fig. 20 Average reduced neutron width of ^{231}Pa , $l = 1, J = 3$.
 Fig. 21 Average fission width of ^{231}Pa , $l = 0, J = 1$.
 Fig. 22 Average fission width of ^{231}Pa , $l = 0, J = 2$.
 Fig. 23 Total cross section of ^{231}Pa .
 Fig. 24 Elastic scattering cross section of ^{231}Pa .
 Fig. 25 Cumulative number of levels of ^{231}Pa .
 Fig. 26 Cumulative number of levels of ^{232}Pa .
 Fig. 27 Level density of ^{231}Pa .
 Fig. 28 Fission cross section of ^{231}Pa .
 Fig. 29 Fission cross section of ^{231}Pa .
 Fig. 30 Cross section of ^{231}Pa : 0.00921 MeV, $1/2^-$ level excitation.
 Fig. 31 Cross section of ^{231}Pa : 0.05857 MeV, $7/2^-$ level excitation..
 Fig. 32 Cross section of ^{231}Pa : 0.077685 MeV, $5/2^-$ level excitation.
 Fig. 33 Cross section of ^{231}Pa : 0.084214 MeV, $5/2^+$ level excitation.
 Fig. 34 Cross section of ^{231}Pa : 0.101408 MeV, $7/2^+$ level excitation.
 Fig. 35 Cross section of ^{231}Pa : 0.102268 MeV, $3/2^+$ level excitation.
 Fig. 36 Cross section of ^{231}Pa : 0.11653 MeV, $(9/2^+)$ level excitation.
 Fig. 37 Cross section of ^{231}Pa : 0.134 MeV, $(11/2^+)$ level excitation.
 Fig. 38 Cross section of ^{231}Pa : 0.1691 MeV, $11/2^-$ level excitation.
 Fig. 39 Cross section of ^{231}Pa : 0.17416 MeV, $(5/2^-)$ level excitation.
 Fig. 40 Cross section of ^{231}Pa : 0.183495 MeV, $(5/2^+)$ level excitation.
 Fig. 41 Cross section of ^{231}Pa : 0.189 MeV, $13/2^+$ level excitation.

- Fig. 42 Cross section of ^{231}Pa : 0.21824 MeV, ($7/2^-$) level excitation.
 Fig. 43 Cross section of ^{231}Pa : 0.24732 MeV, $7/2^+$ level excitation.
 Fig. 44 Cross section of ^{231}Pa : 0.272 MeV, ($9/2^-$) level excitation.
 Fig. 45 Cross section of ^{231}Pa : 0.287 MeV, ($1/2^+$) level excitation.
 Fig. 46 Cross section of ^{231}Pa : 0.31795 MeV, ($3/2^+$) level excitation.
 Fig. 47 Cross section of ^{231}Pa : 0.320209 MeV, $3/2^-$ level excitation.
 Fig. 48 Cross section of ^{231}Pa : 0.340 MeV, ($11/2^-$) level excitation.
 Fig. 49 Cross section of ^{231}Pa : 0.35184 MeV, ($5/2^-$) level excitation.
 Fig. 50 Total inelastic scattering cross section of ^{231}Pa .
 Fig. 51 Total inelastic scattering cross section of ^{231}Pa .
 Fig. 52 Continuum inelastic scattering cross section ^{231}Pa .
 Fig. 53 Capture cross section of ^{231}Pa .
 Fig. 54 Fission cross section of ^{231}Pa .
 Fig. 55 Chance fission contributions to the fission cross section of ^{231}Pa .
 Fig. 56 Fission cross sections of ^{229}Pa , ^{231}Pa .
 Fig. 57 Fission cross section of ^{230}Pa .
 Fig. 58 ($n,2n$) cross section of ^{231}Pa .
 Fig. 59 ($n,3n$) cross section of ^{231}Pa .
 Fig. 60 Prompt fission neutron number of ^{231}Pa .
 Fig. 61 Prompt fission neutron number of ^{231}Pa .
 Fig. 62 Components of first neutron spectrum of ^{231}Pa for incident neutron energy 20 MeV.
 Fig. 63 Components of second neutron spectrum of ^{231}Pa for incident neutron energy 20 MeV.
 Fig. 64 Components of third neutron spectrum of ^{231}Pa for incident neutron energy 20 MeV.
 Fig. 65 Components of first neutron spectrum of ^{231}Pa for incident neutron energy 14 MeV.
 Fig. 66 Components of second neutron spectrum of ^{231}Pa for incident neutron energy 14 MeV.
 Fig. 67 Components of first neutron spectrum of ^{231}Pa for incident neutron energy 8 MeV.
 Fig. 68 Components of second neutron spectrum of ^{231}Pa for incident neutron energy 8 MeV.
 Fig. 69 Prompt fission neutron spectra for neutron incident energy 2MeV. The spectrum was plotted as a ratio to Maxwellian with average energy equal to average energy of fission neutrons $\langle E_m \rangle = 1.949\text{MeV}$.
 Fig. 70 The same as in Fig.69 for $E_n=7\text{MeV}$. Average energy of post fission neutrons $\langle E_m \rangle = 1.970\text{MeV}$ was used for data normalization.
 Fig. 71 The same as in Fig. 69 for $E_n=14\text{MeV}$. $\langle E_m \rangle = 1.903\text{MeV}$.
 Fig. 72 The same as in Fig. 69 for $E_n=20\text{MeV}$. $\langle E_m \rangle = 1.947\text{MeV}$.
 Fig. 73. Dependence of average energy of prompt fission neutrons on incident energy.

- Fig. 74 Comparison of $(n,n'\gamma)$ reaction neutron spectra of ^{231}Pa for incident neutron energy 20 MeV.
- Fig. 75 Comparison of $(n,n'\gamma)$ reaction neutron spectra of ^{231}Pa for incident neutron energy 14 MeV.
- Fig. 76 Comparison of $(n,n'\gamma)$ reaction neutron spectra of ^{231}Pa for incident neutron energy 10 MeV.
- Fig. 77 Comparison of $(n,n'\gamma)$ reaction neutron spectra of ^{231}Pa for incident neutron energy 8 MeV.
- Fig. 78 Comparison of $(n,n'\gamma)$ reaction neutron spectra of ^{231}Pa for incident neutron energy 6 MeV.
- Fig. 79 Comparison of $(n,n'\gamma)$ reaction neutron spectra of ^{231}Pa for incident neutron energy 4 MeV.
- Fig. 80 Comparison of $(n,2n)$ reaction neutron spectra of ^{231}Pa for incident neutron energy 20 MeV.
- Fig. 81 Comparison of $(n,2n)$ reaction neutron spectra of ^{231}Pa for incident neutron energy 14 MeV.
- Fig. 82 Comparison of $(n,2n)$ reaction neutron spectra of ^{231}Pa for incident neutron energy 10 MeV.
- Fig. 83 Comparison of $(n,2n)$ reaction neutron spectra of ^{231}Pa for incident neutron energy 8 MeV.
- Fig. 84 Comparison of $(n,3n)$ reaction neutron spectra of ^{231}Pa for incident neutron energy 20 MeV.
- Fig. 85 Comparison of $(n,3n)$ reaction neutron spectra of ^{231}Pa for incident neutron energy 14 MeV.

^{231}Pa CUMULATIVE SUM OF LEVELS

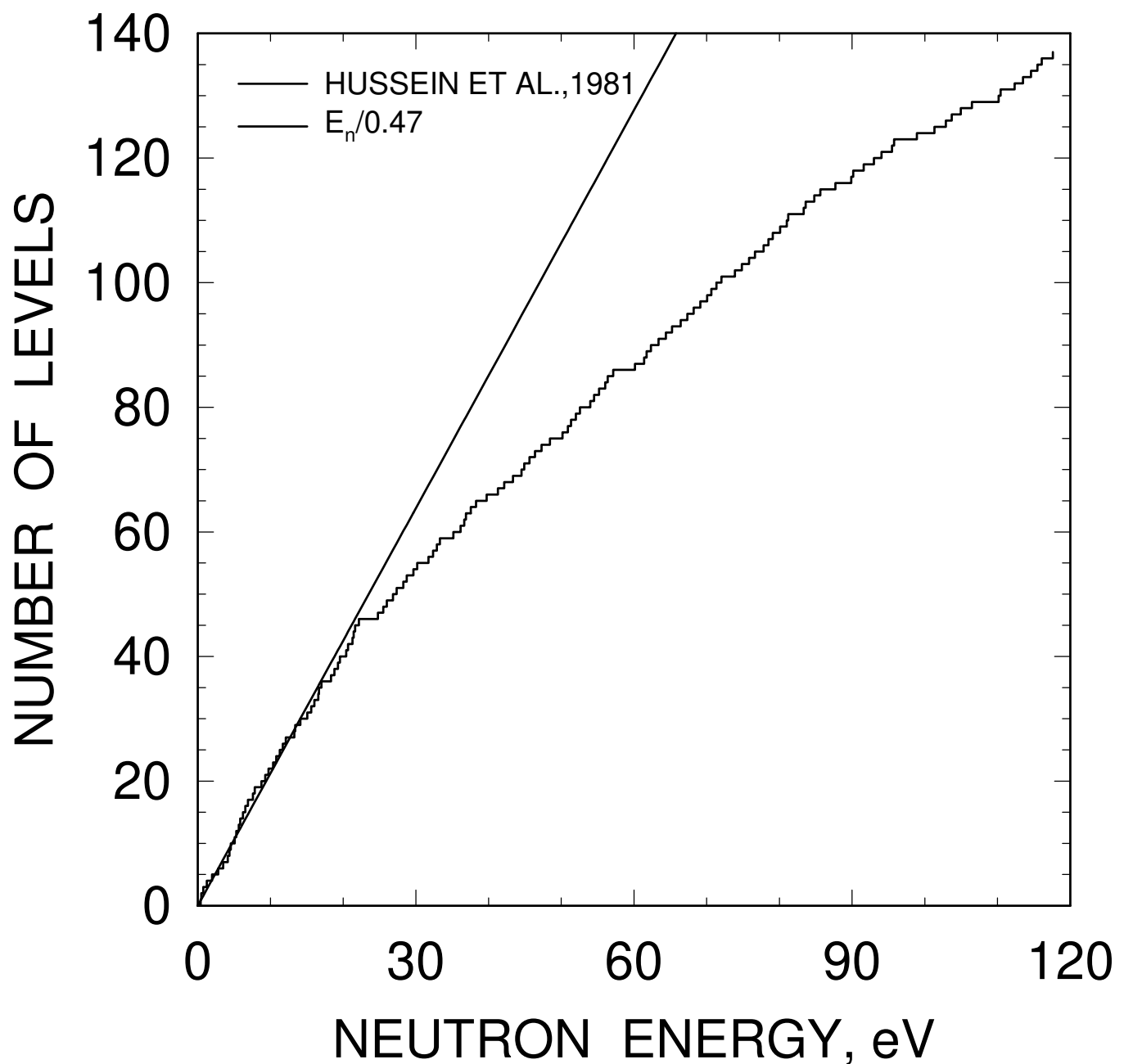


FIG. 1

^{231}Pa CUMULATIVE SUM OF REDUCED NEUTRON WIDTHS

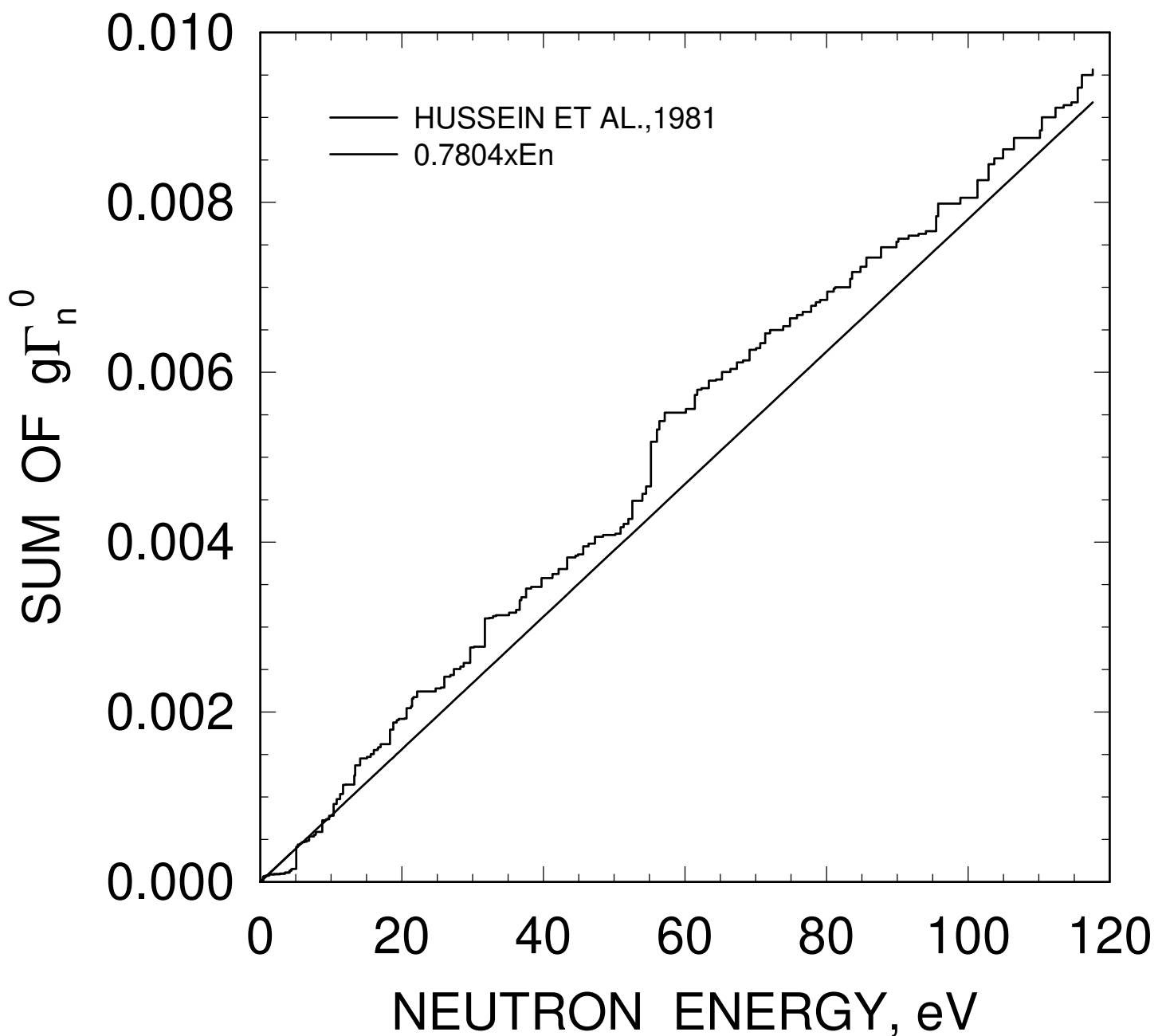


FIG. 2

^{231}Pa LEVEL SPACING DISTRIBUTION

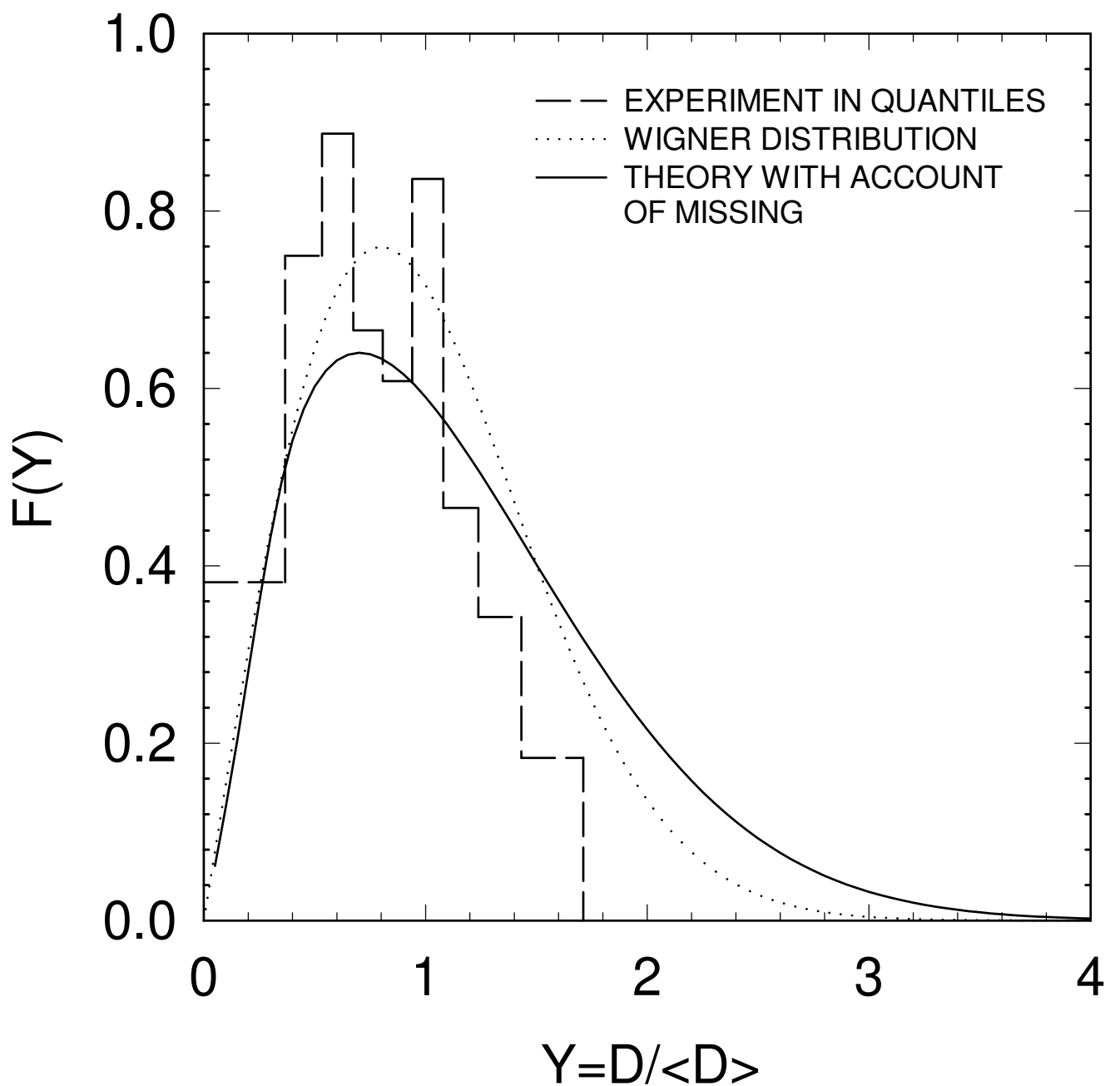


FIG. 3

^{231}Pa REDUCED NEUTRON WIDTH DISTRIBUTION

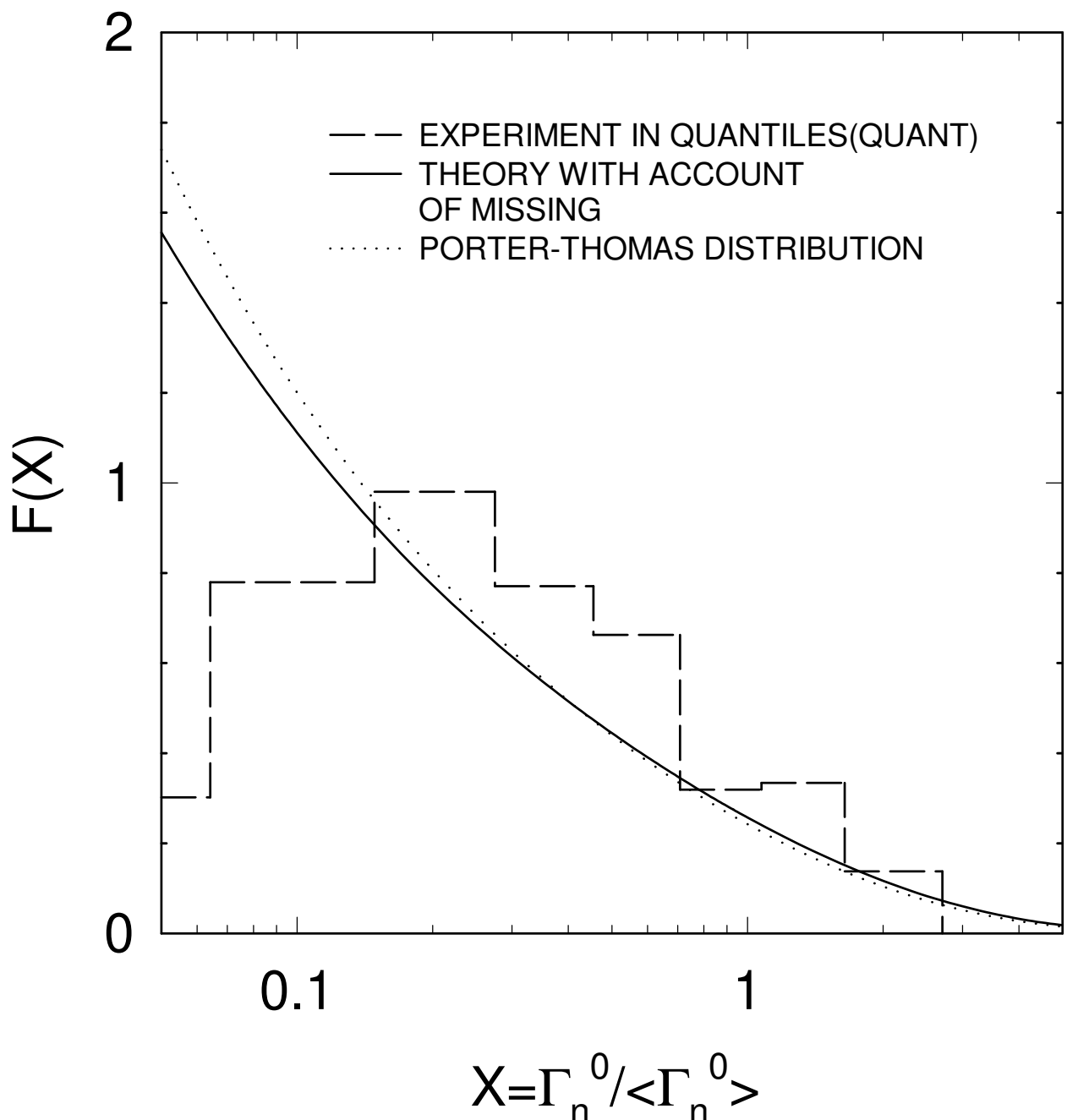


FIG. 4

^{231}Pa CUMULATIVE PORTER-THOMAS DISTRIBUTION OF REDUCED NEUTRON WIDTHS

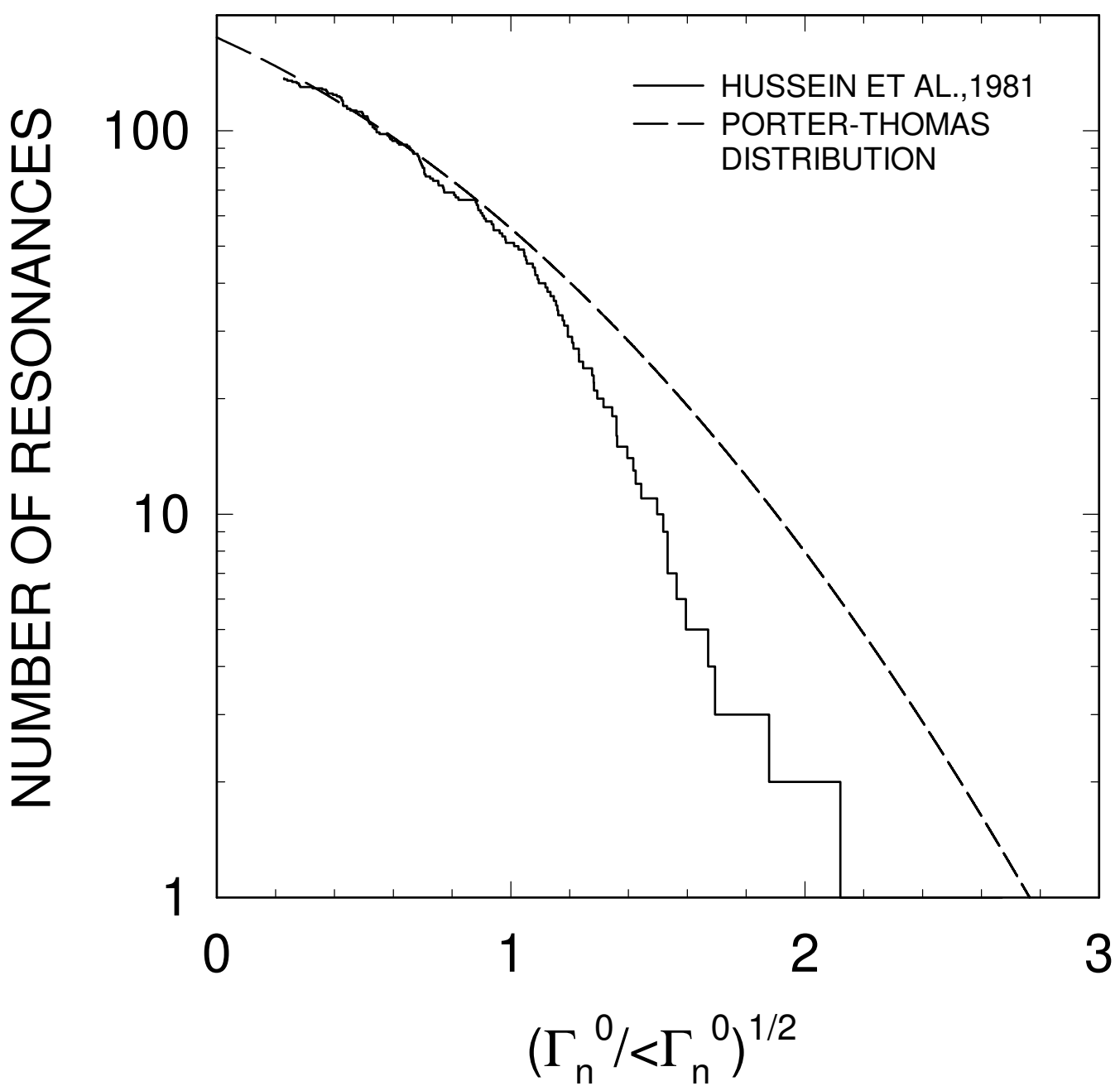


FIG. 5

^{231}Pa TOTAL CROSS SECTION

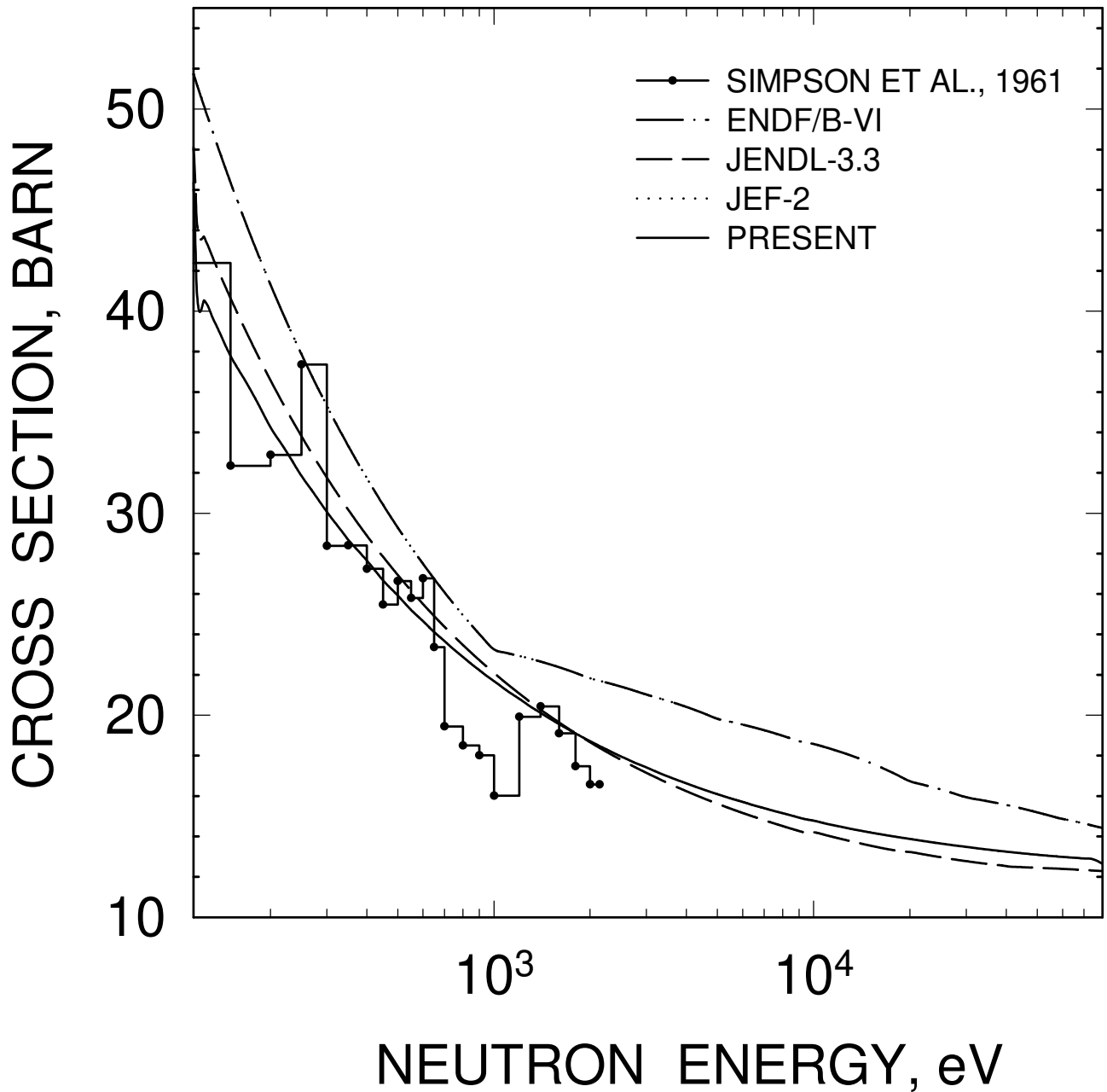


FIG. 6

^{231}Pa ELASTIC CROSS SECTION

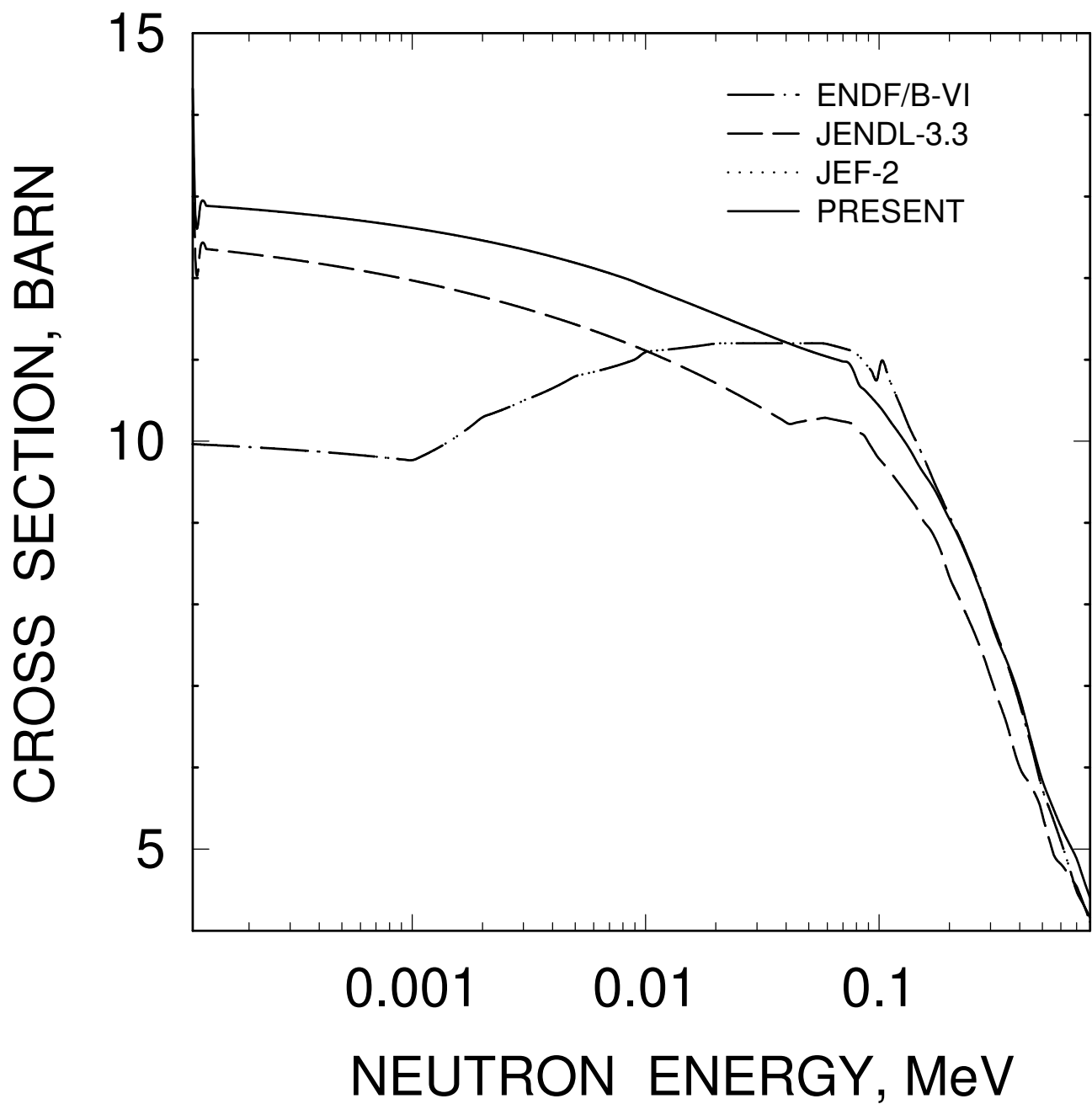


FIG. 7

^{231}Pa FISSION CROSS SECTION

CROSS SECTION, BARN

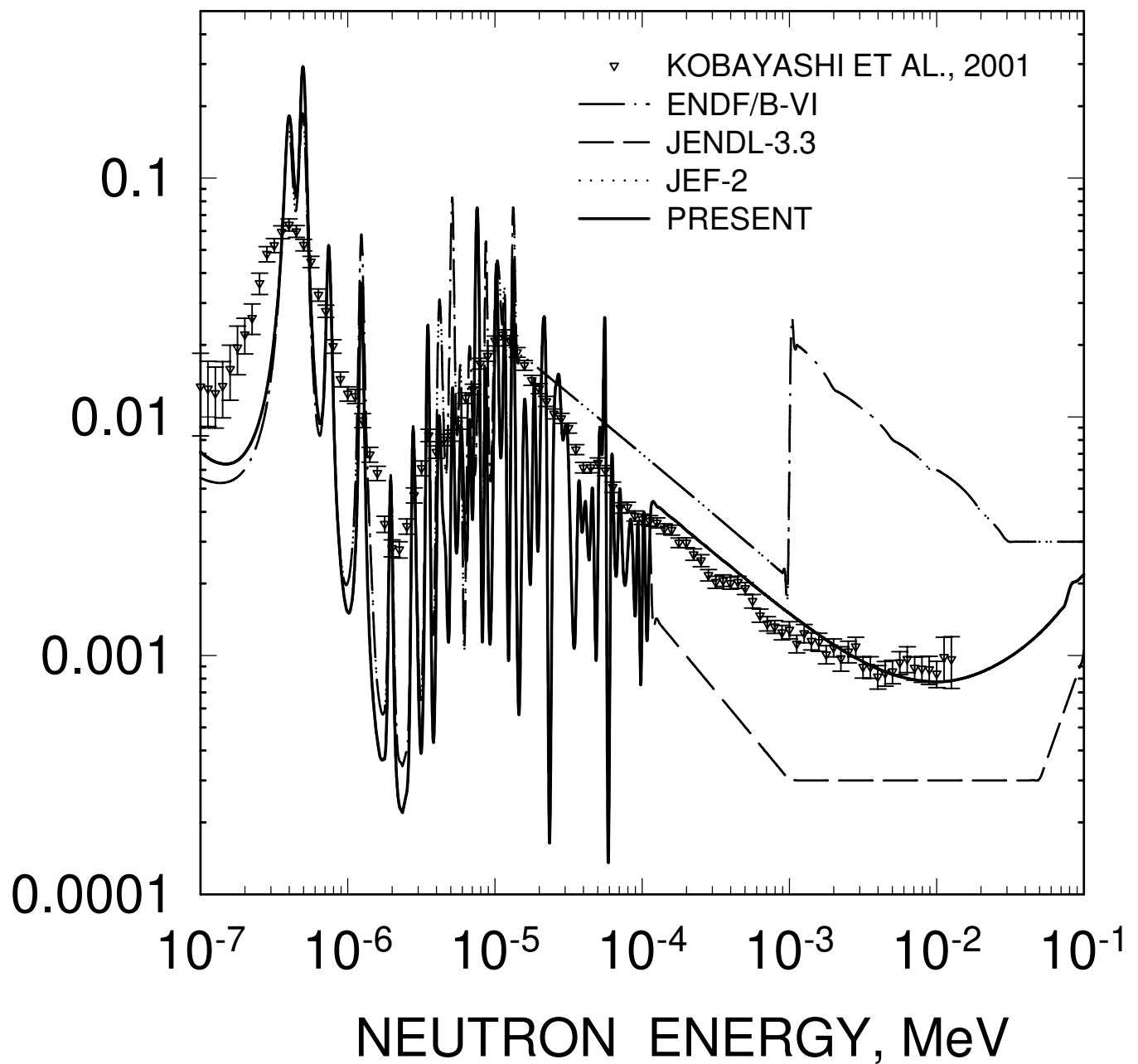


FIG. 8

^{231}Pa (n,γ) CROSS SECTION

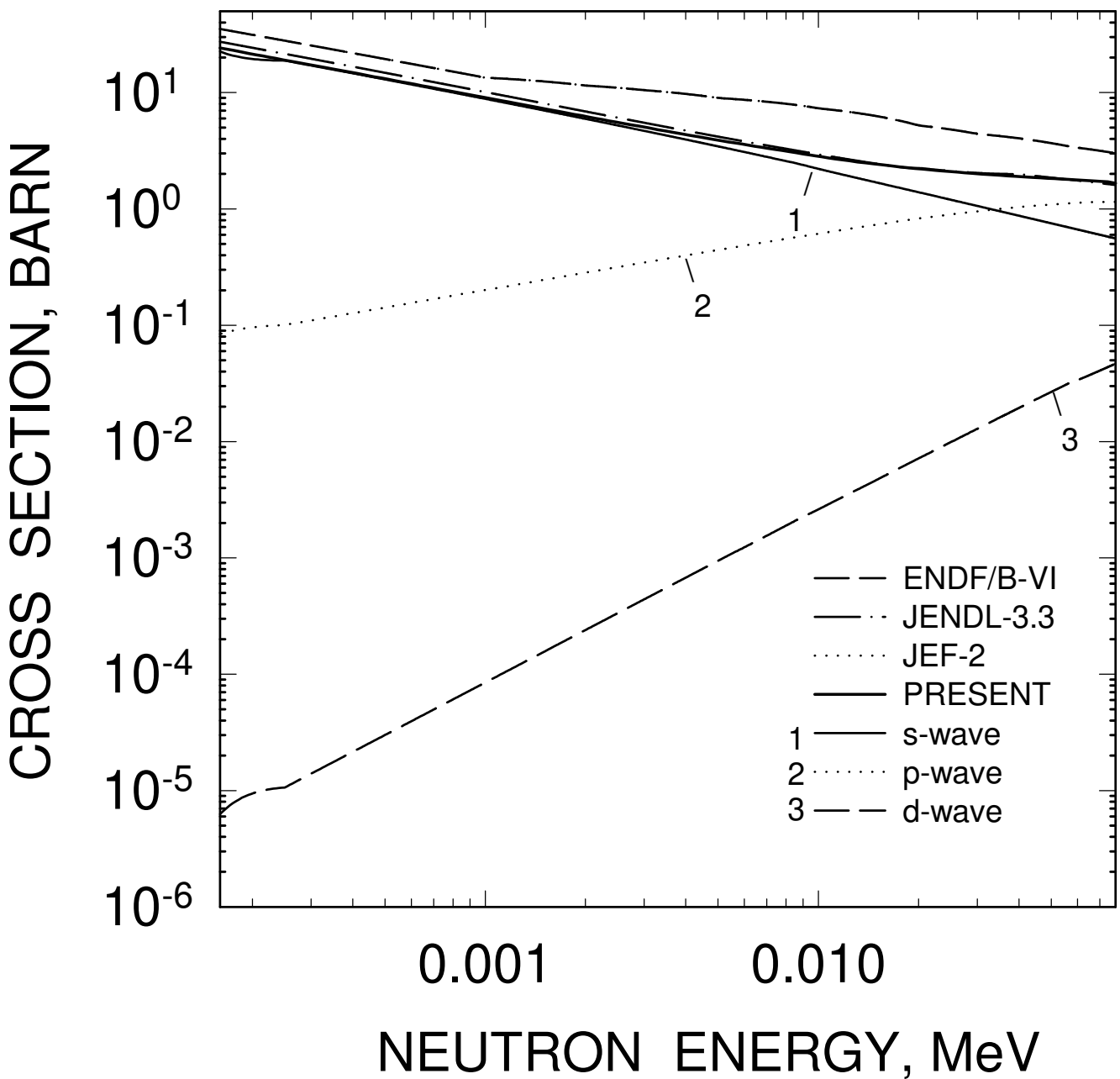


FIG. 9

^{233}Pa INELASTIC CROSS SECTION

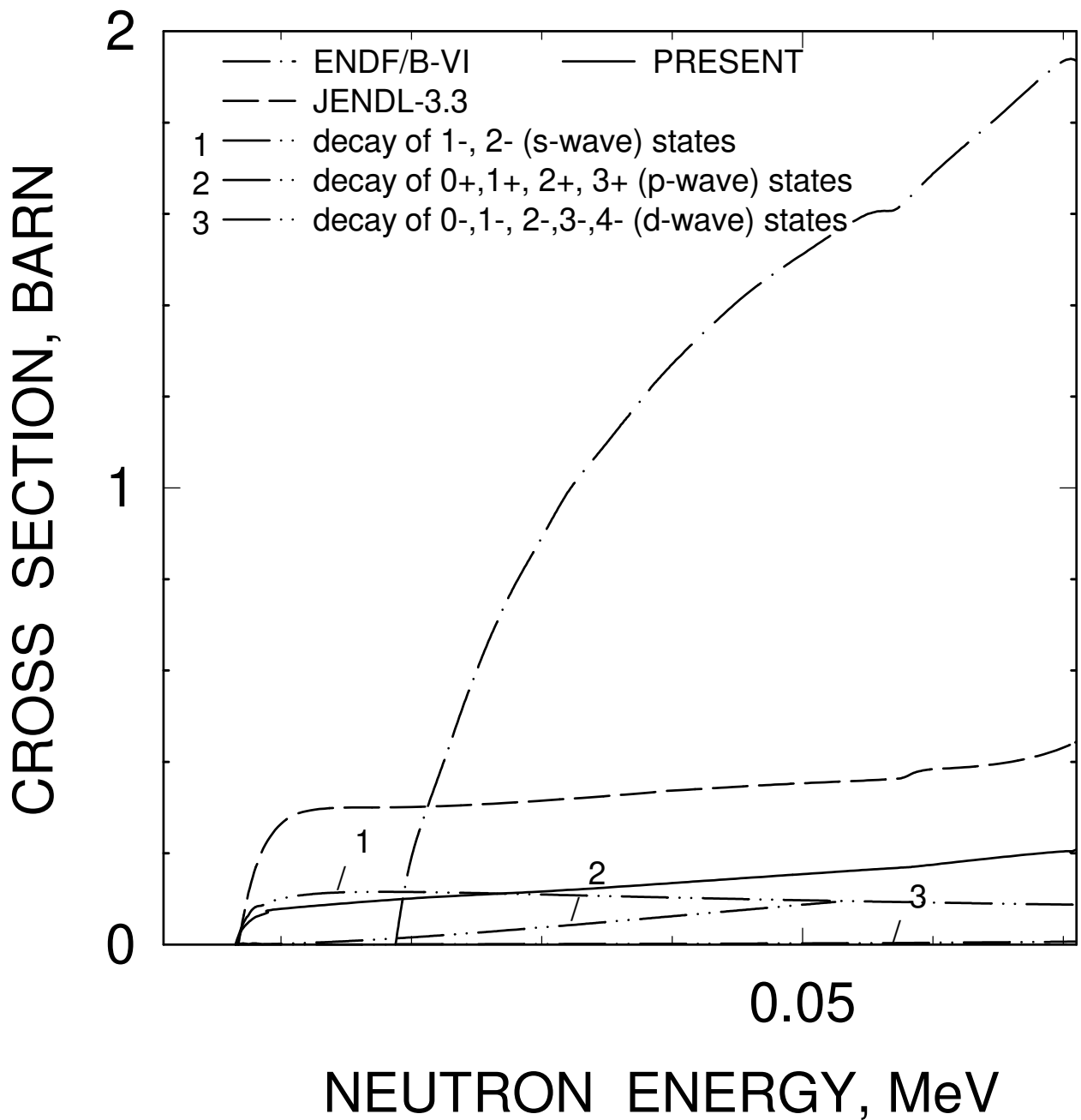


FIG. 10

^{231}Pa : AVERAGE LEVEL SPACING
($L=0$, $J=1$)

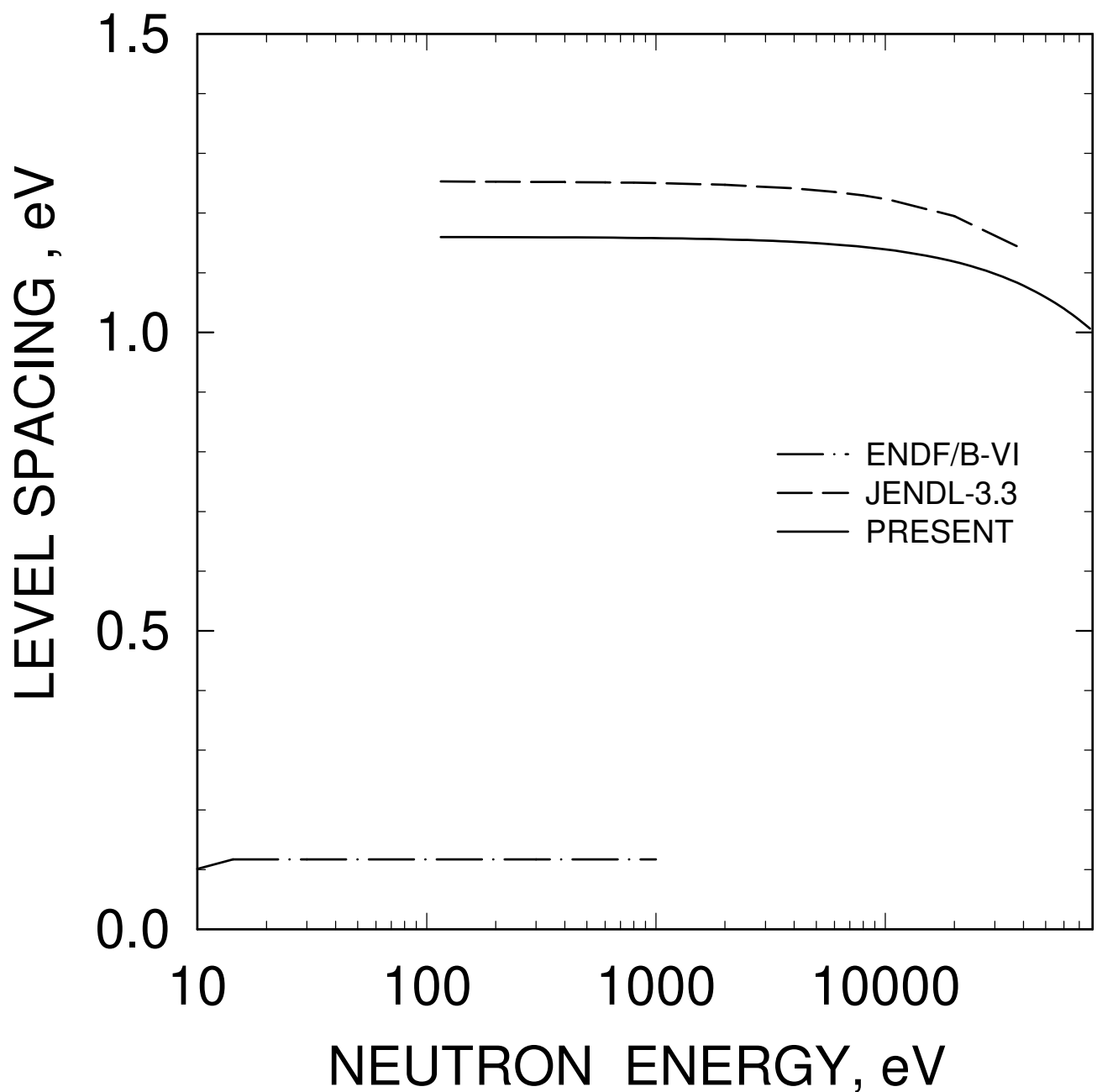


FIG. 11

^{231}Pa : AVERAGE LEVEL SPACING
(L=0, J=2)

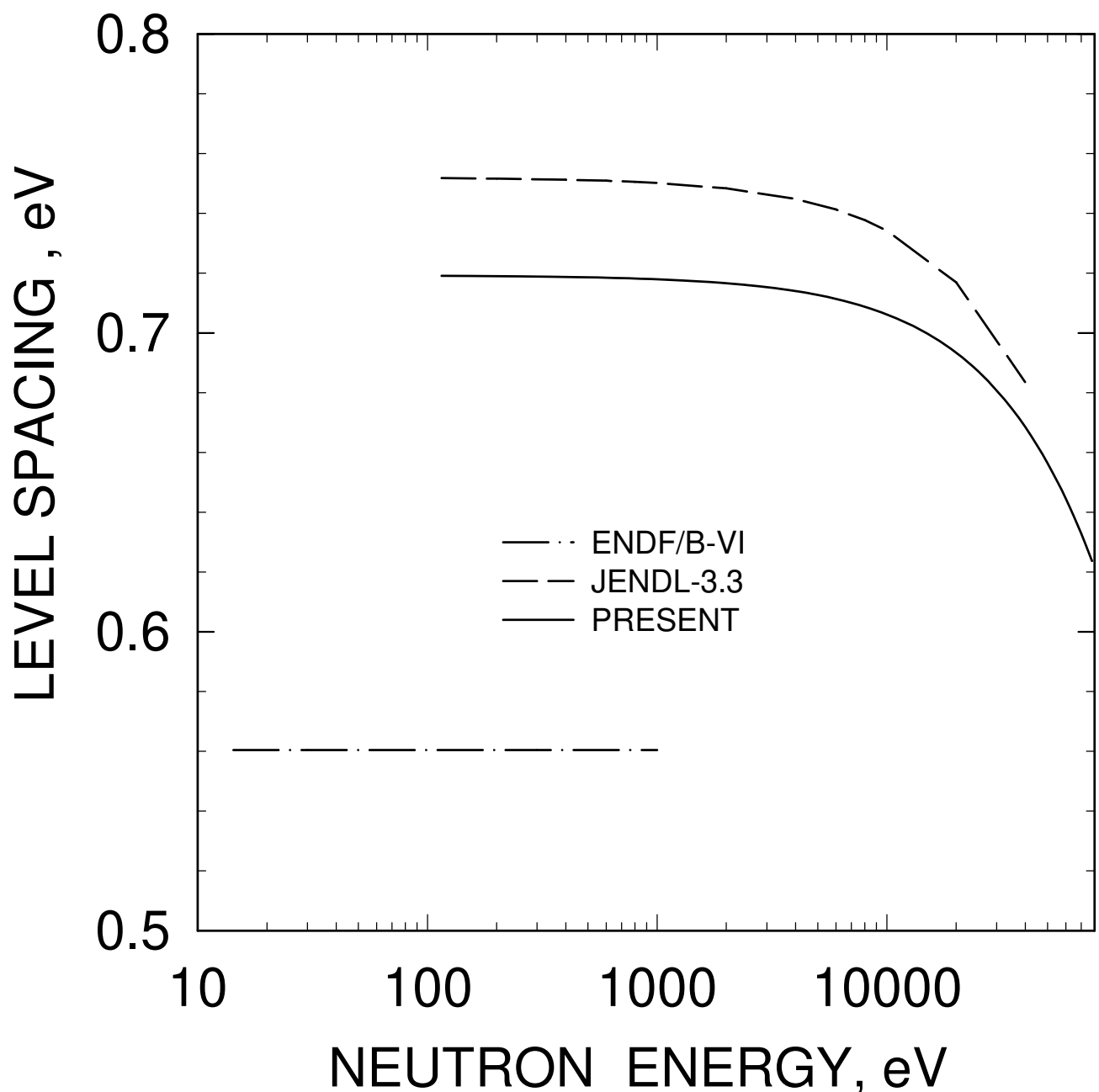


FIG. 12

^{231}Pa : AVERAGE LEVEL SPACING
(L=1, J=0)

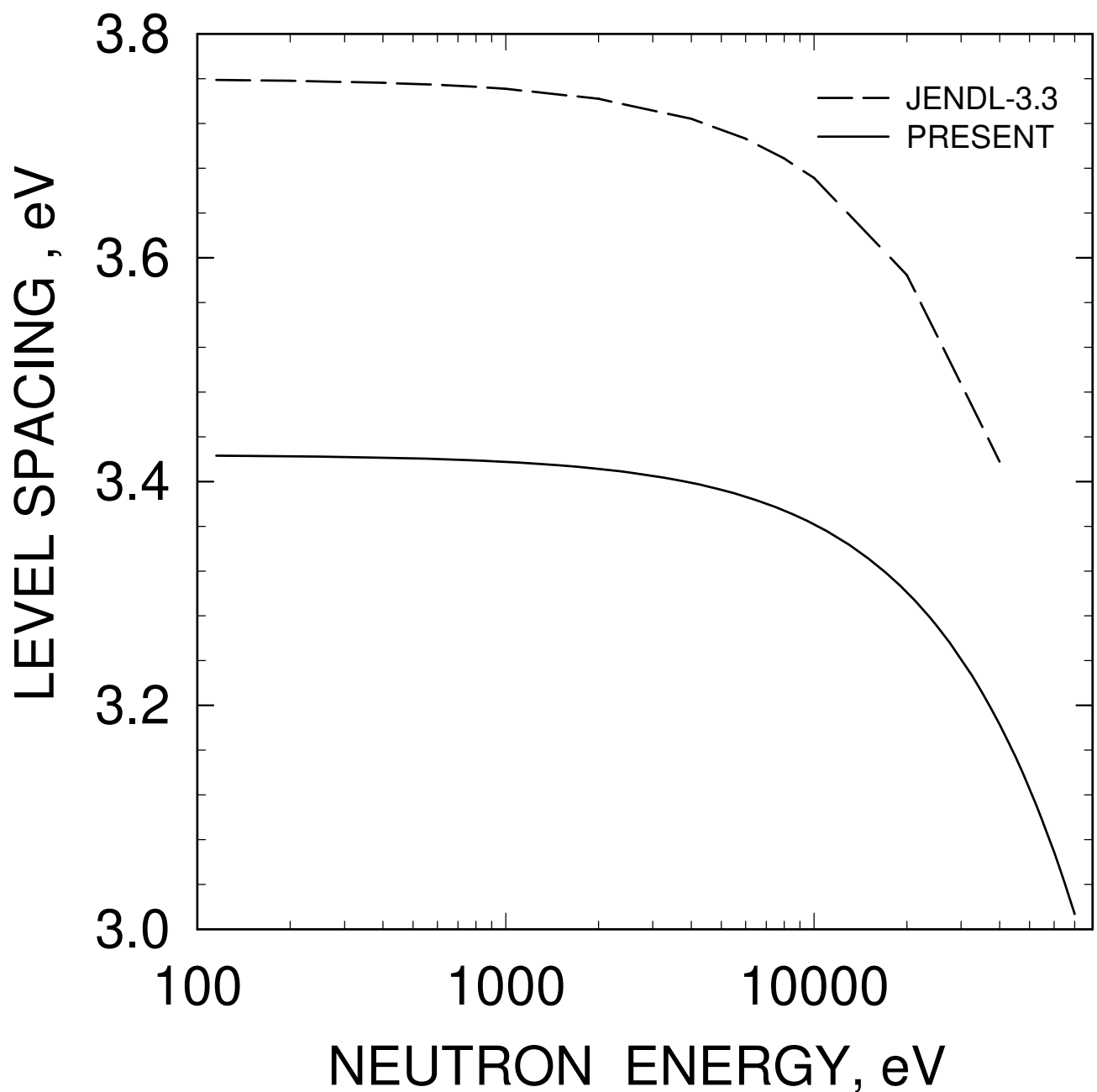


FIG. 13

^{231}Pa : AVERAGE LEVEL SPACING
(L=1, J=3)

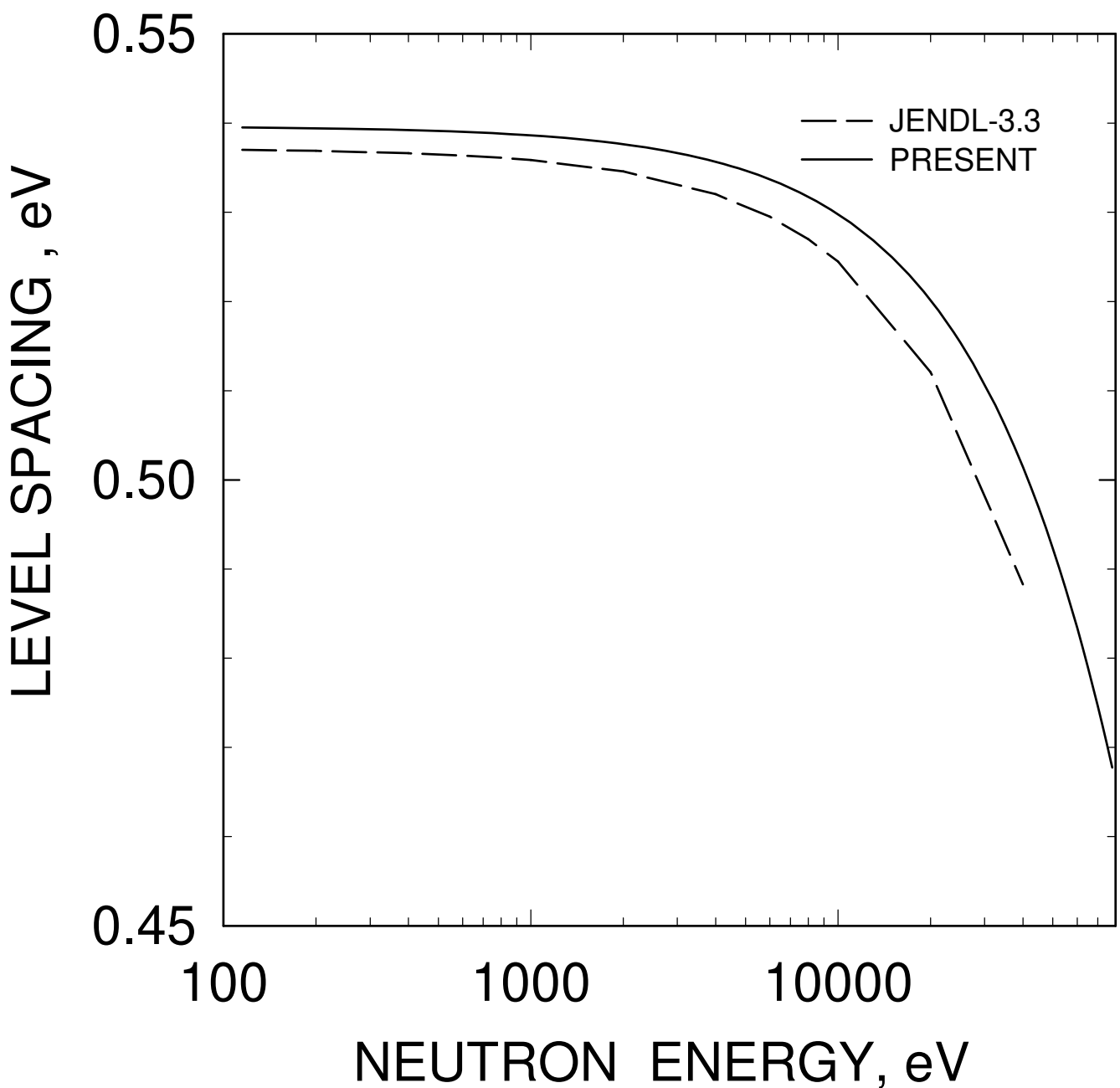


FIG. 14

^{231}Pa : AVERAGE REDUCED
NEUTRON WIDTH
(L=0, J=1)

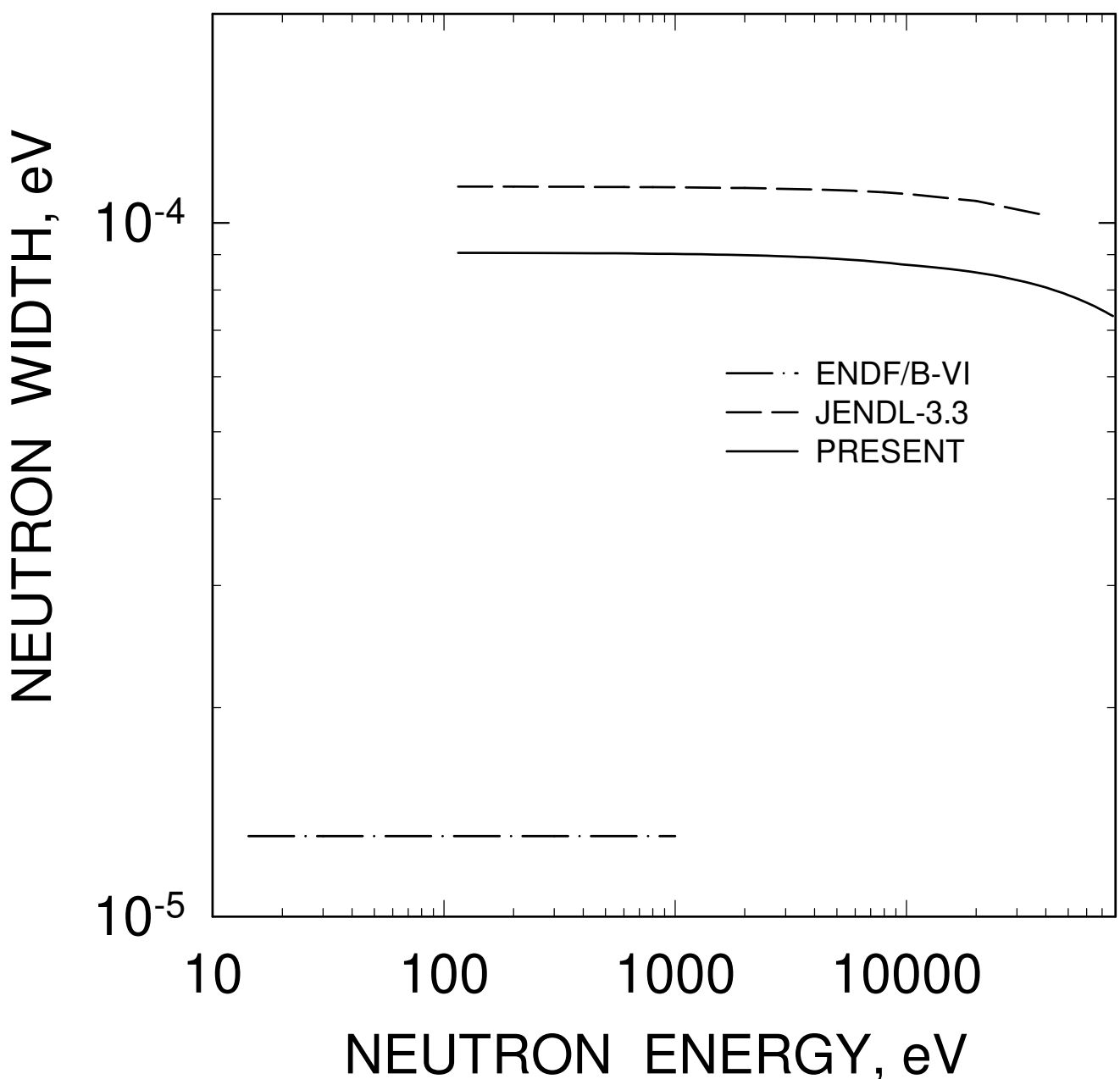


FIG. 15

^{231}Pa : AVERAGE REDUCED
NEUTRON WIDTH
(L=0, J=2)

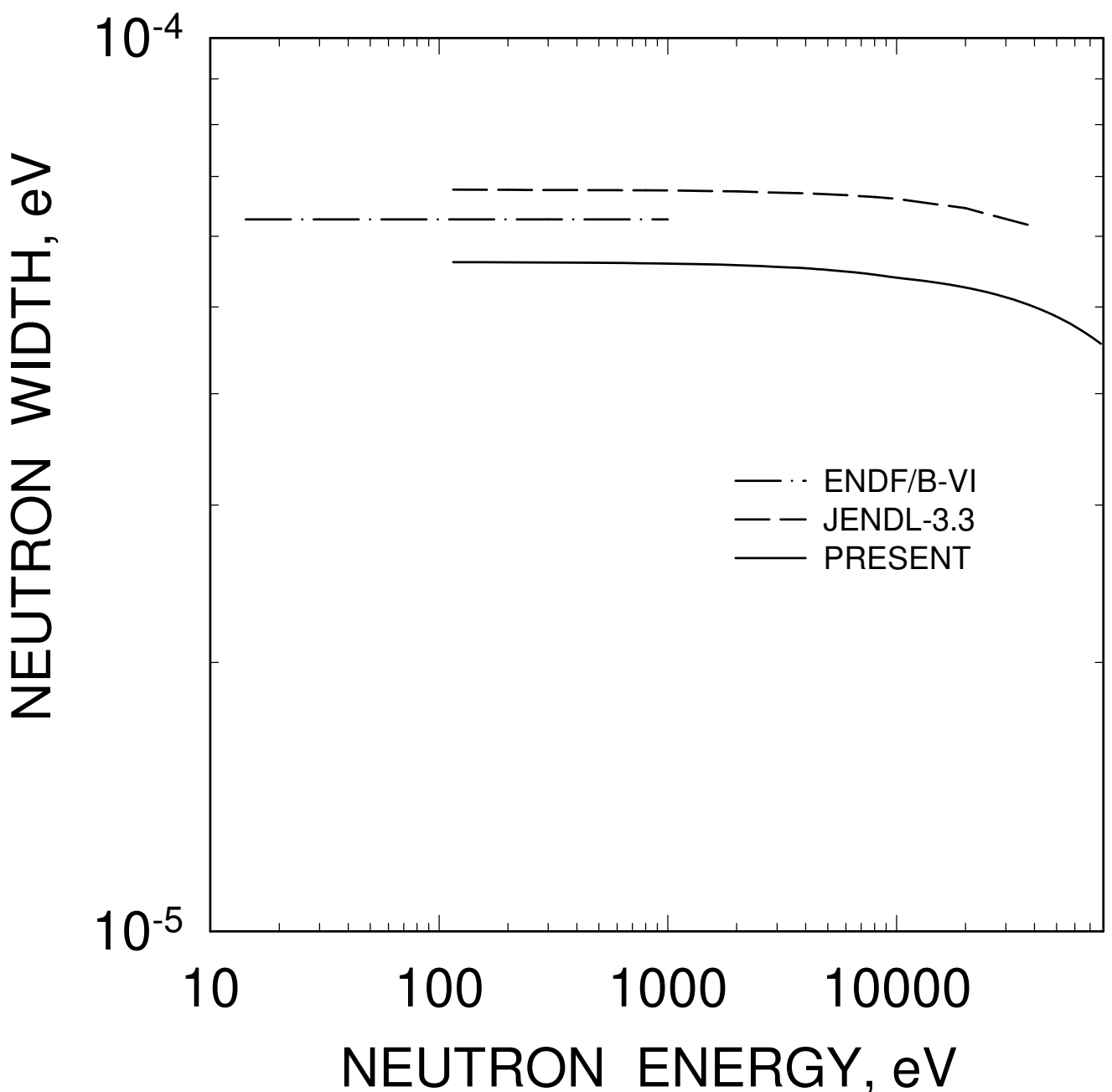


FIG. 16

^{231}Pa : AVERAGE REDUCED
NEUTRON WIDTH
($L=1$, $J=0$)

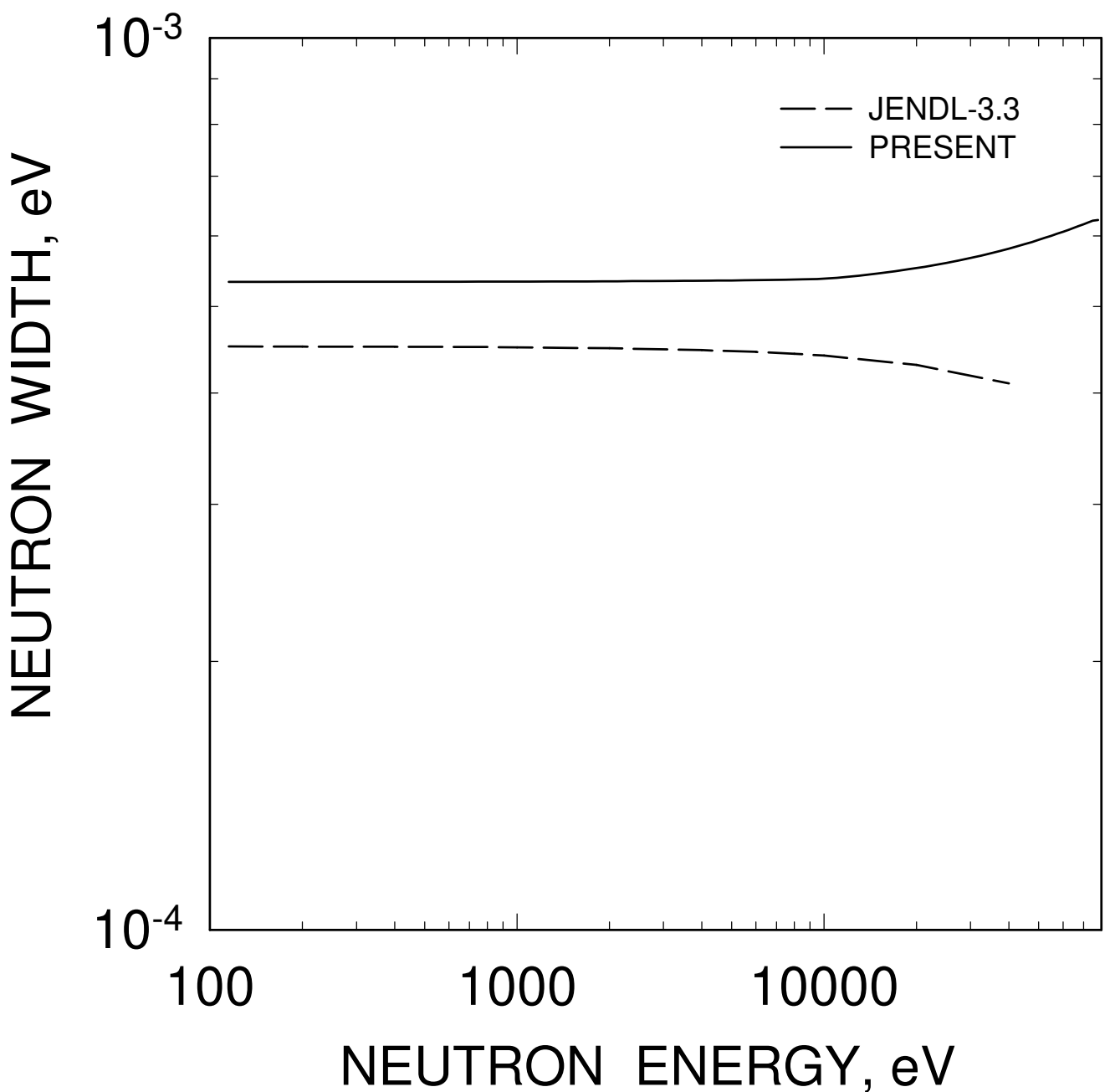


FIG. 17

^{231}Pa : AVERAGE REDUCED
NEUTRON WIDTH
($L=1$, $J=1$)

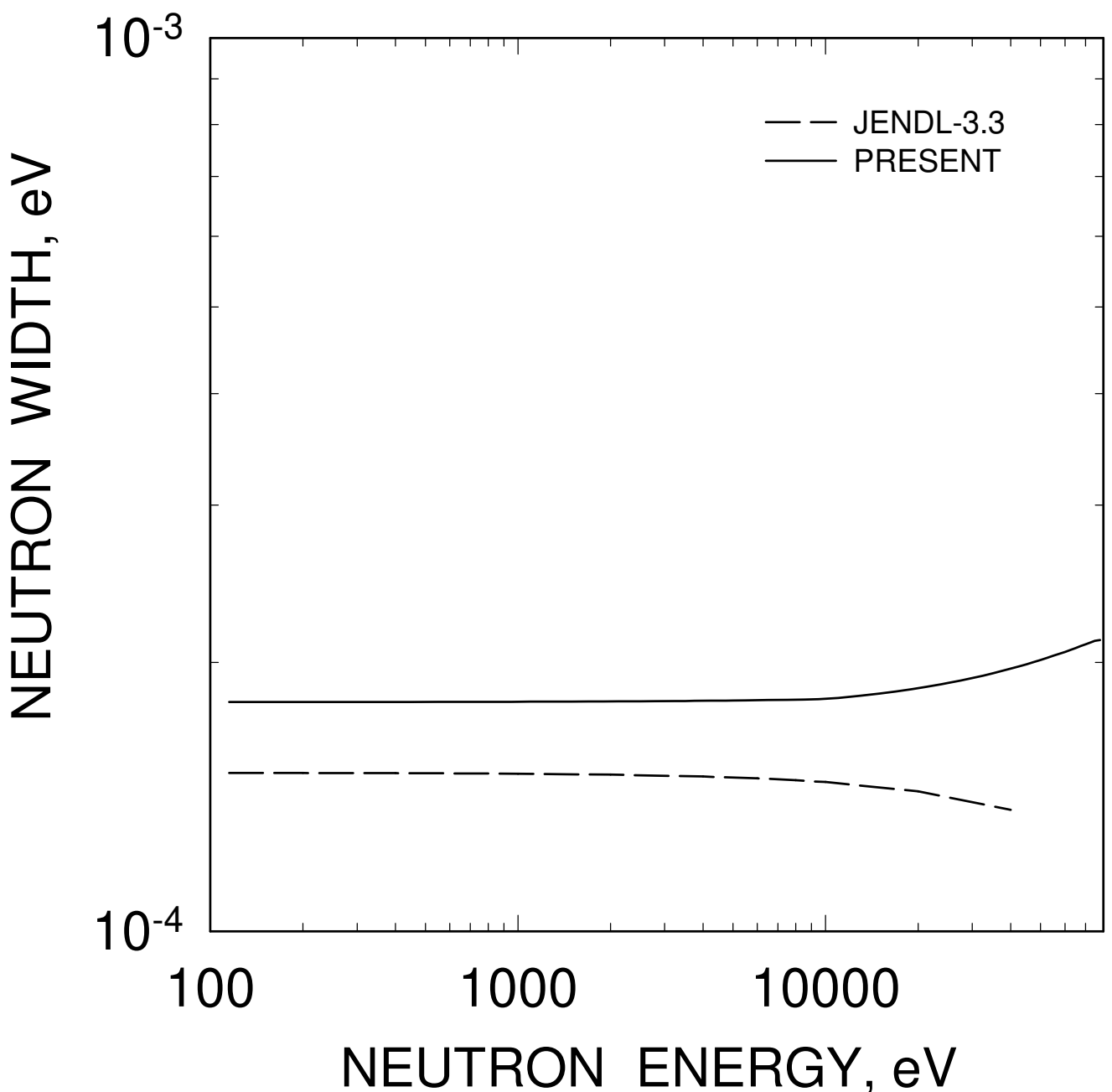


FIG. 18

^{231}Pa : AVERAGE REDUCED
NEUTRON WIDTH
($L=1$, $J=2$)

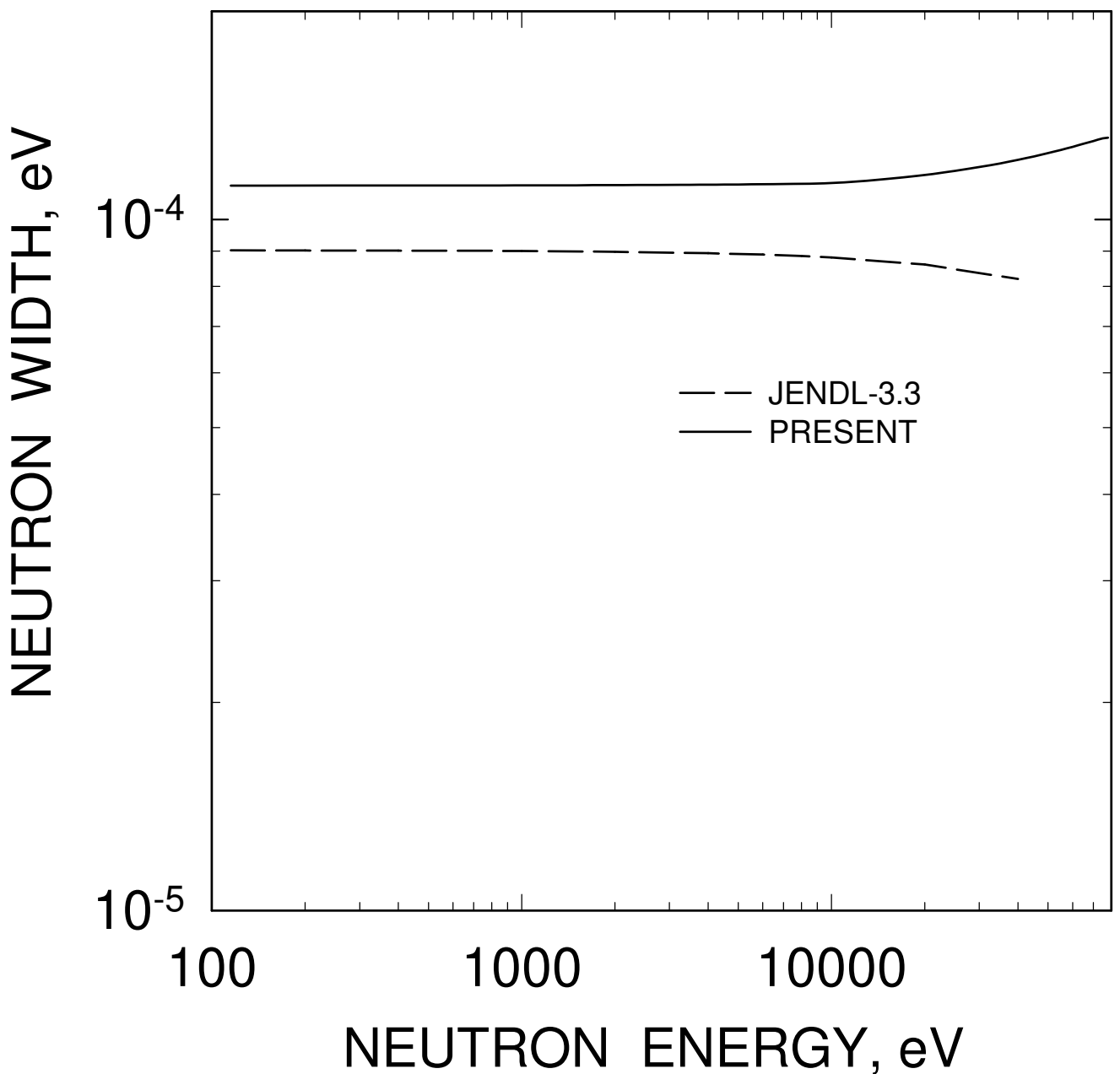


FIG. 19

^{231}Pa : AVERAGE REDUCED
NEUTRON WIDTH
($L=1$, $J=3$)

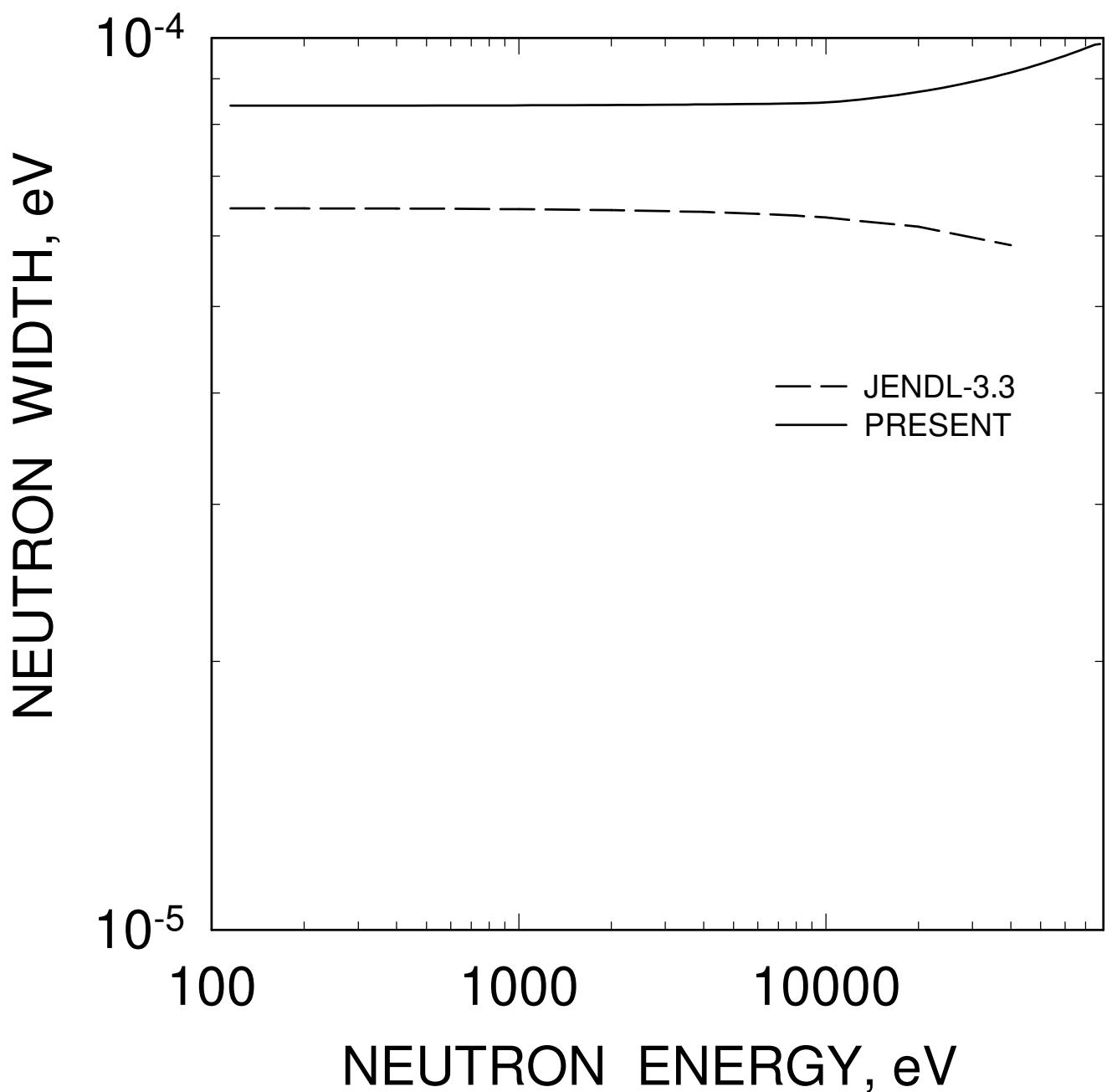


FIG. 20

^{231}Pa : AVERAGE FISSION WIDTH
(L=0, J=1)

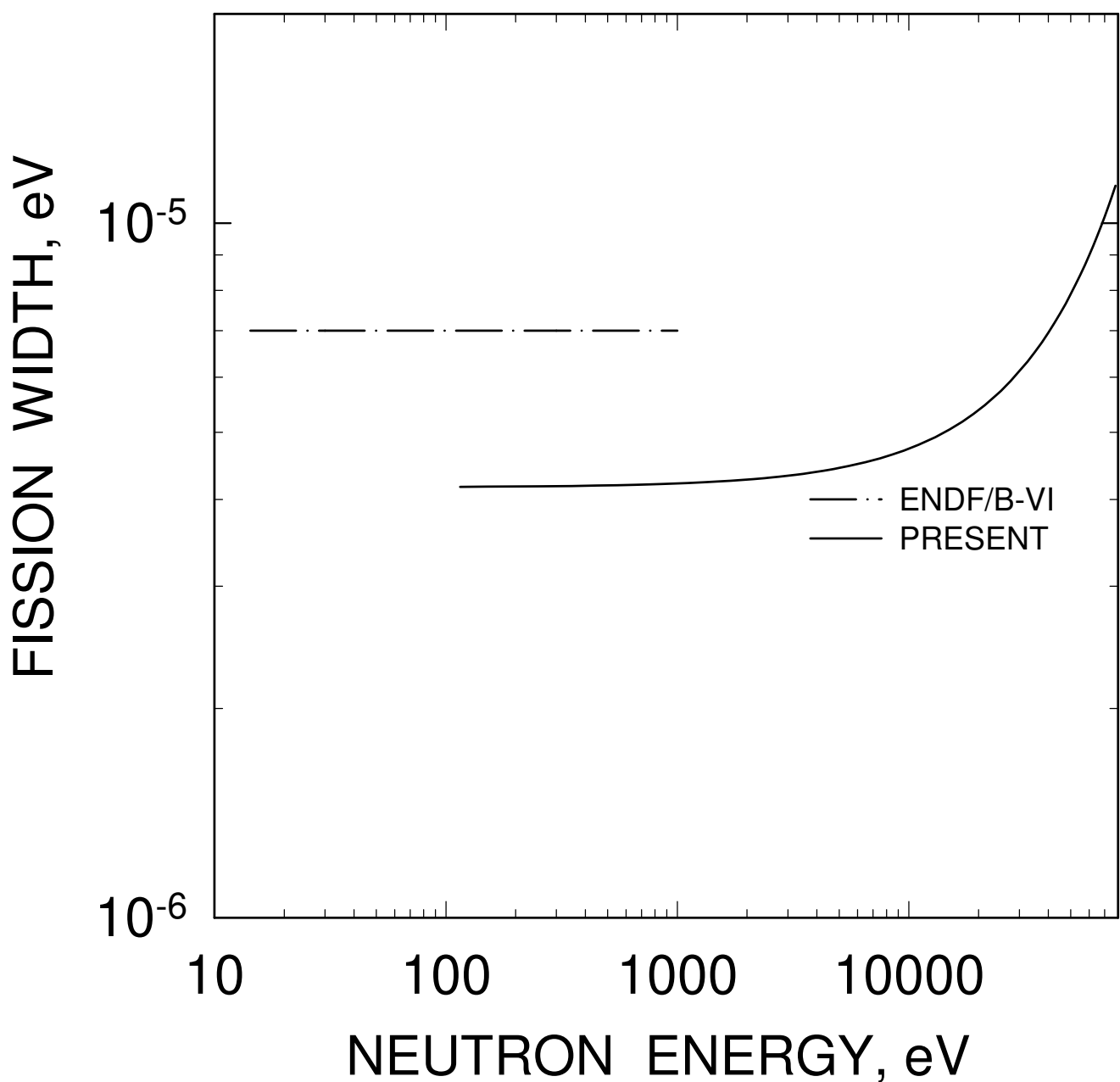


FIG. 21

^{231}Pa : AVERAGE FISSION WIDTH
(L=0, J=2)

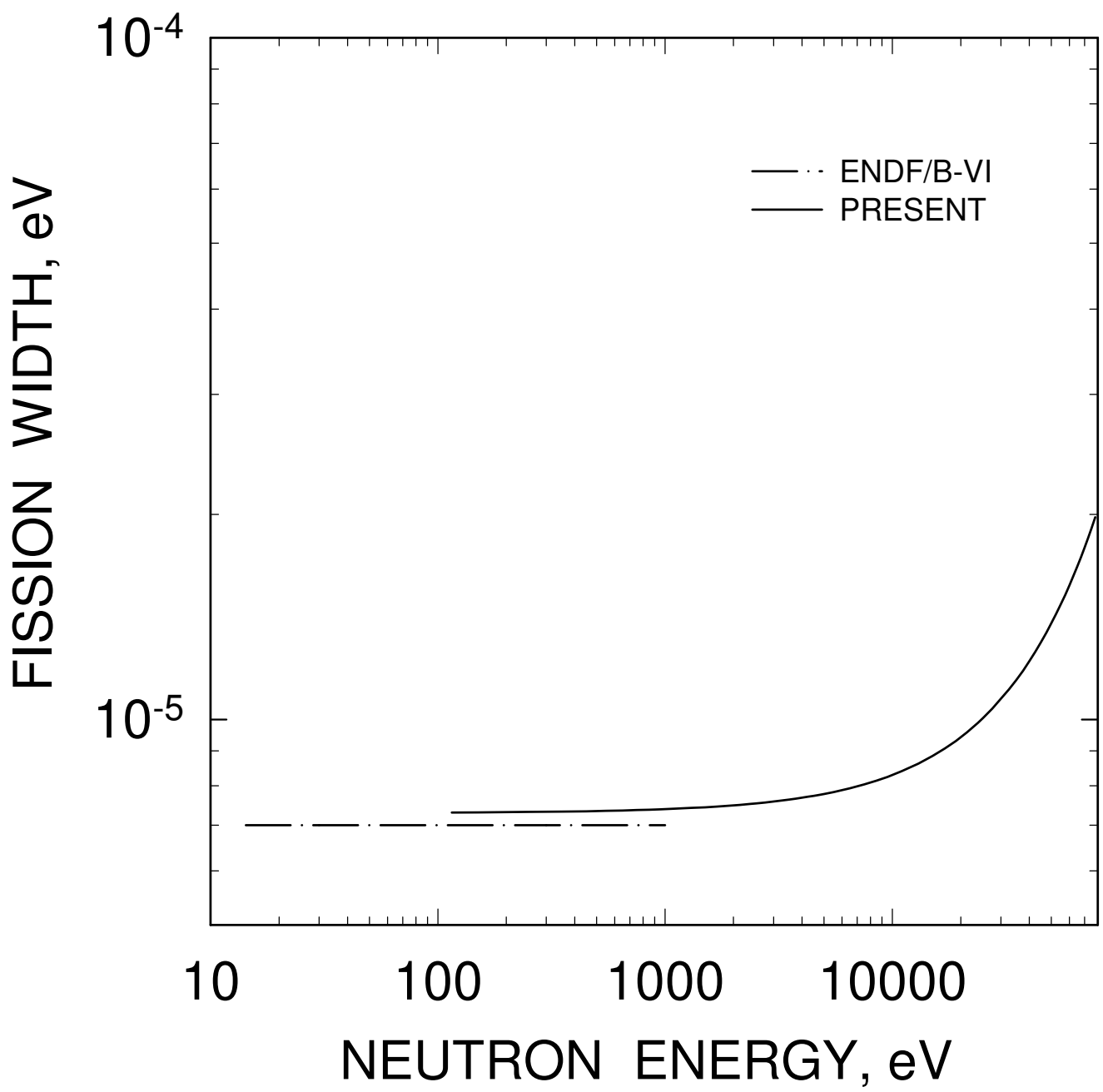


FIG. 22

^{231}Pa TOTAL CROSS SECTION

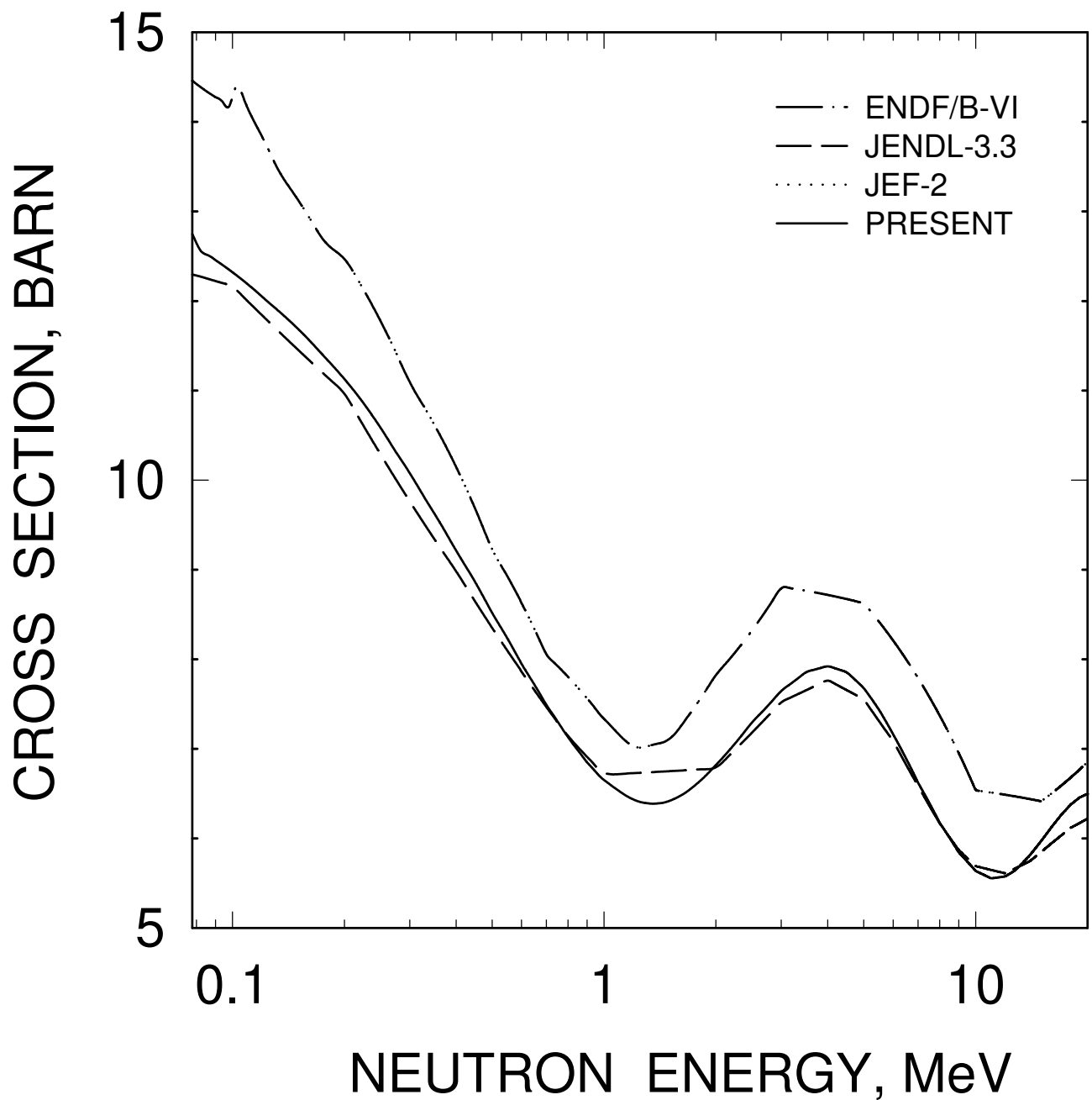


FIG. 23

^{231}Pa ELASTIC CROSS SECTION

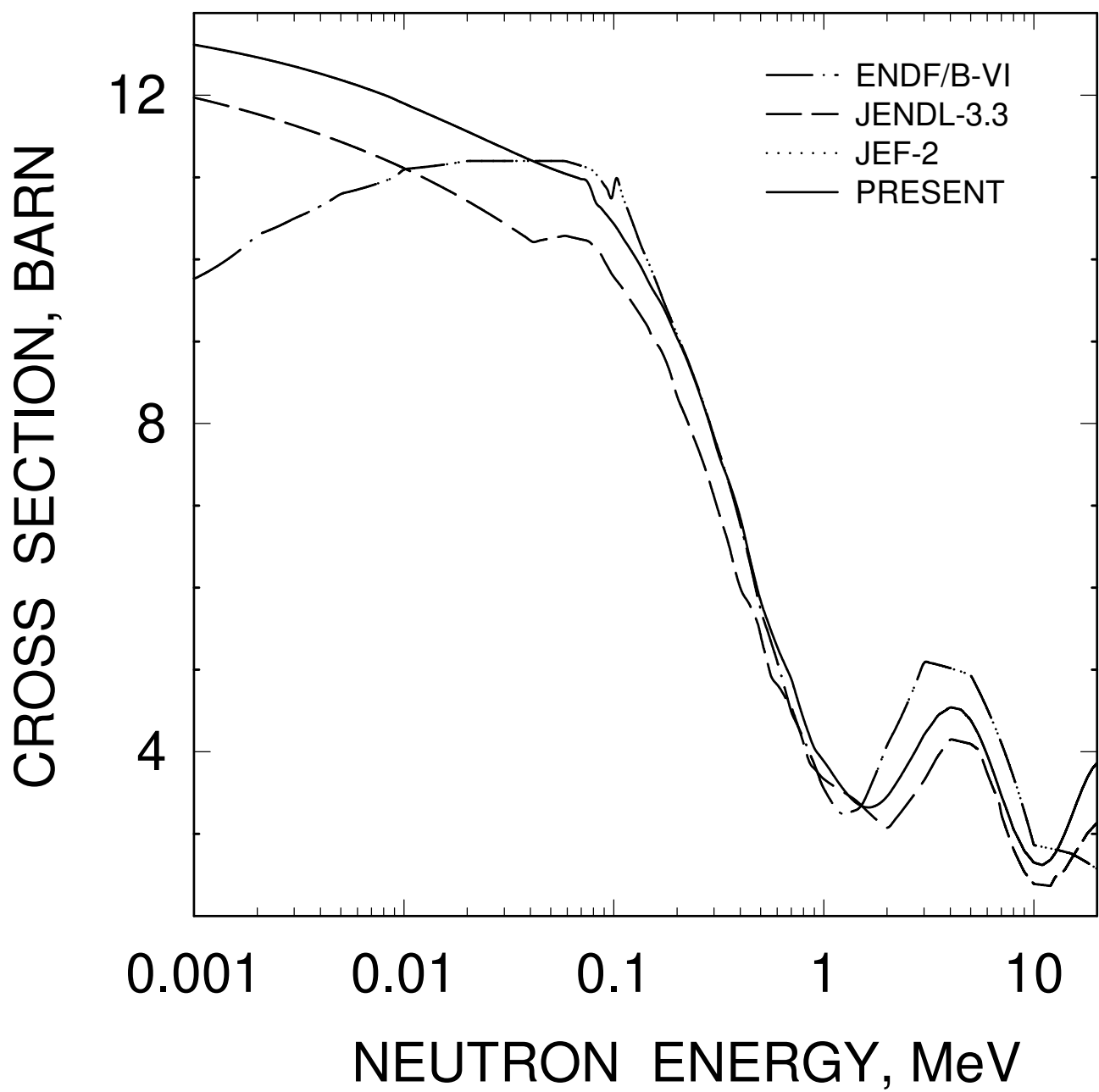


FIG. 24

^{231}Pa

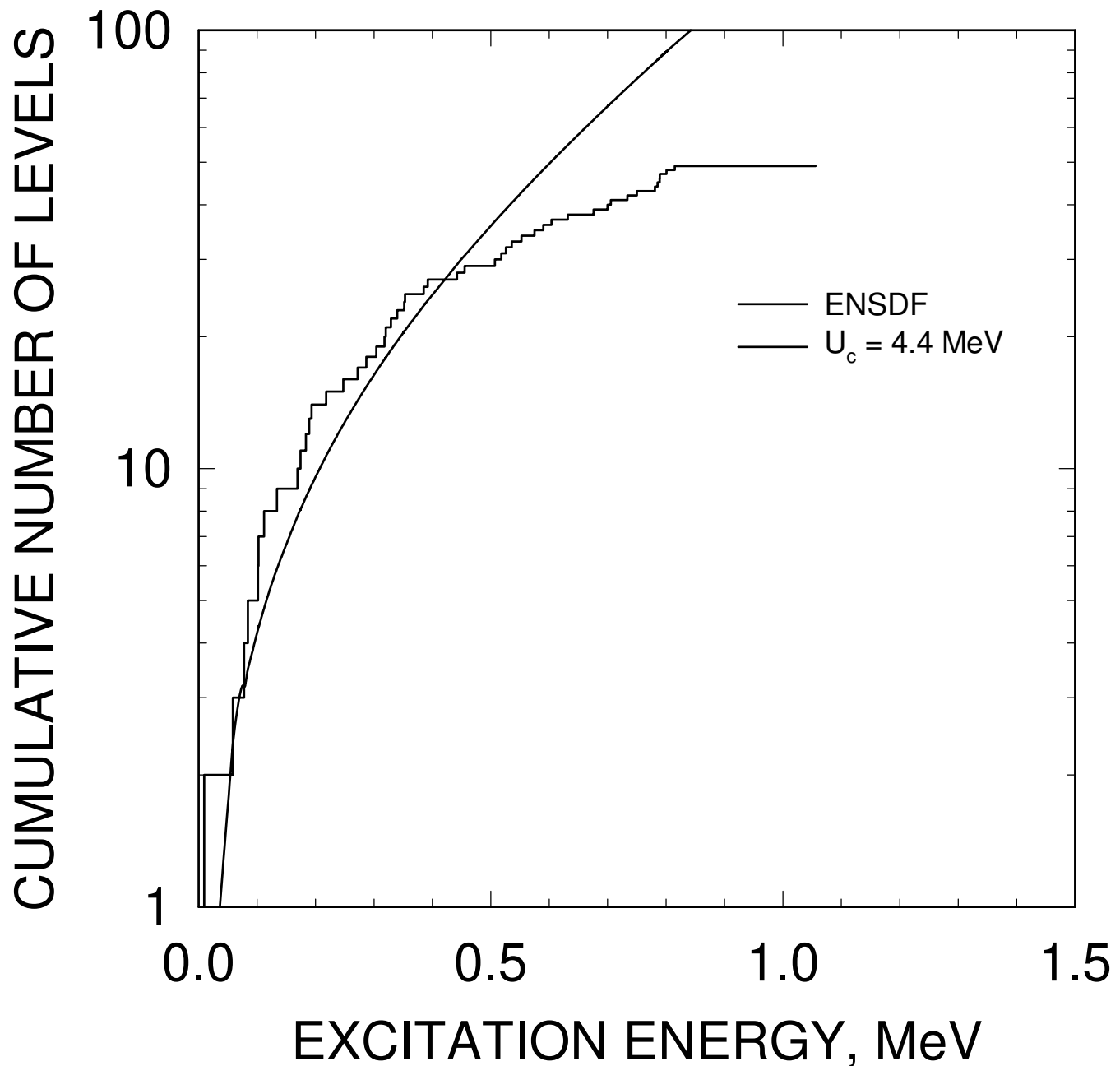


FIG. 25

^{232}Pa

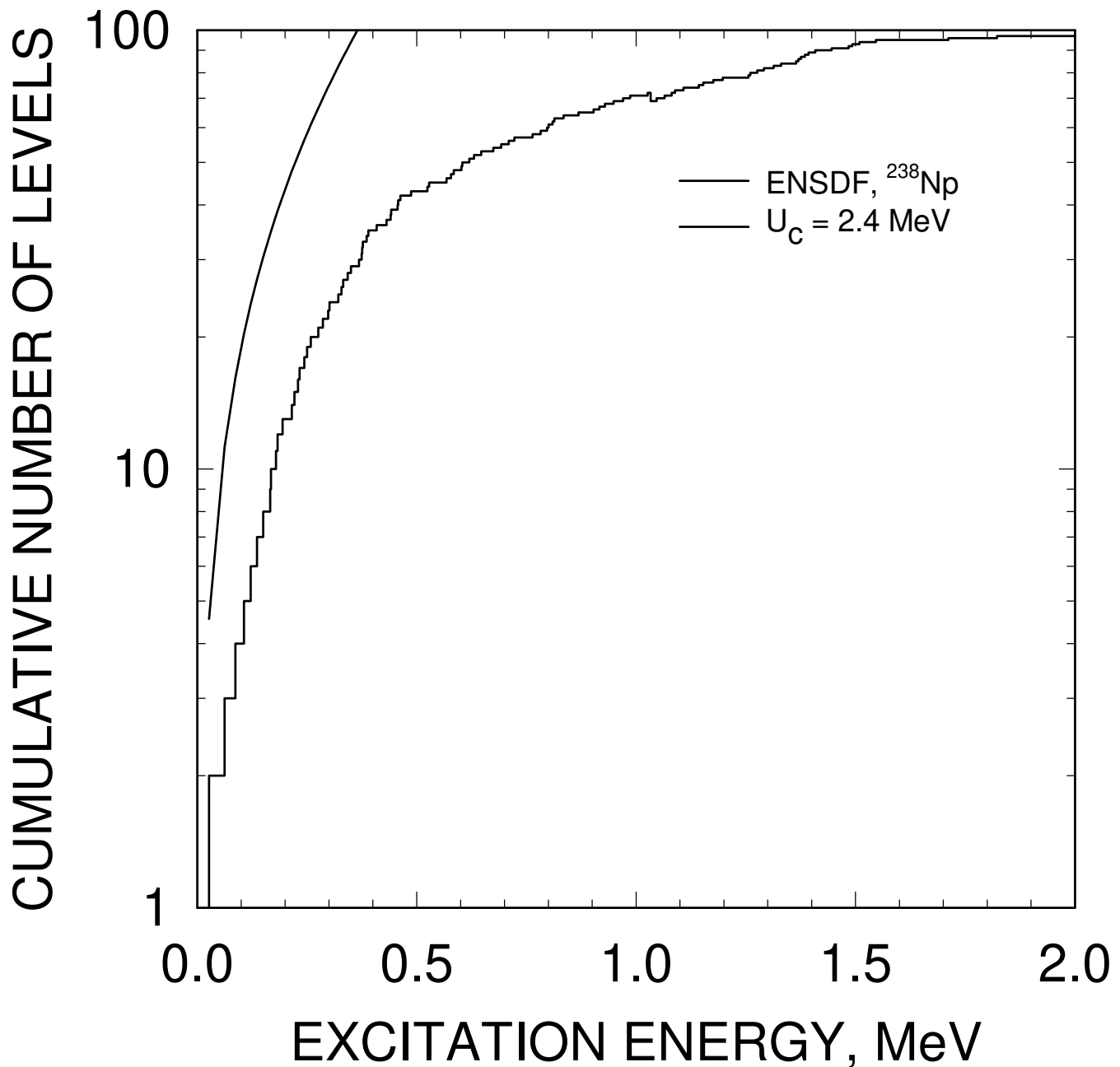


FIG. 26

^{231}Pa

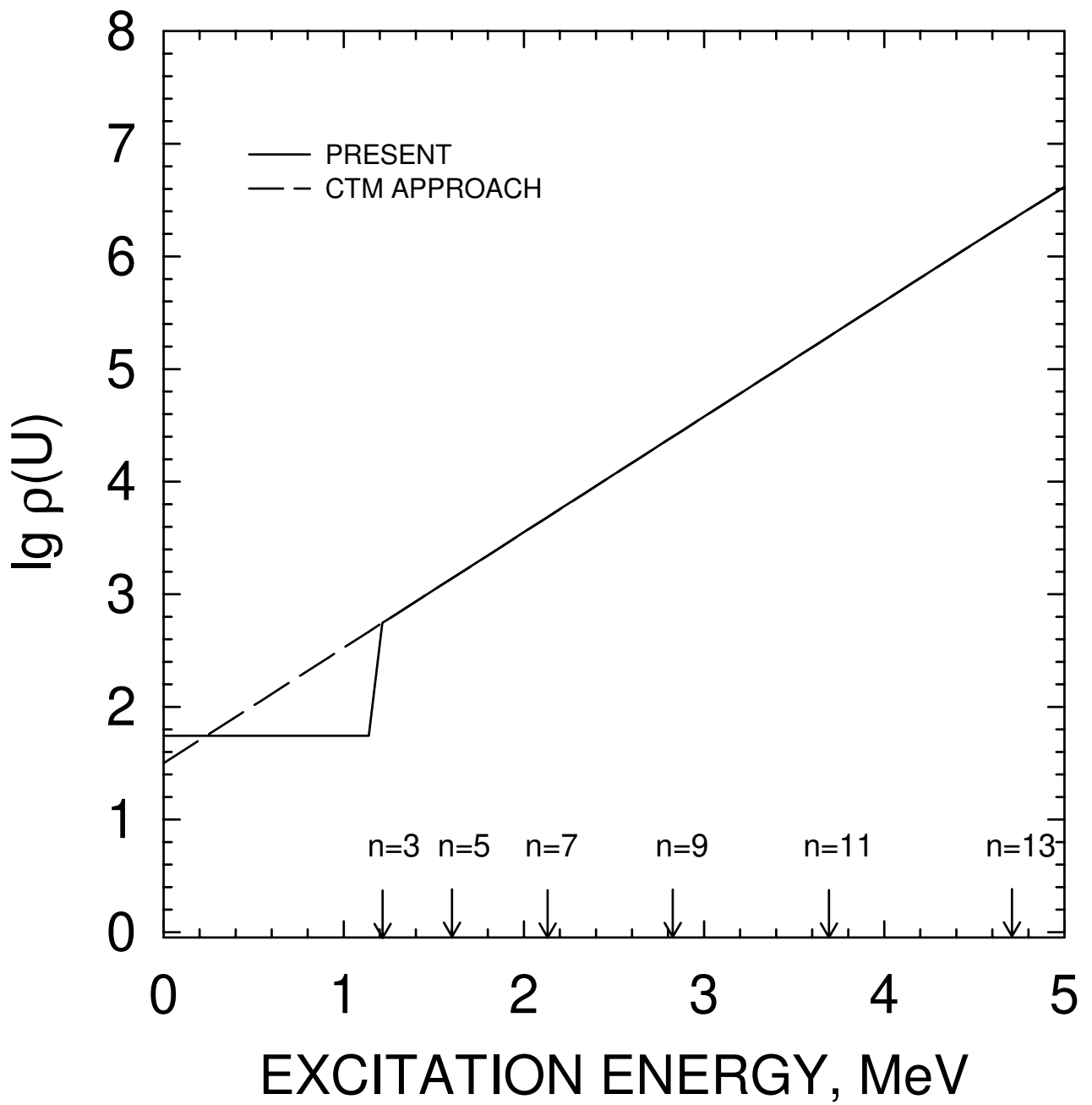


FIG. 27

^{231}Pa FISSION CROSS SECTION

CROSS SECTION, BARN

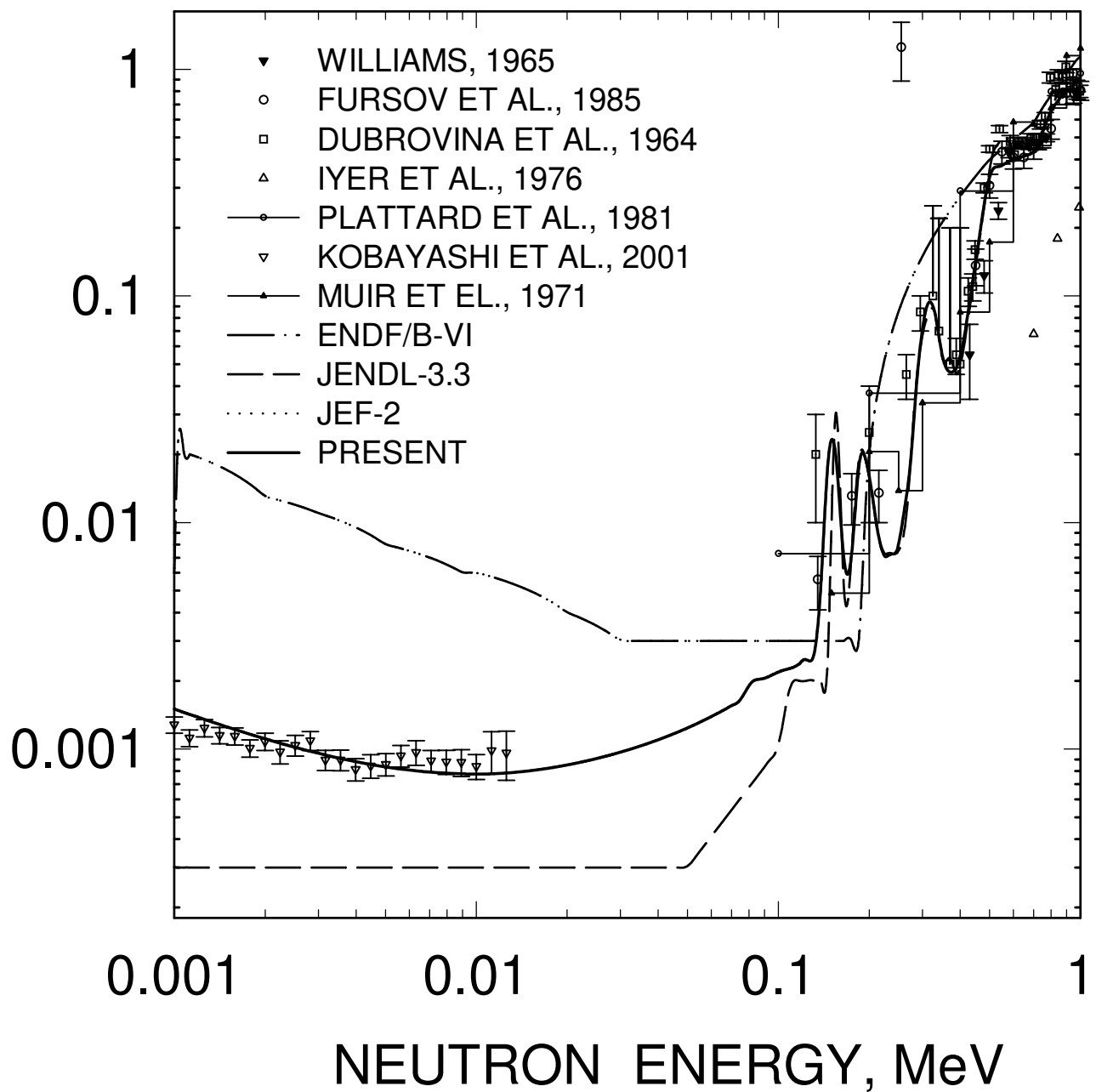


FIG. 28

^{231}Pa FISSION CROSS SECTION

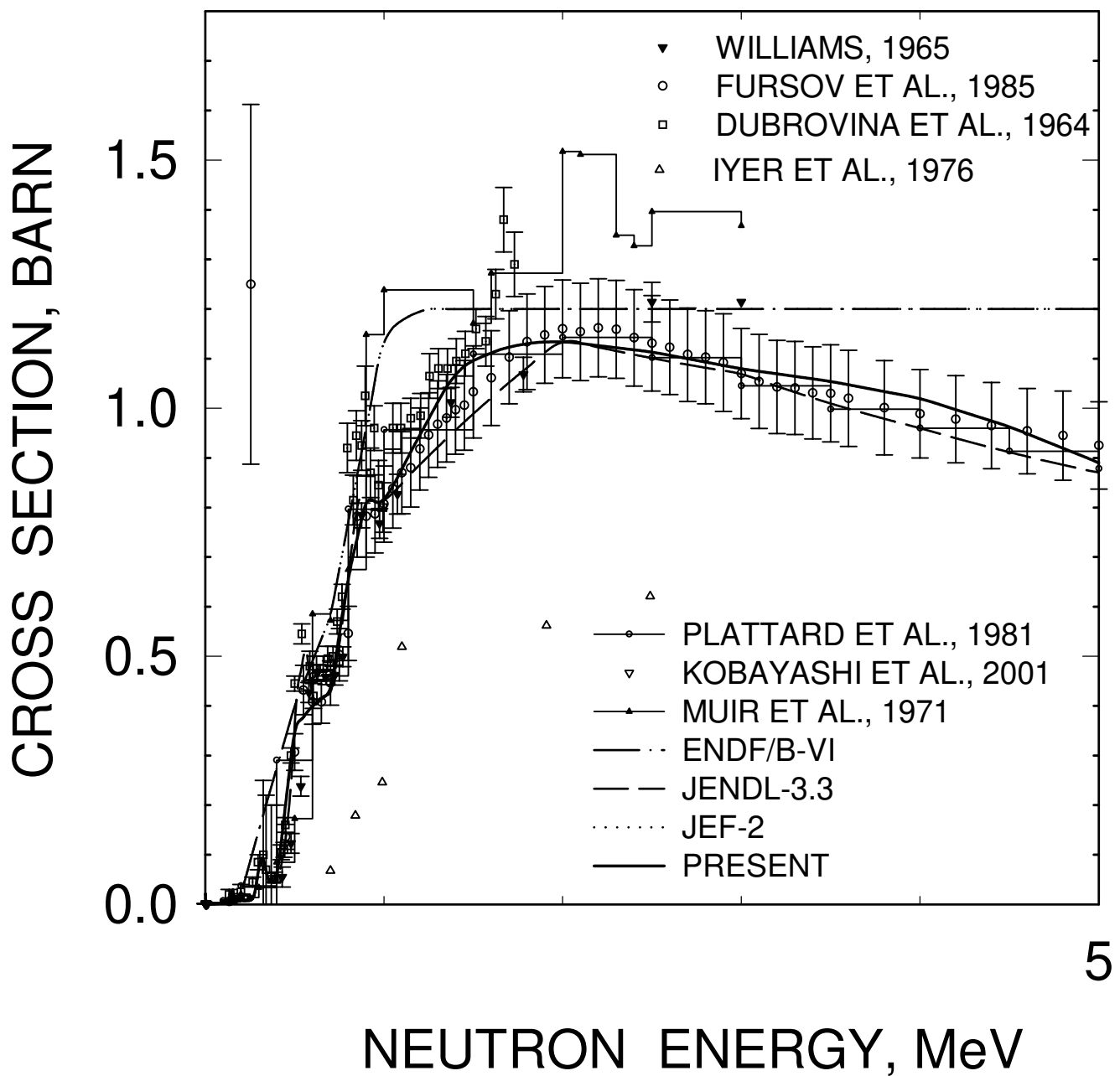


FIG. 29

^{231}Pa : 0.00921, $1/2^-$ LEVEL EXCITATION

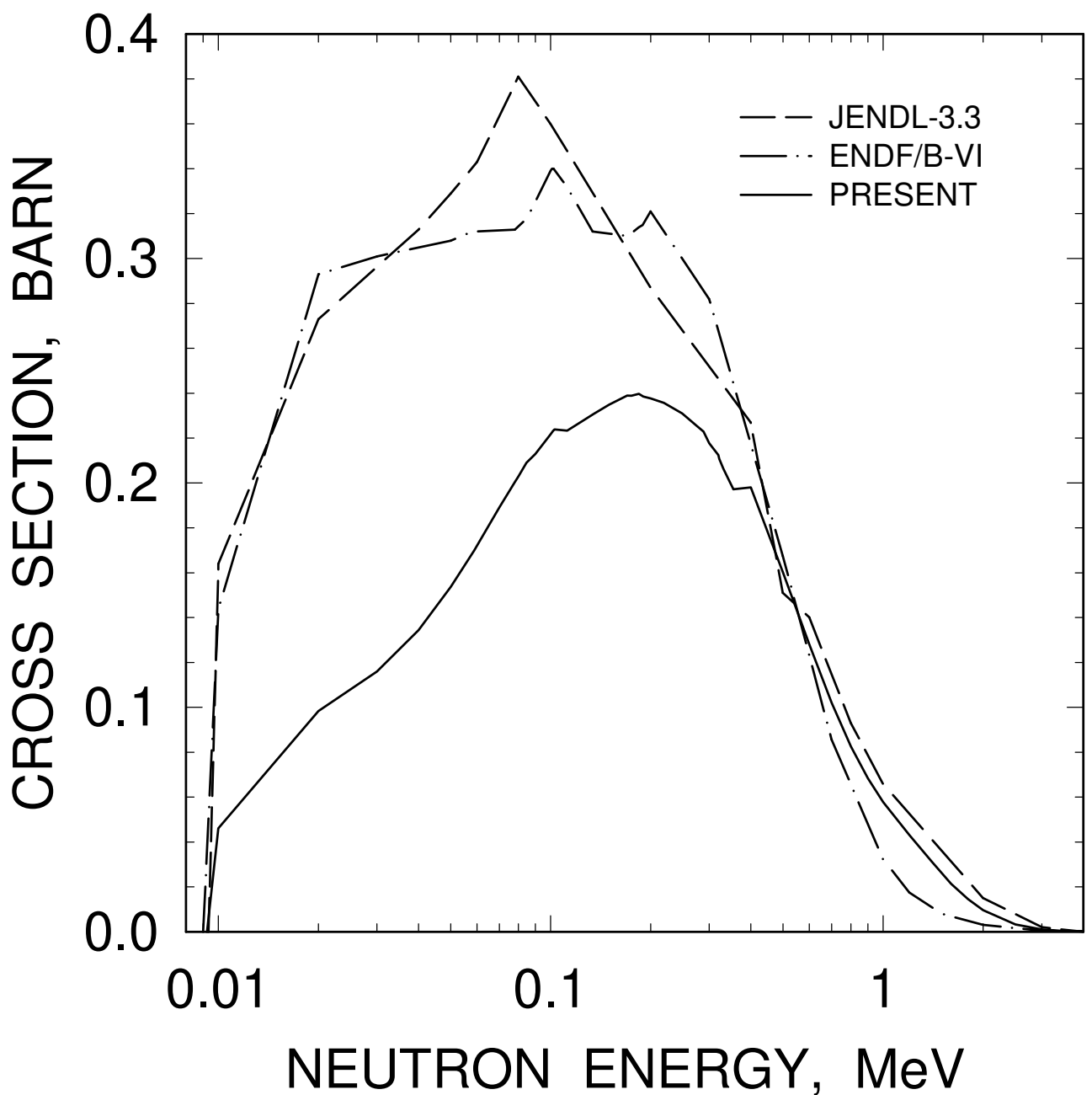


FIG. 30

^{231}Pa : 0.05857, $7/2^-$ LEVEL EXCITATION

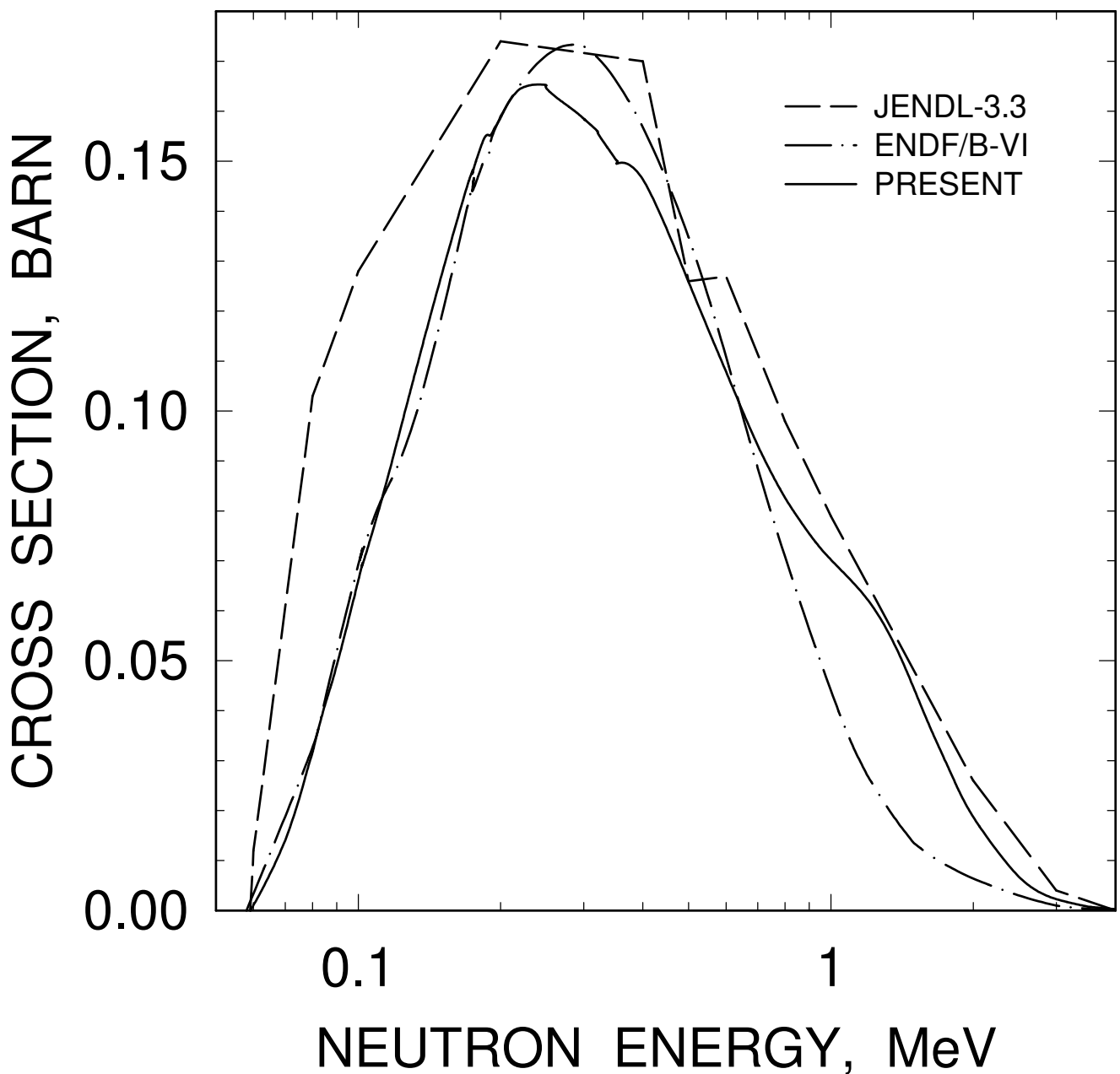


FIG. 31

^{231}Pa : 0.077685, $5/2^-$ LEVEL EXCITATION

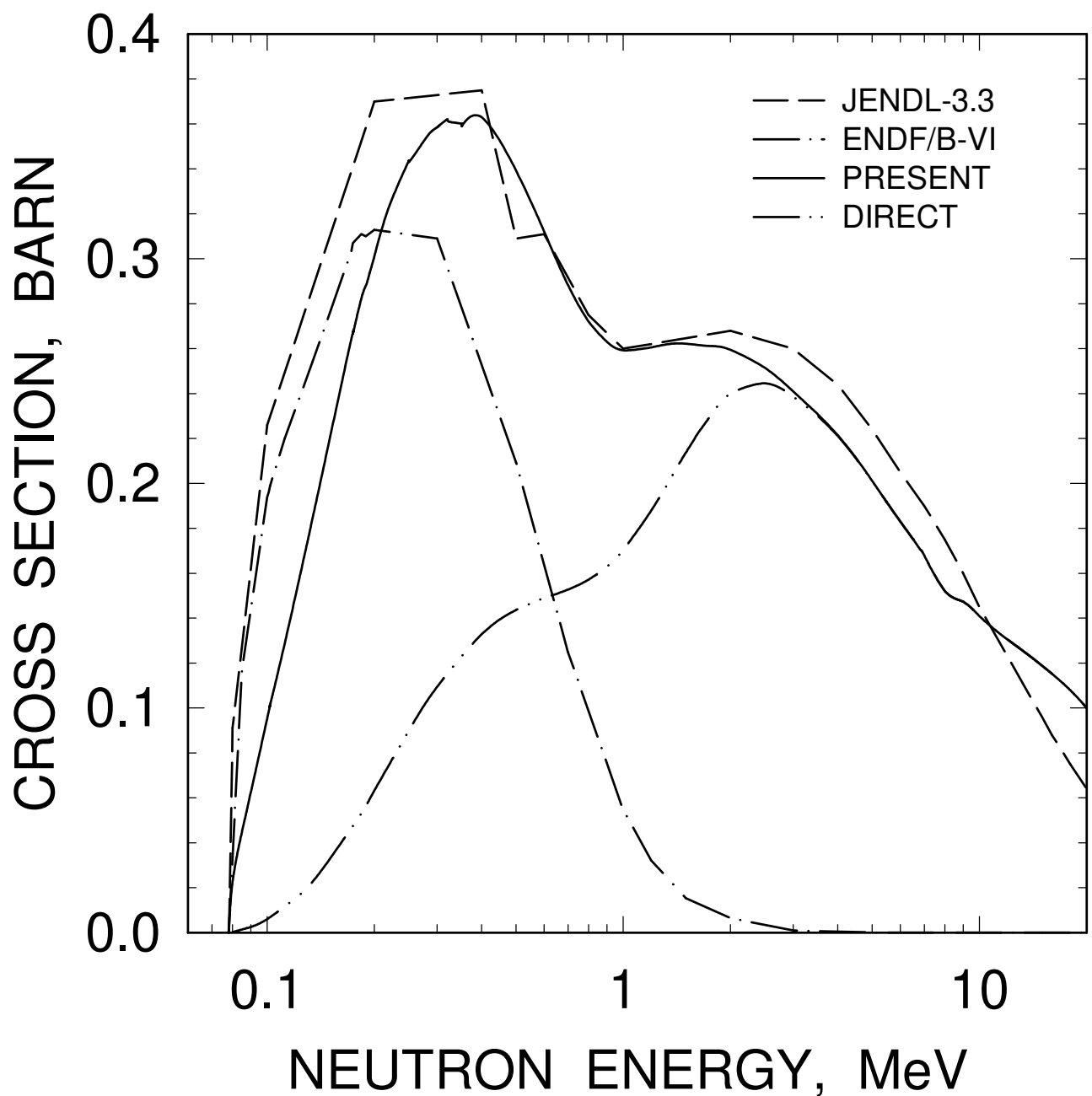


FIG. 32

^{231}Pa : 0.084216, $5/2^+$ LEVEL EXCITATION

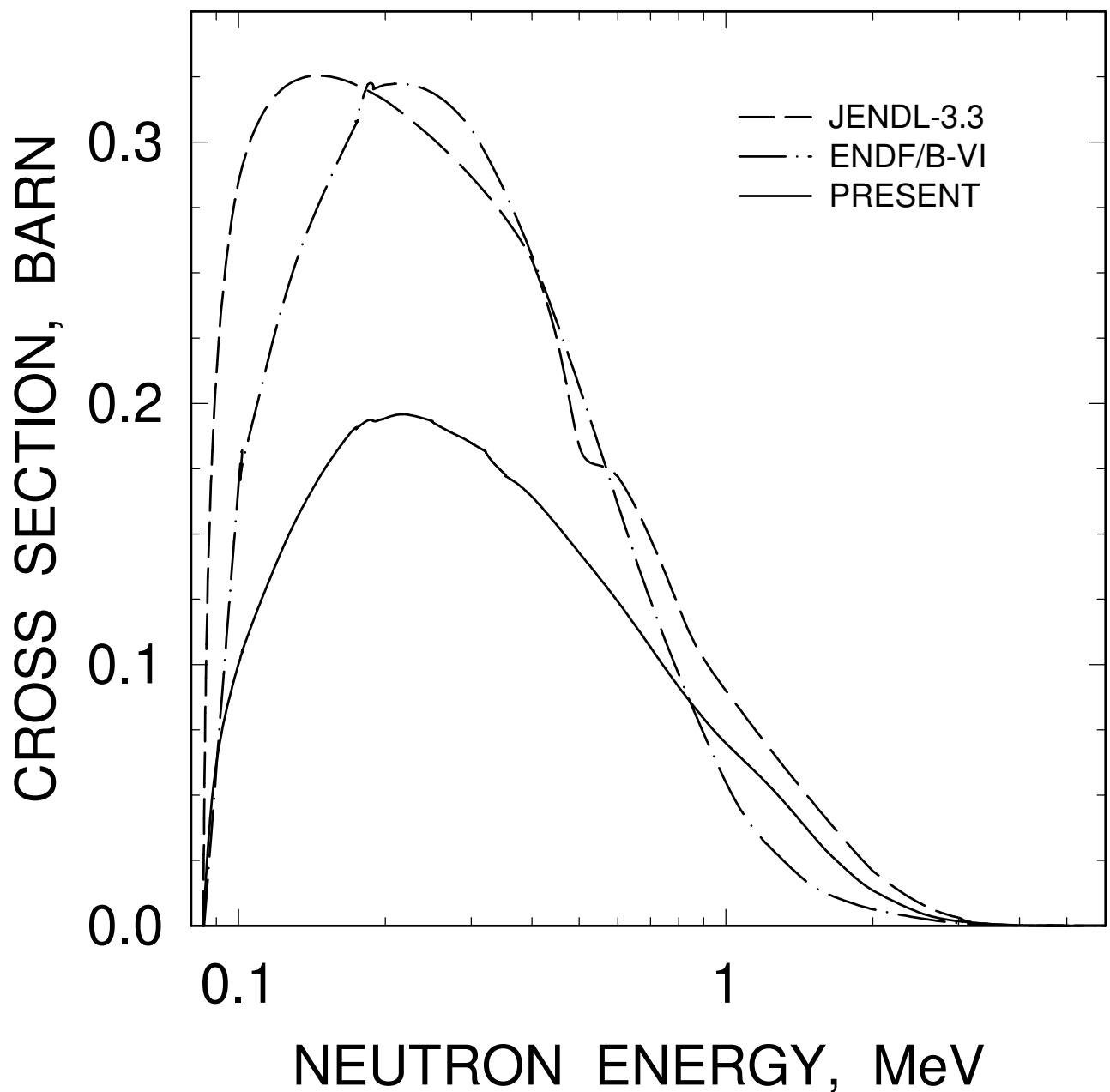


FIG. 33

^{231}Pa : 0.101408, $7/2^+$ LEVEL EXCITATION

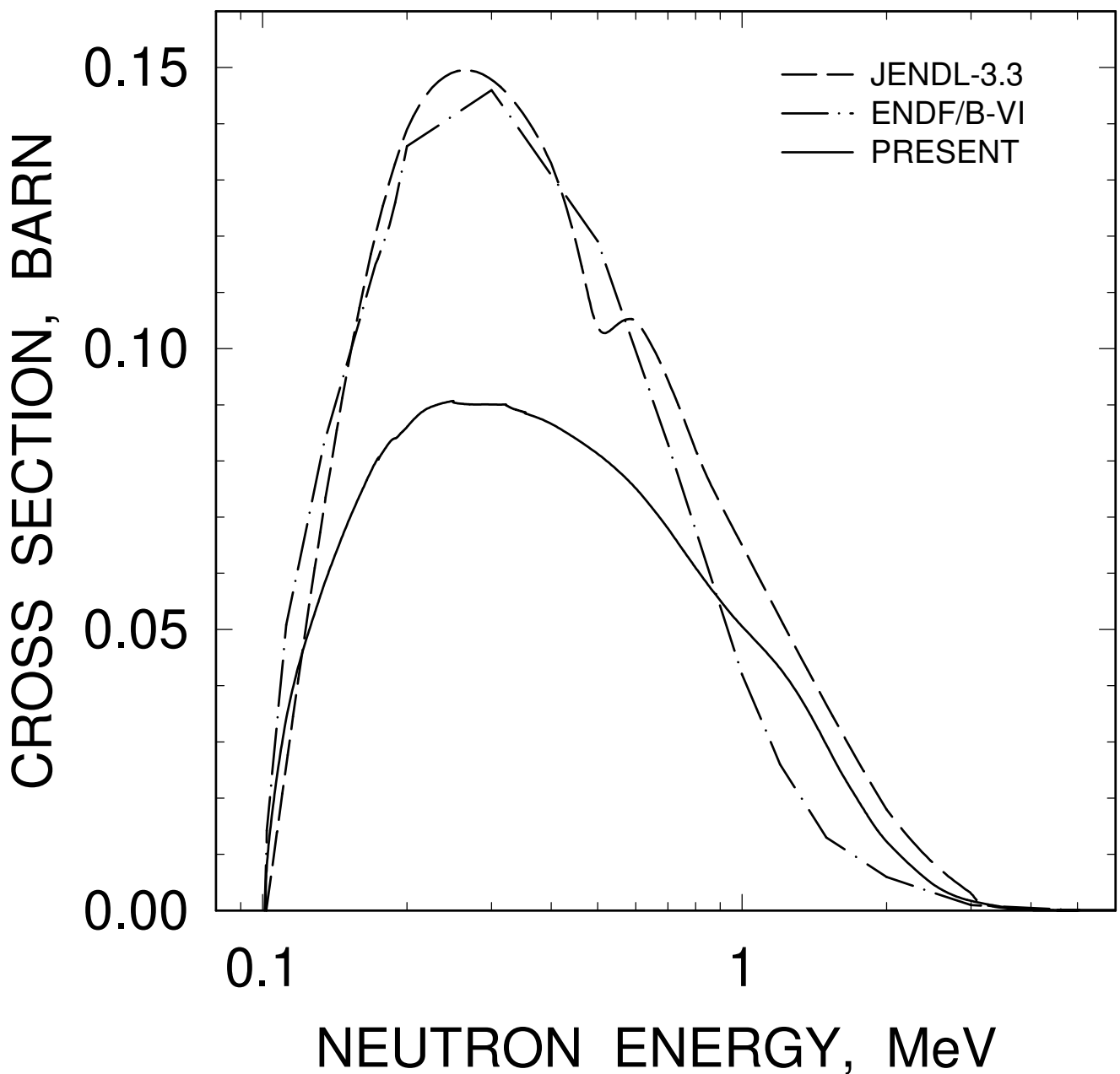


FIG. 34

^{231}Pa : 0.102268, $3/2^+$ LEVEL EXCITATION

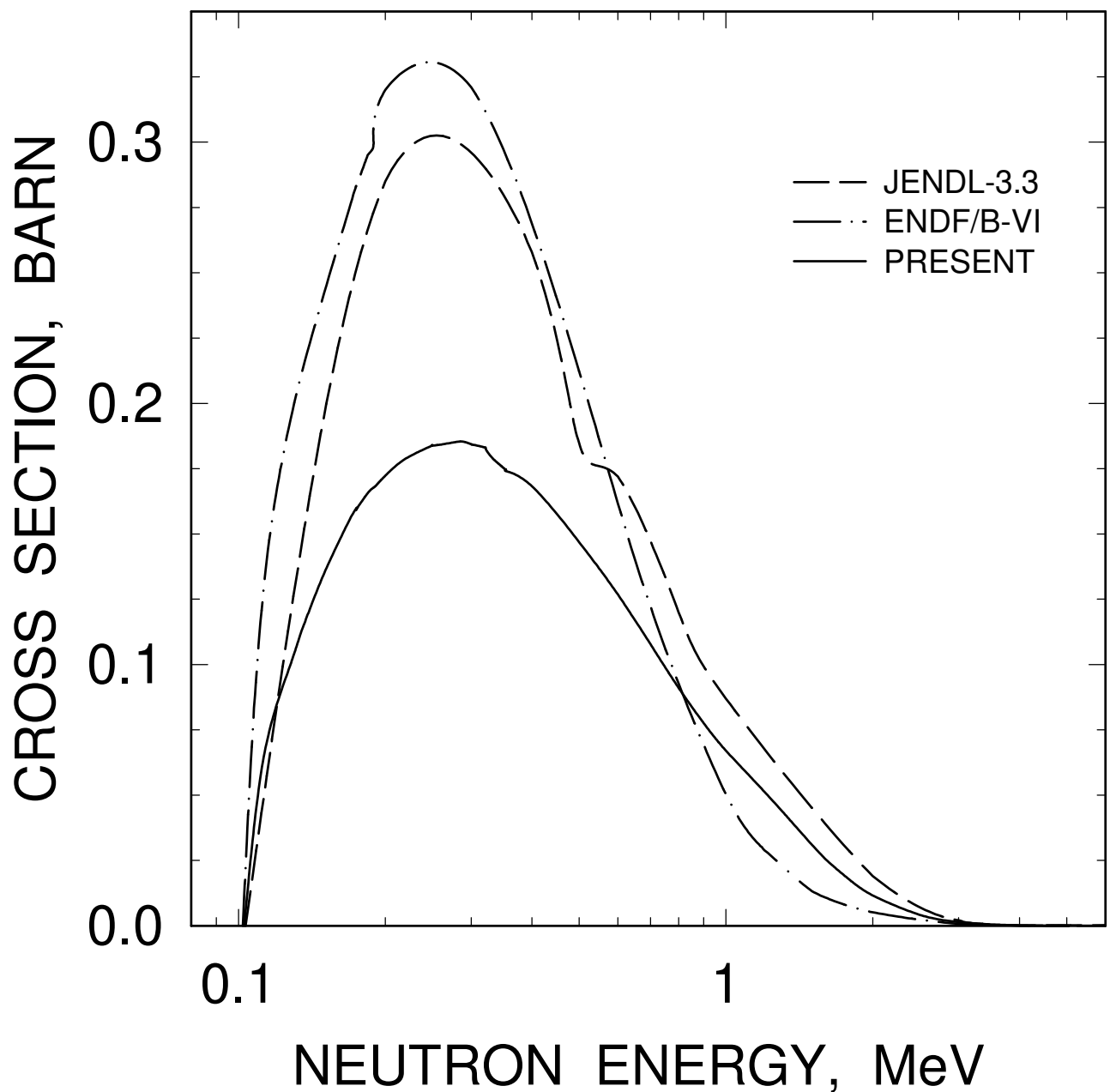


FIG. 35

^{231}Pa : 0.111653, ($9/2^+$) LEVEL EXCITATION

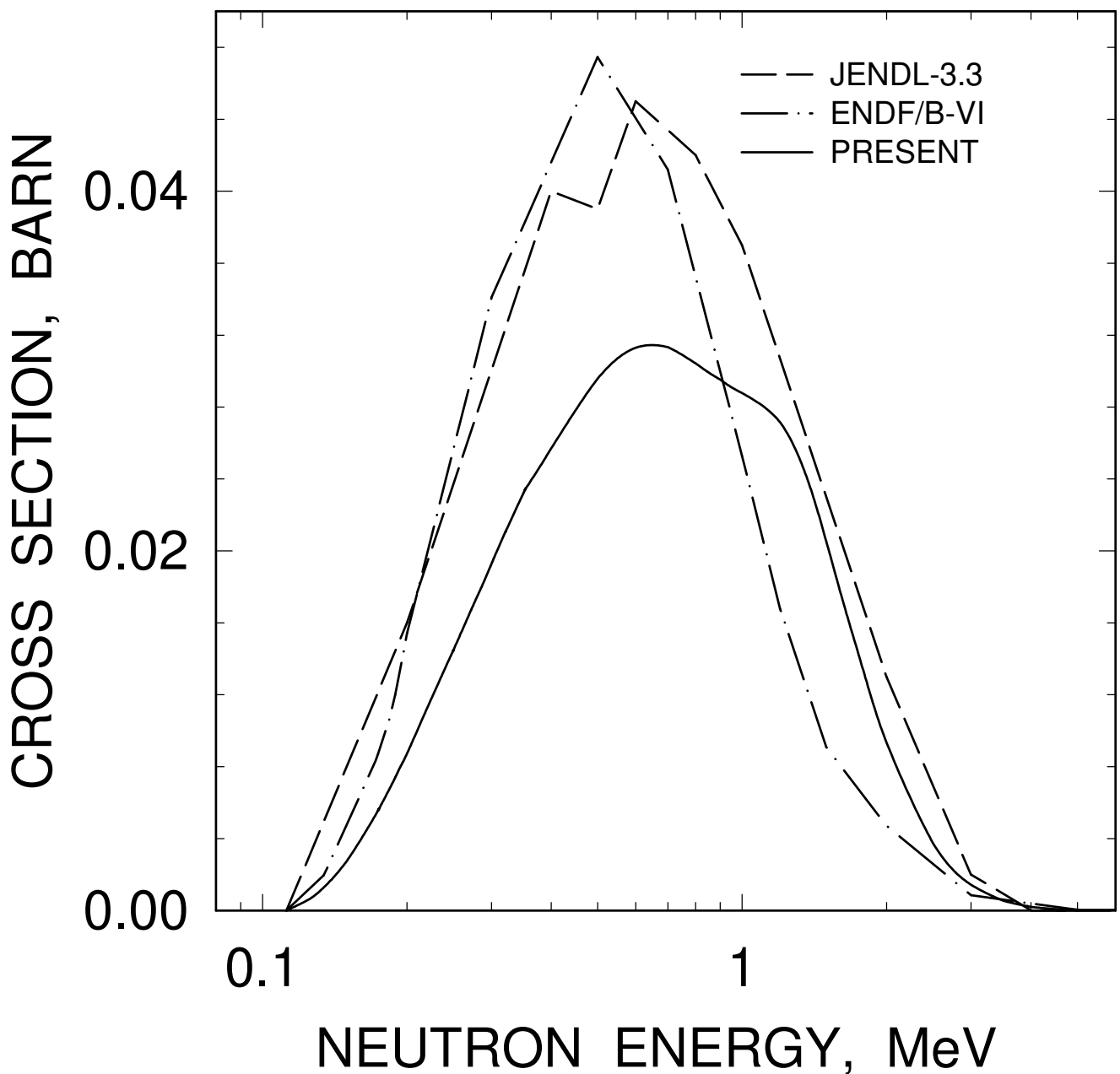


FIG. 36

^{231}Pa : 0.134, ($11/2^+$) LEVEL EXCITATION

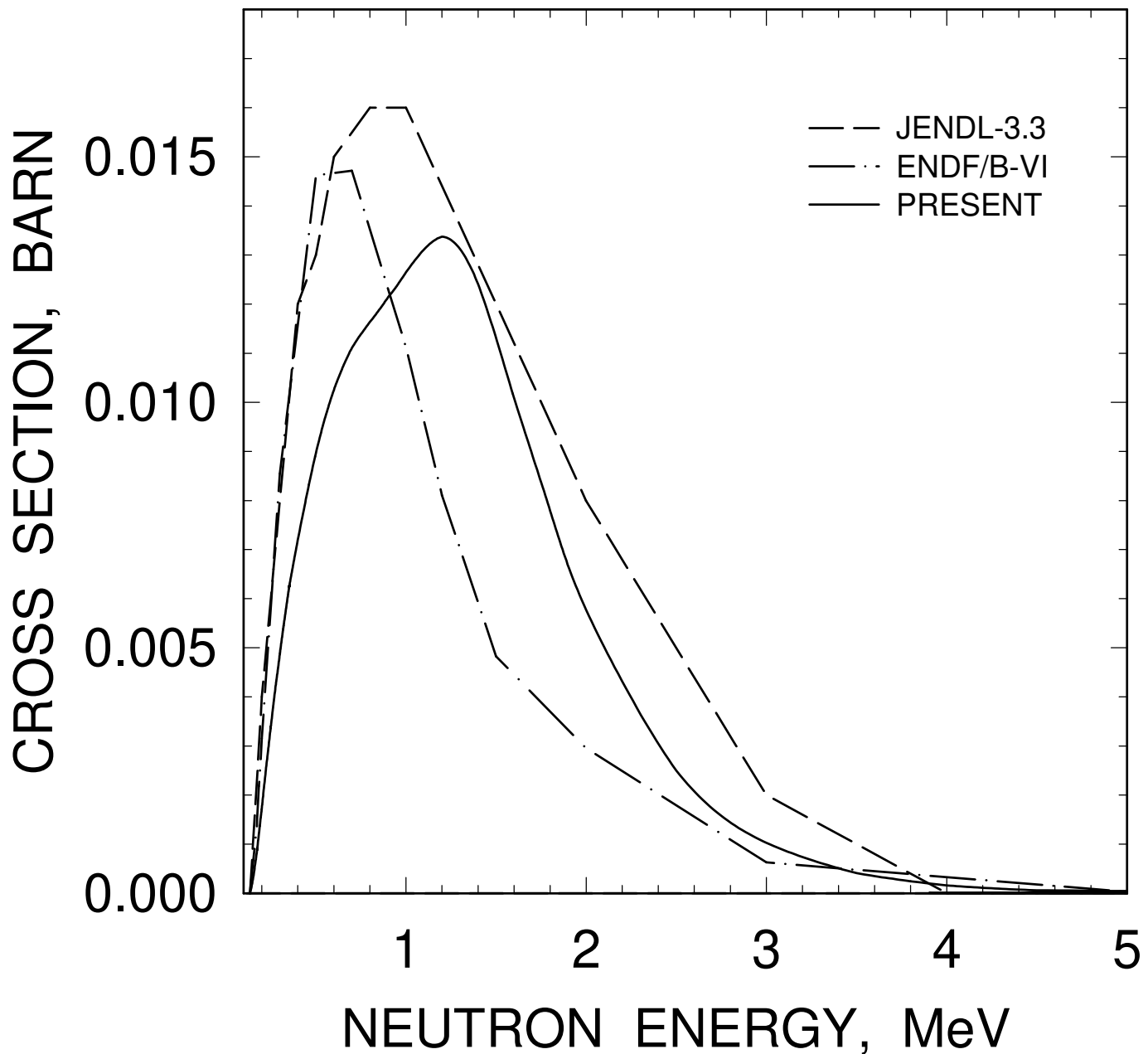


FIG. 37

^{231}Pa : 0.169, $11/2^-$ LEVEL EXCITATION

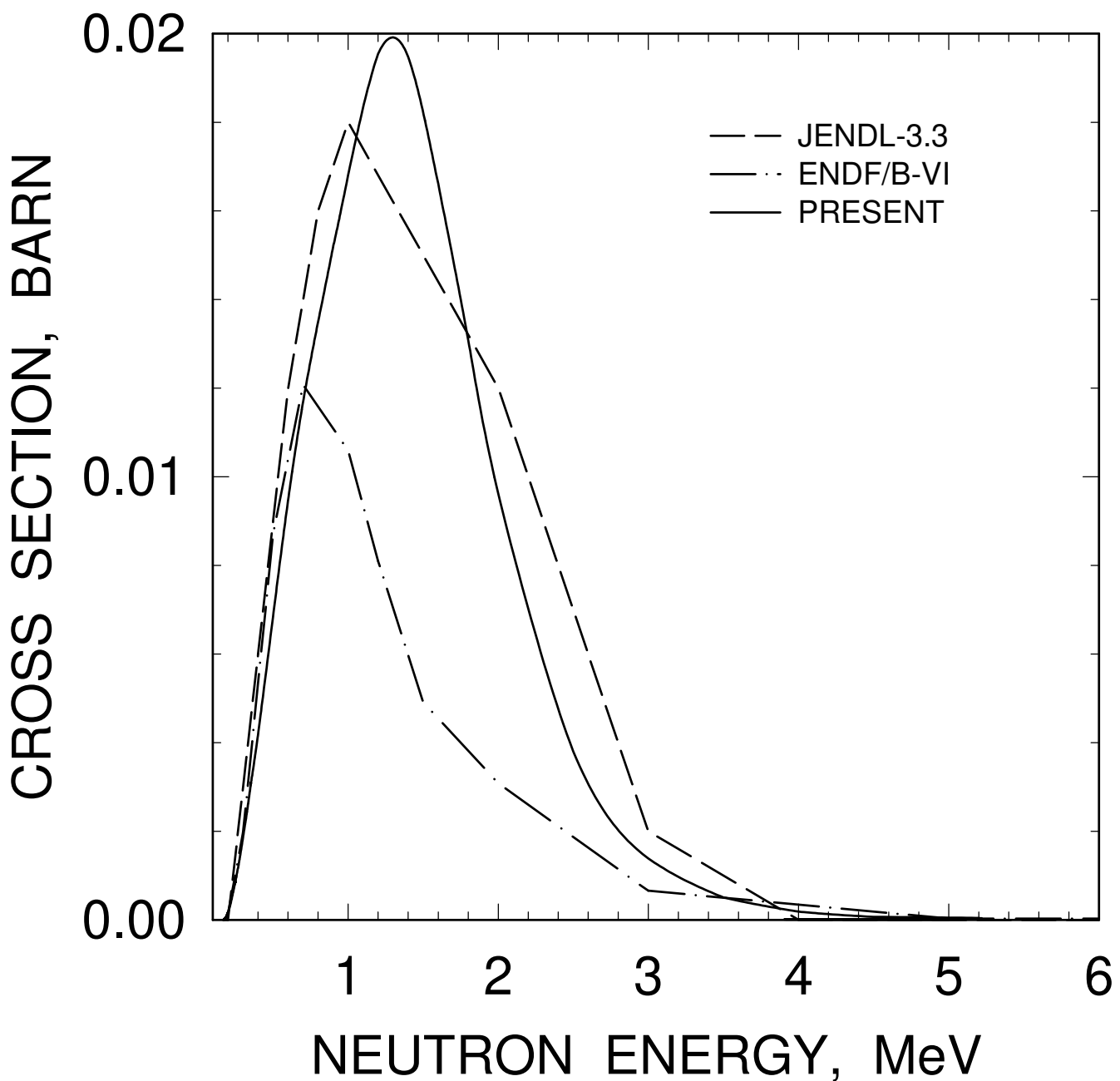


FIG. 38

^{231}Pa : 0.17416, ($5/2^-$) LEVEL EXCITATION

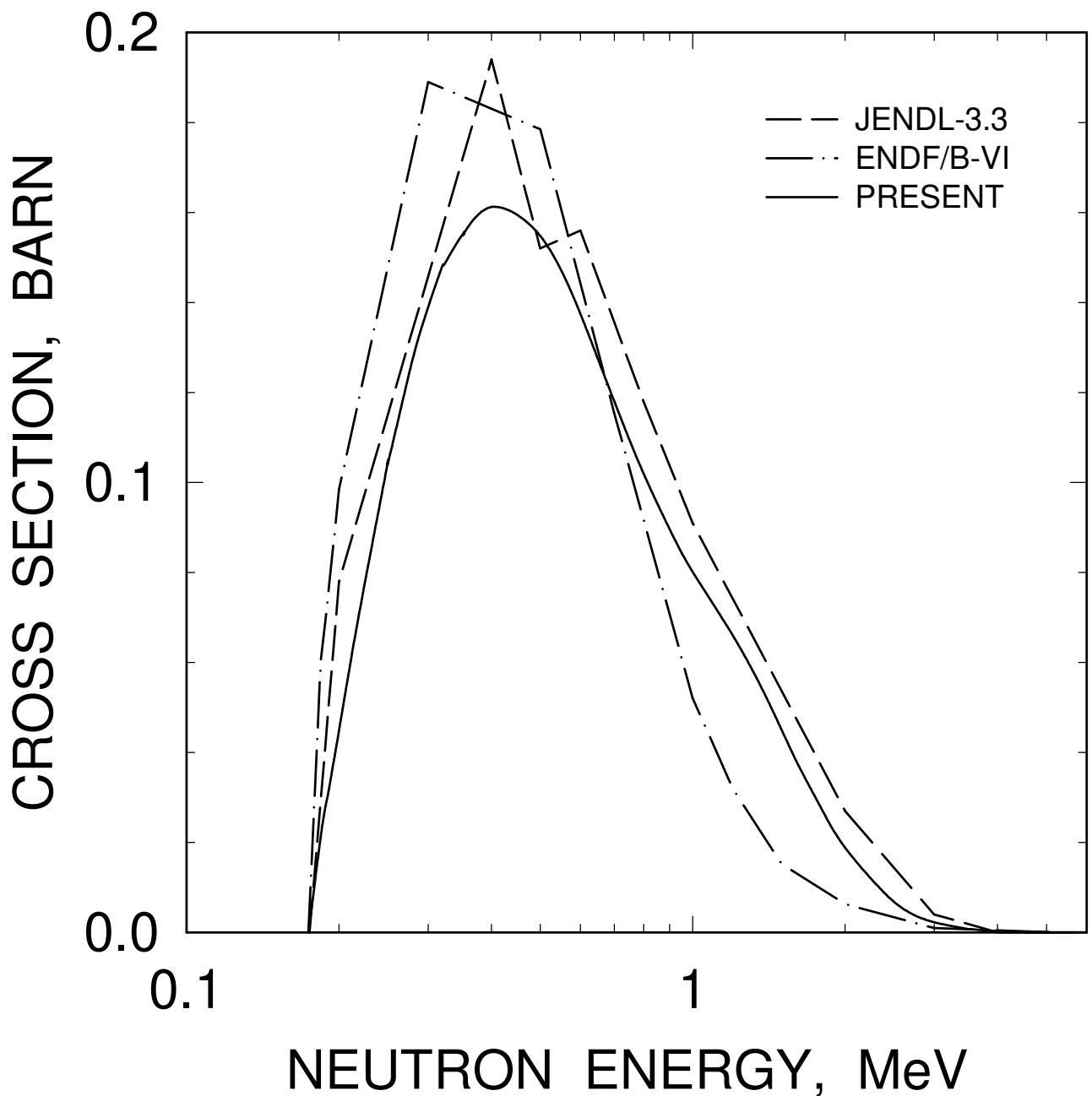


FIG. 39

^{231}Pa : 0.183495, $5/2^+$ LEVEL EXCITATION

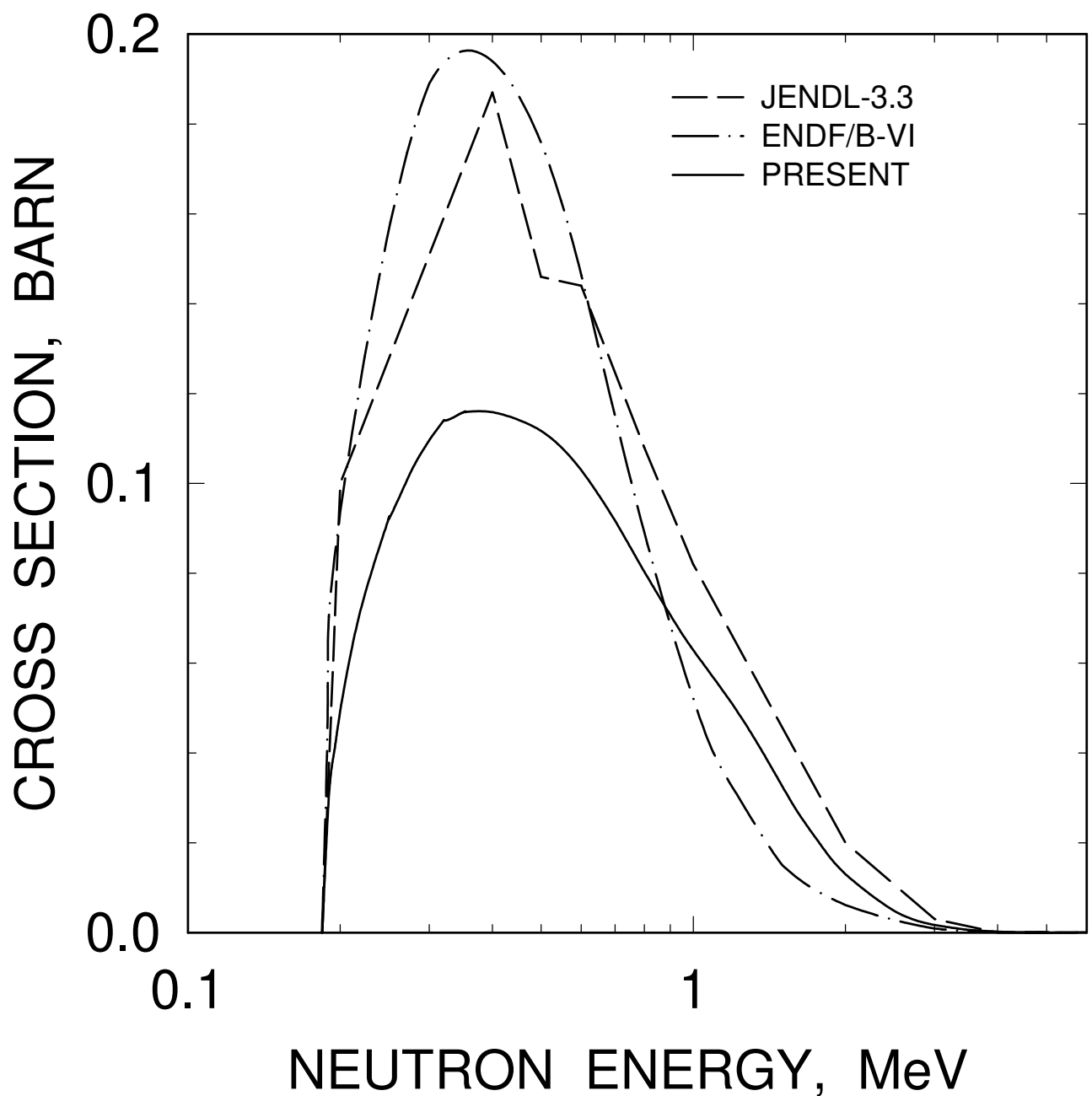


FIG. 40

^{231}Pa : 0.189, $13/2^+$ LEVEL EXCITATION

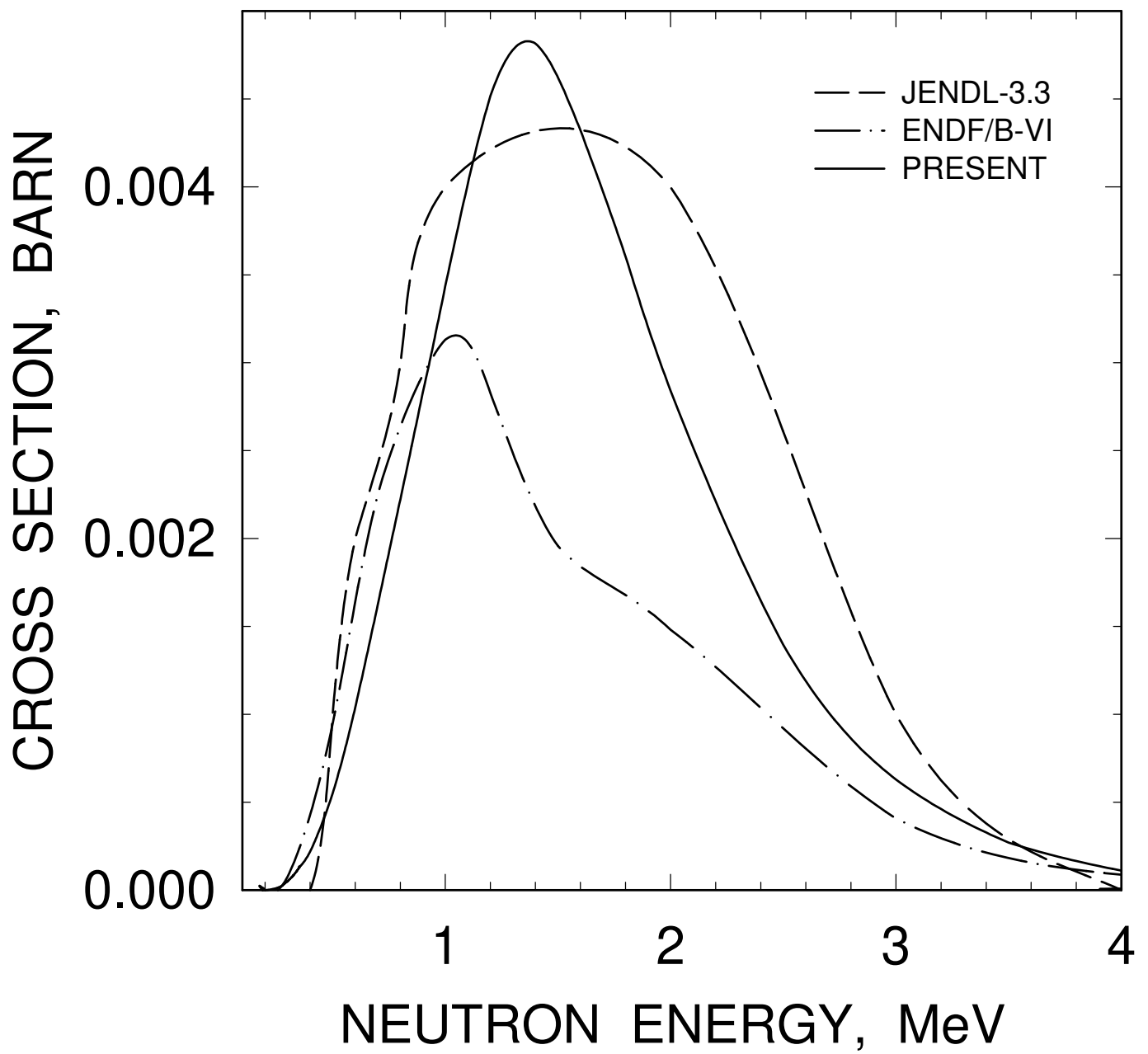


FIG. 41

^{231}Pa : 0.21824, ($7/2^-$) LEVEL EXCITATION

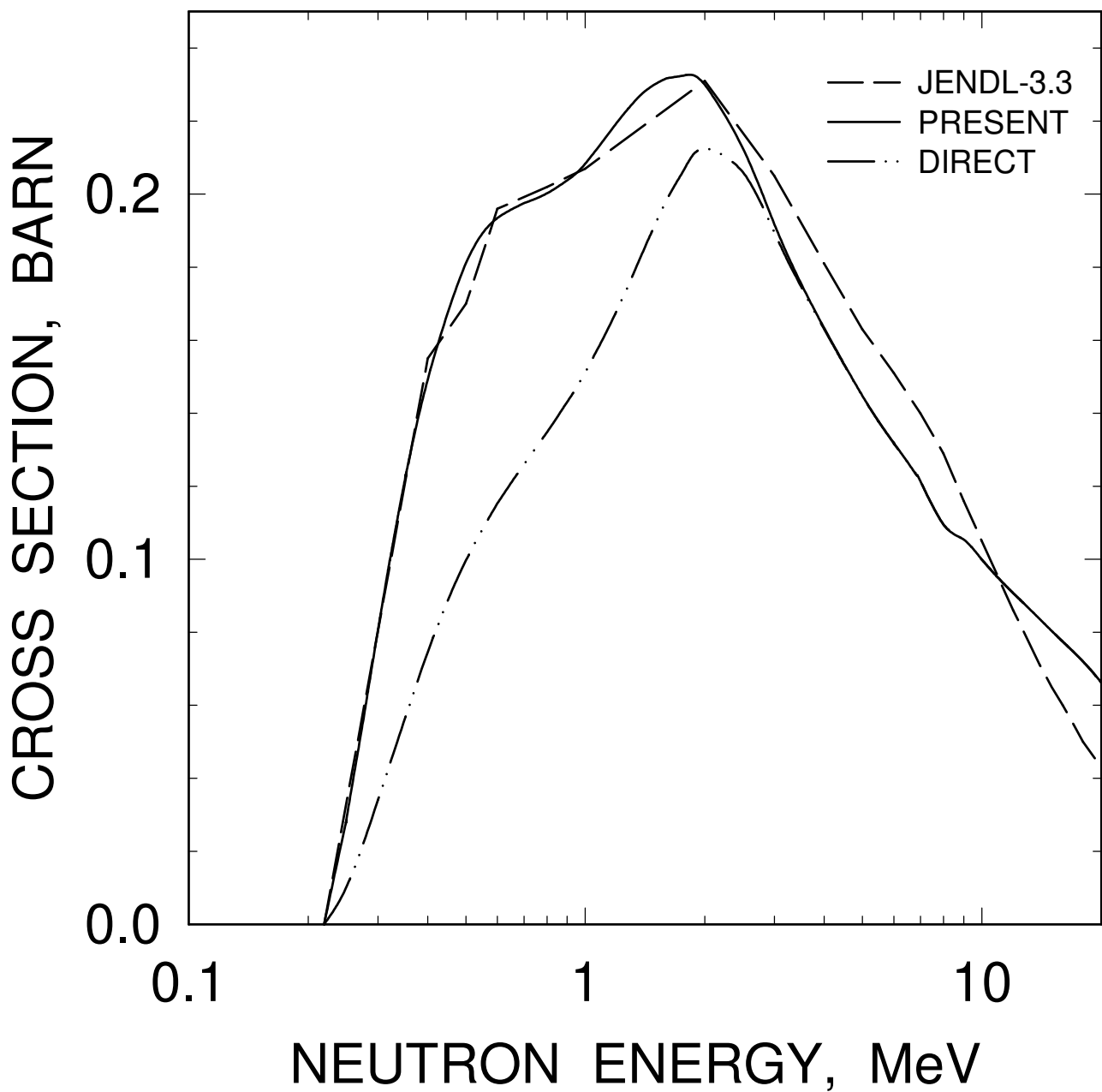


FIG. 42

^{231}Pa : 0.24732, $7/2^+$ LEVEL EXCITATION

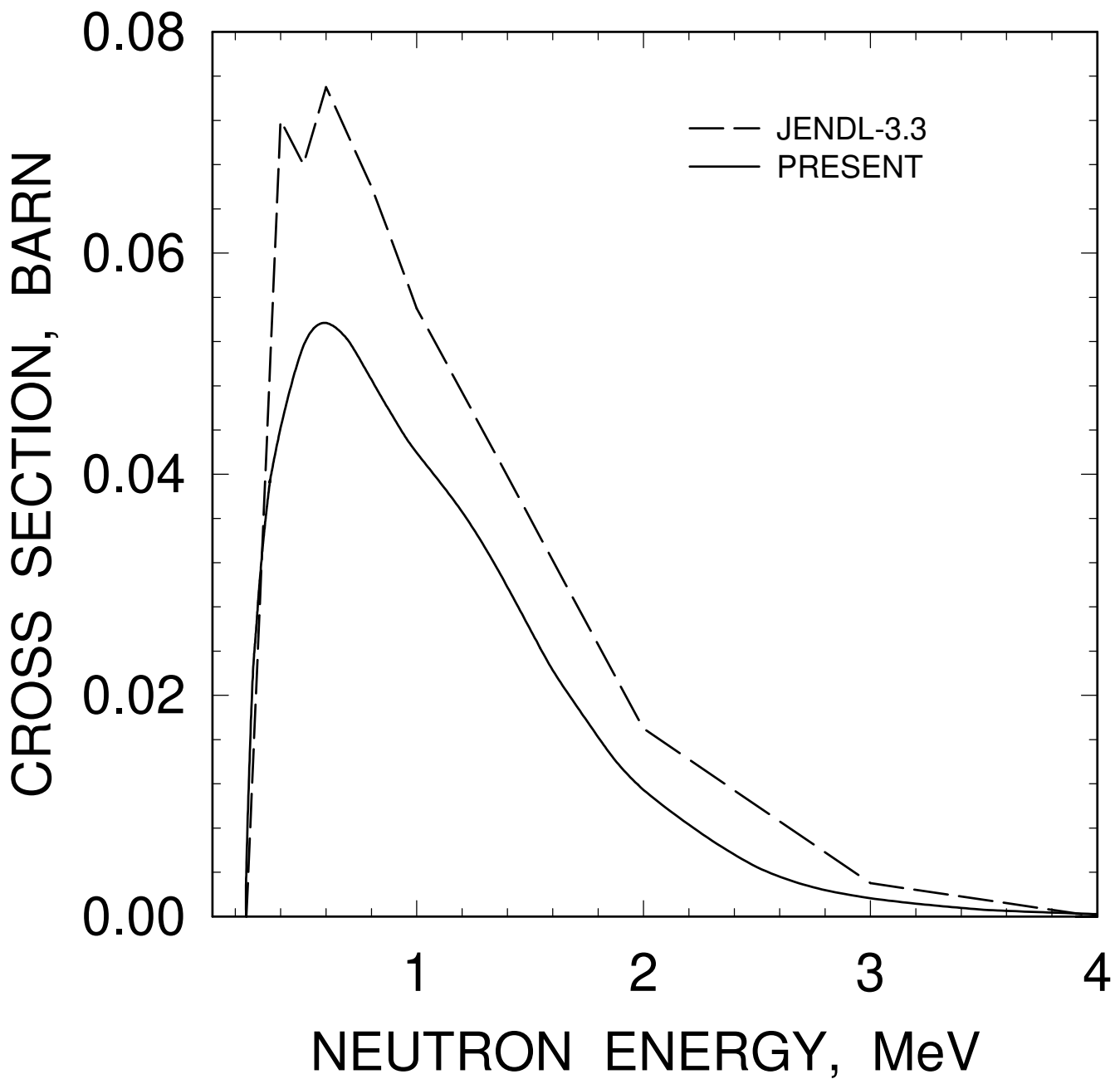


FIG. 43

^{231}Pa : 0.272, (9/2 $^{-}$) LEVEL EXCITATION

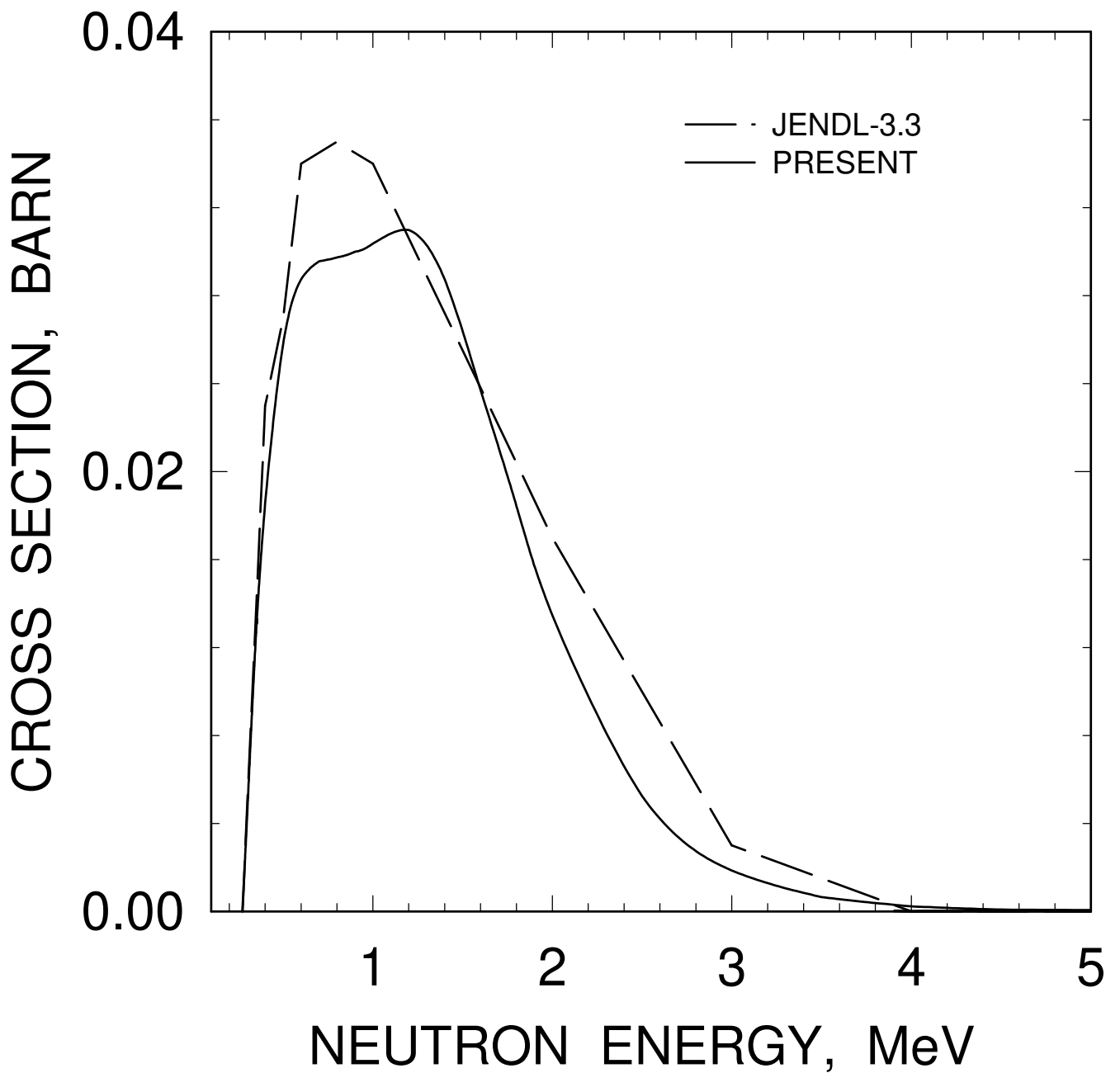


FIG. 44

^{231}Pa : 0.287, ($1/2^+$) LEVEL EXCITATION

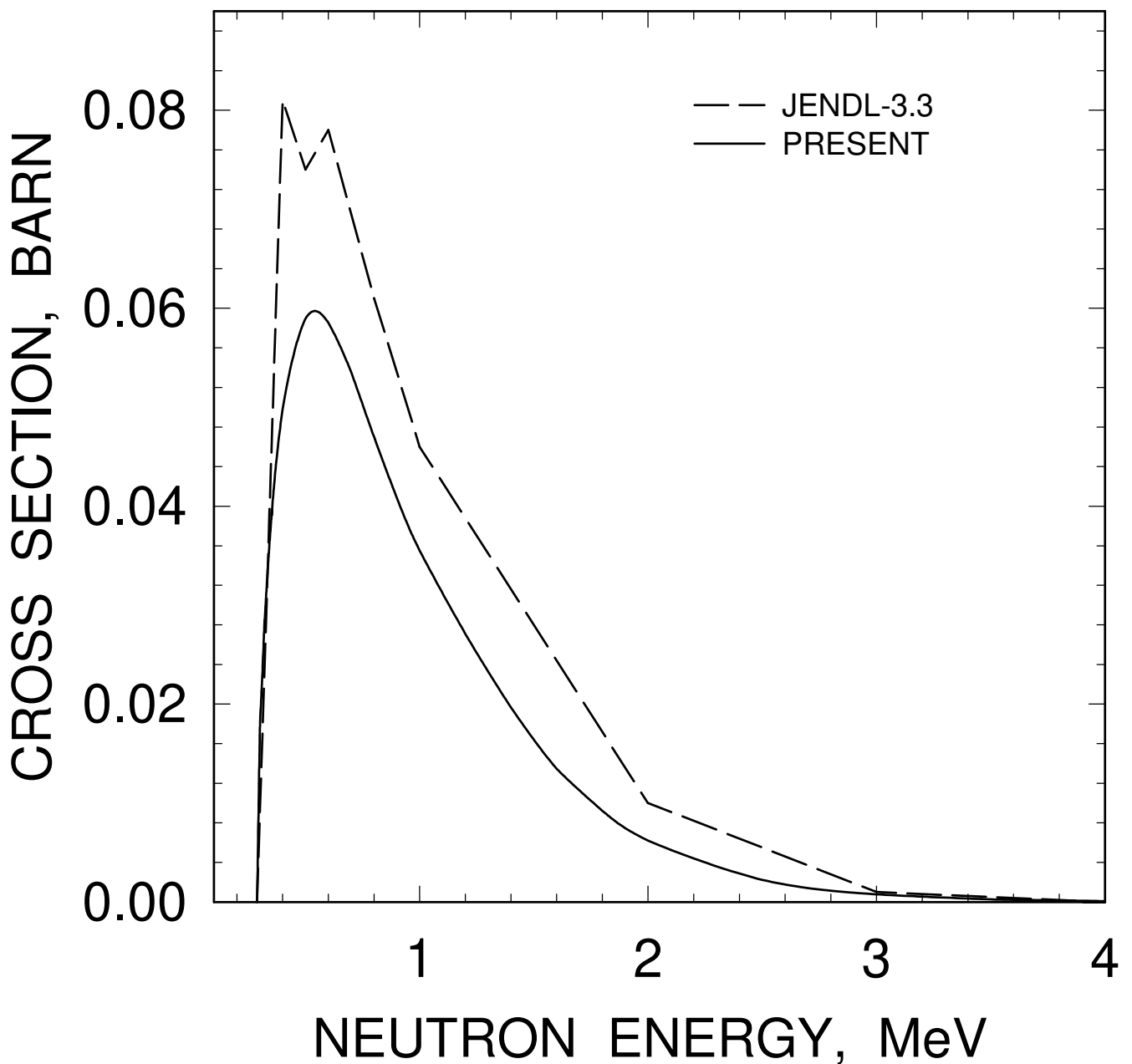


FIG. 45

^{231}Pa : 0.31795, ($3/2^+$) LEVEL EXCITATION

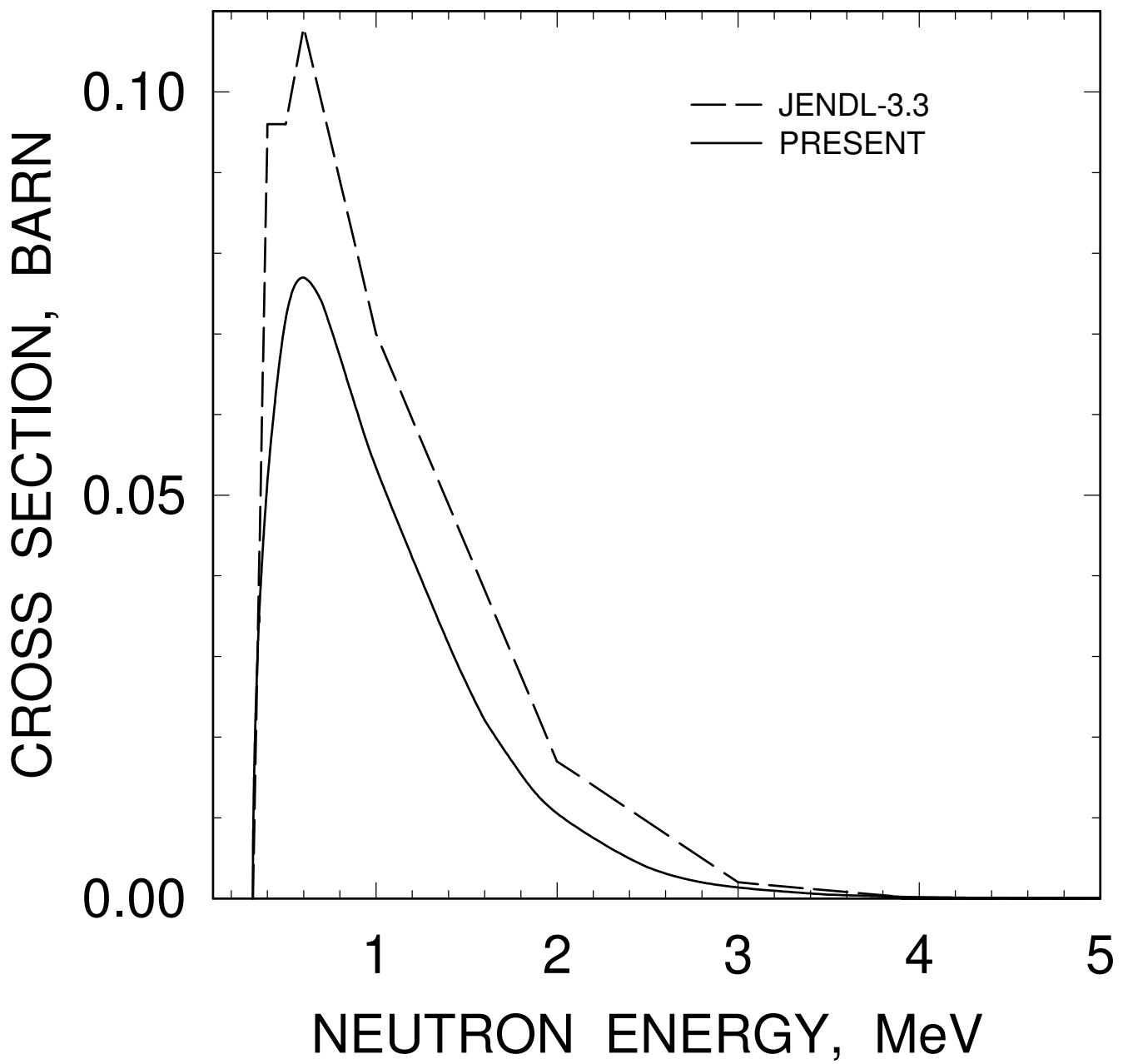


FIG. 46

^{231}Pa : 0.320209, $3/2^-$ LEVEL EXCITATION

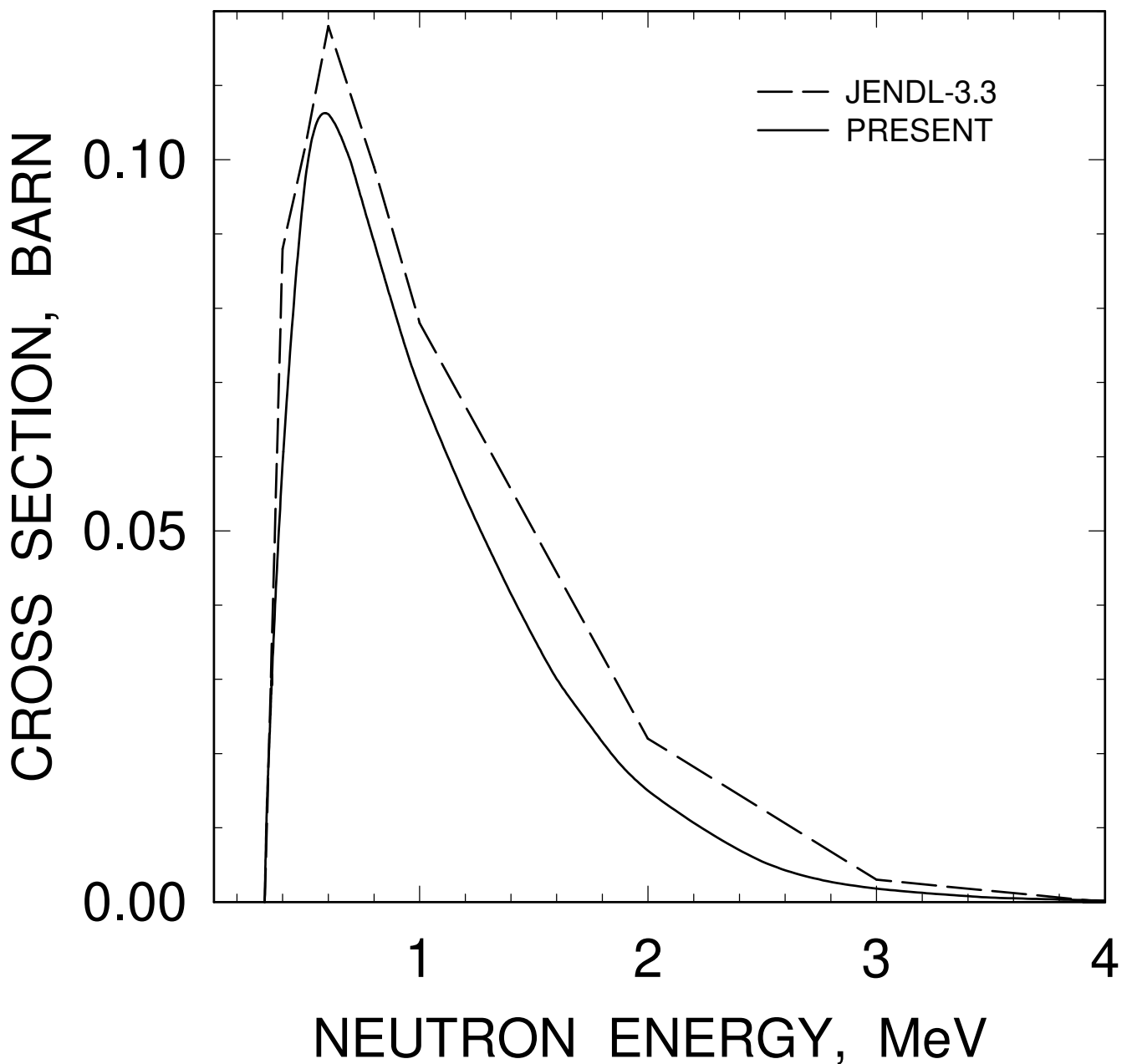


FIG. 47

^{231}Pa : 0.340, (11/2 $^{-}$) LEVEL EXCITATION

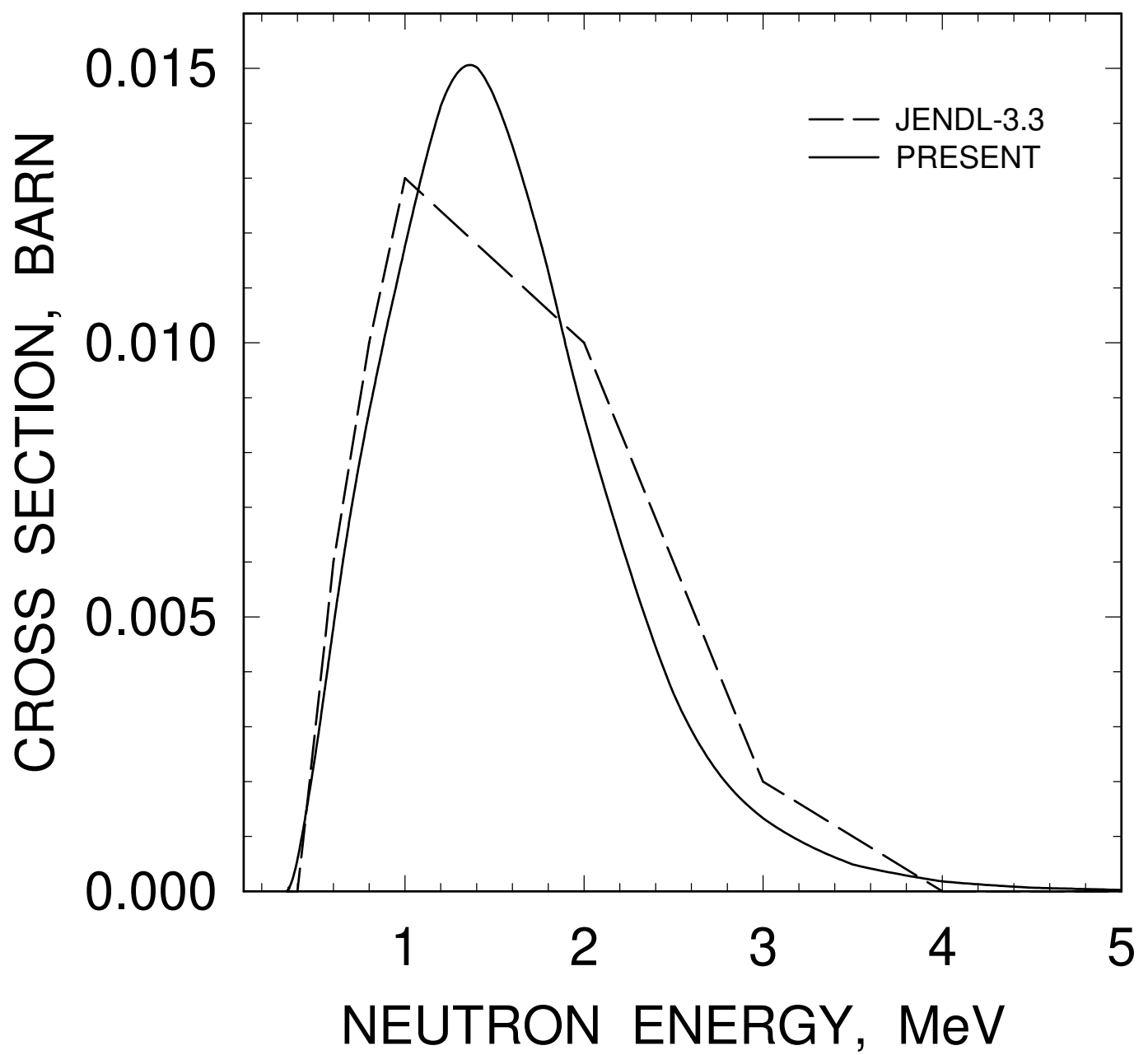


FIG. 48

^{231}Pa : 0.35184, $(5/2^-)$ LEVEL EXCITATION

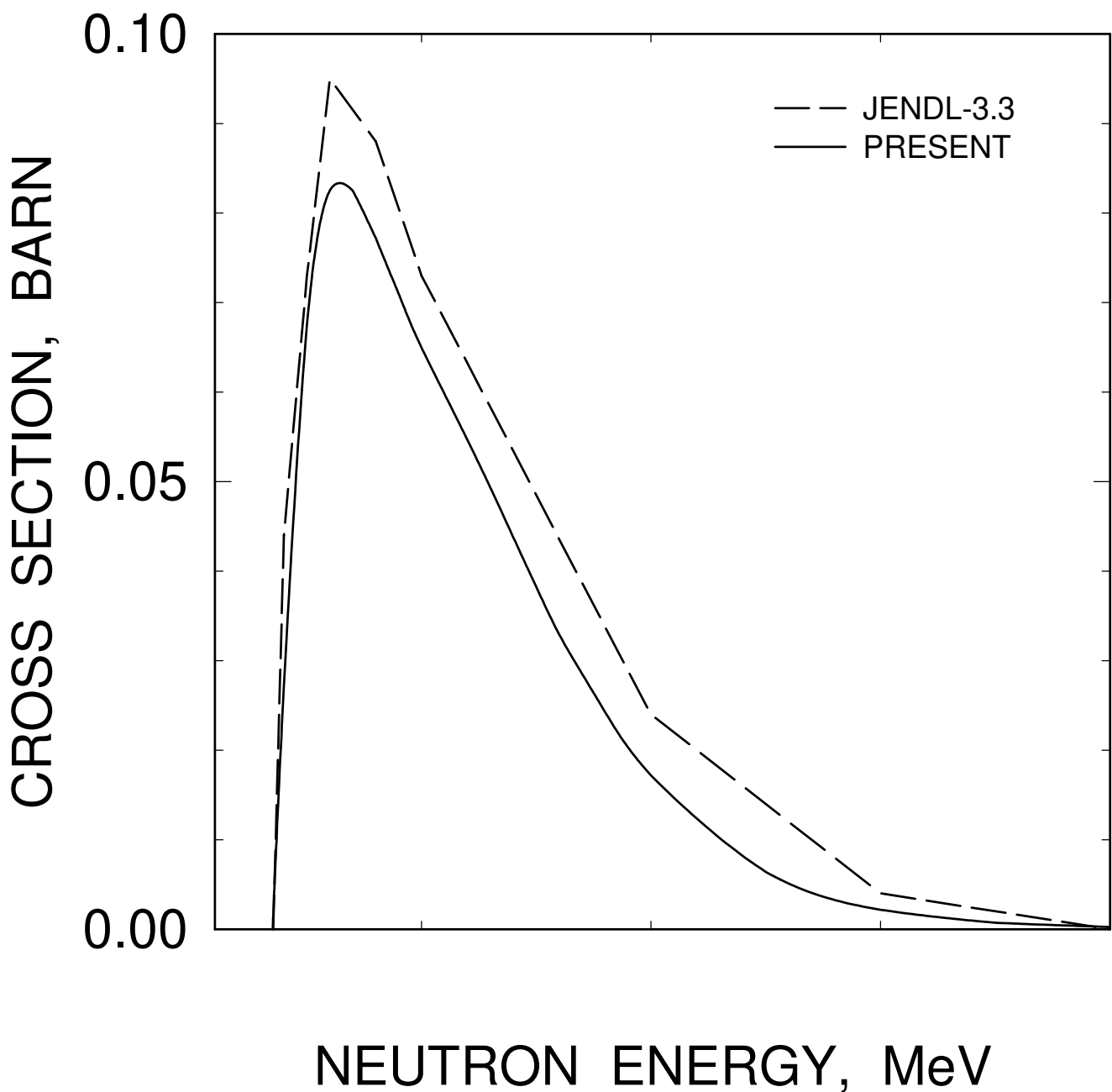


FIG. 49

^{231}Pa INELASTIC CROSS SECTION

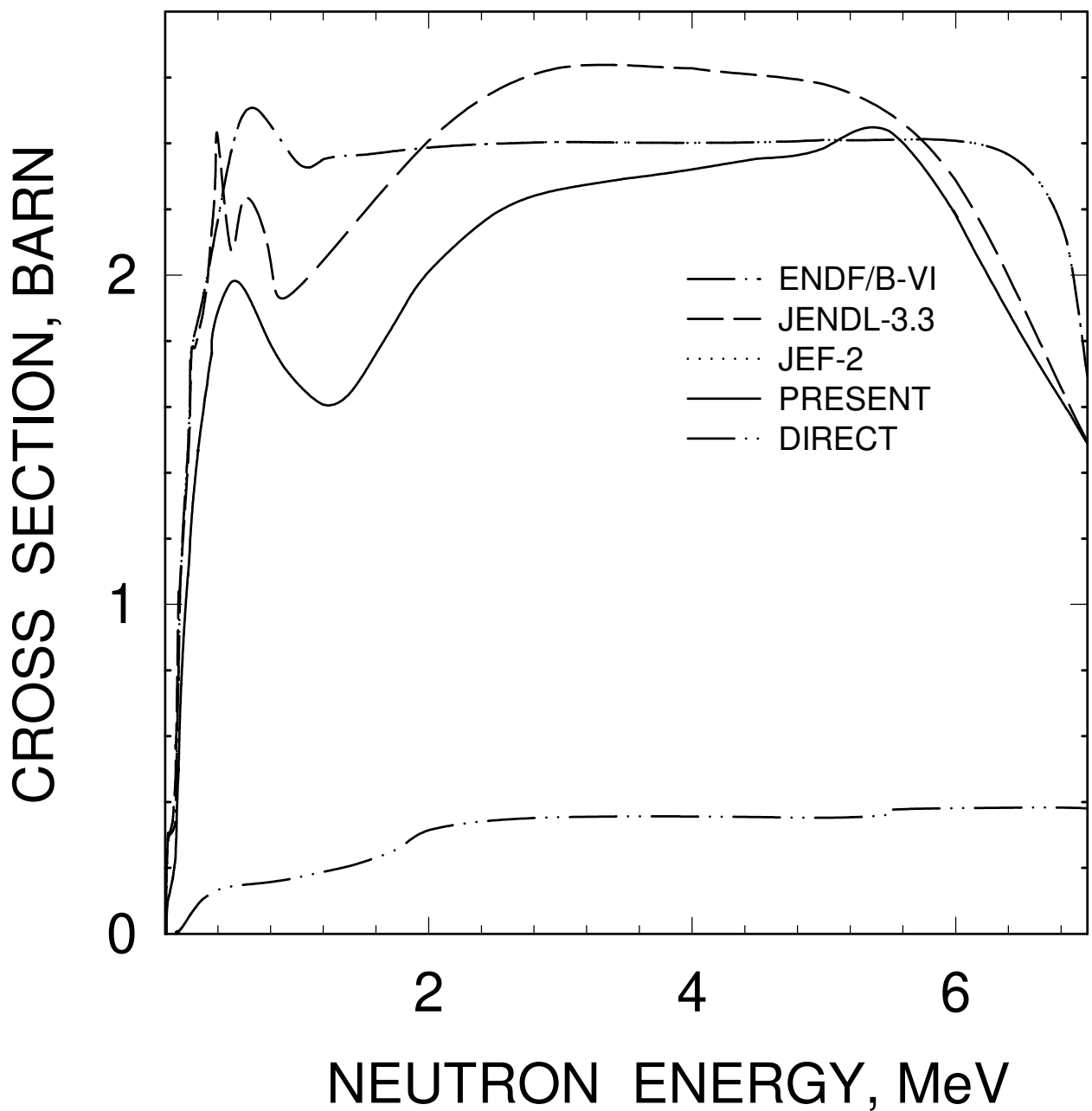


FIG. 50

^{231}Pa INELASTIC CROSS SECTION

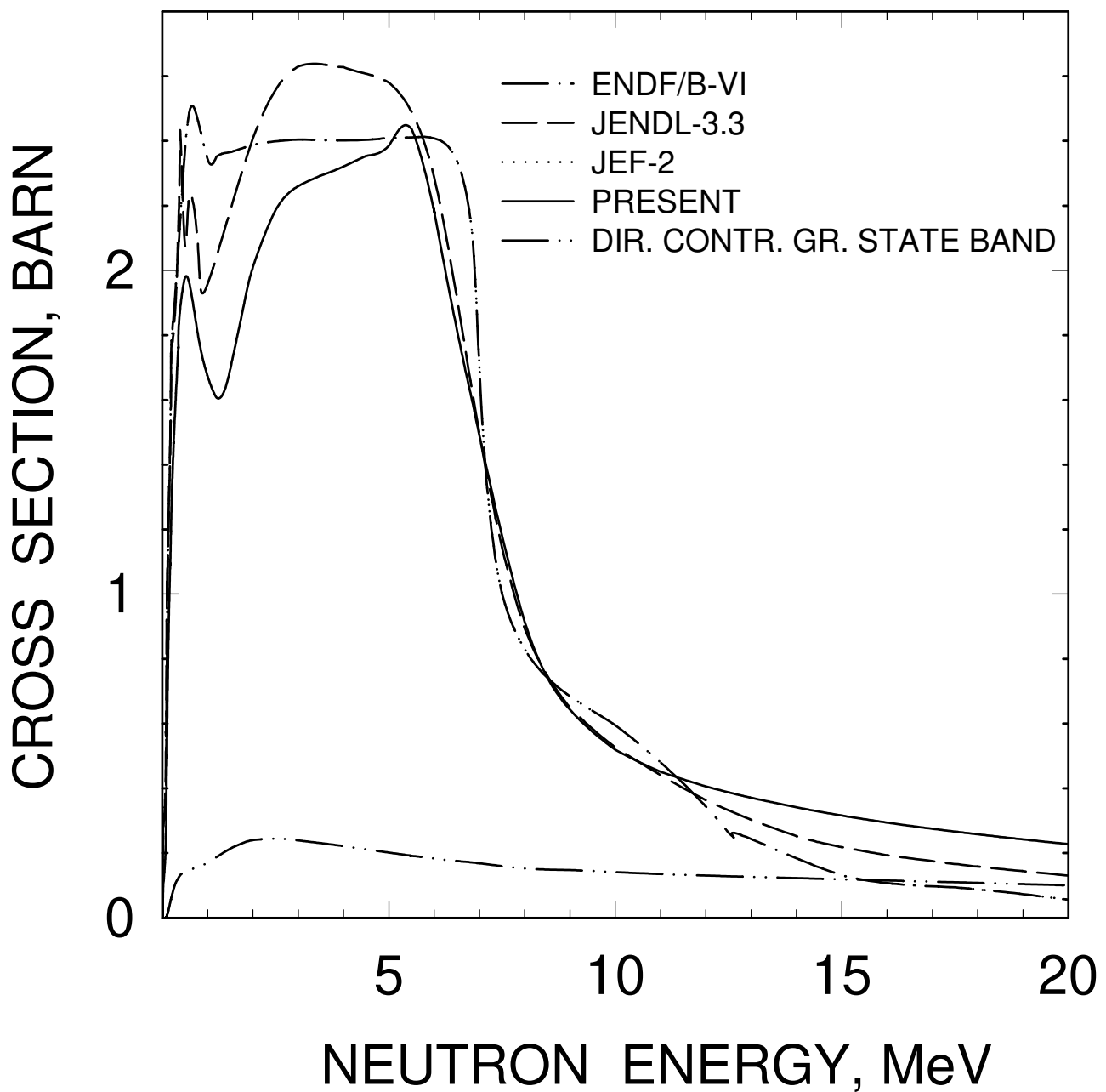


FIG. 51

^{231}Pa INELASTIC CROSS SECTION (CONTINUUM CONTRIBUTION)

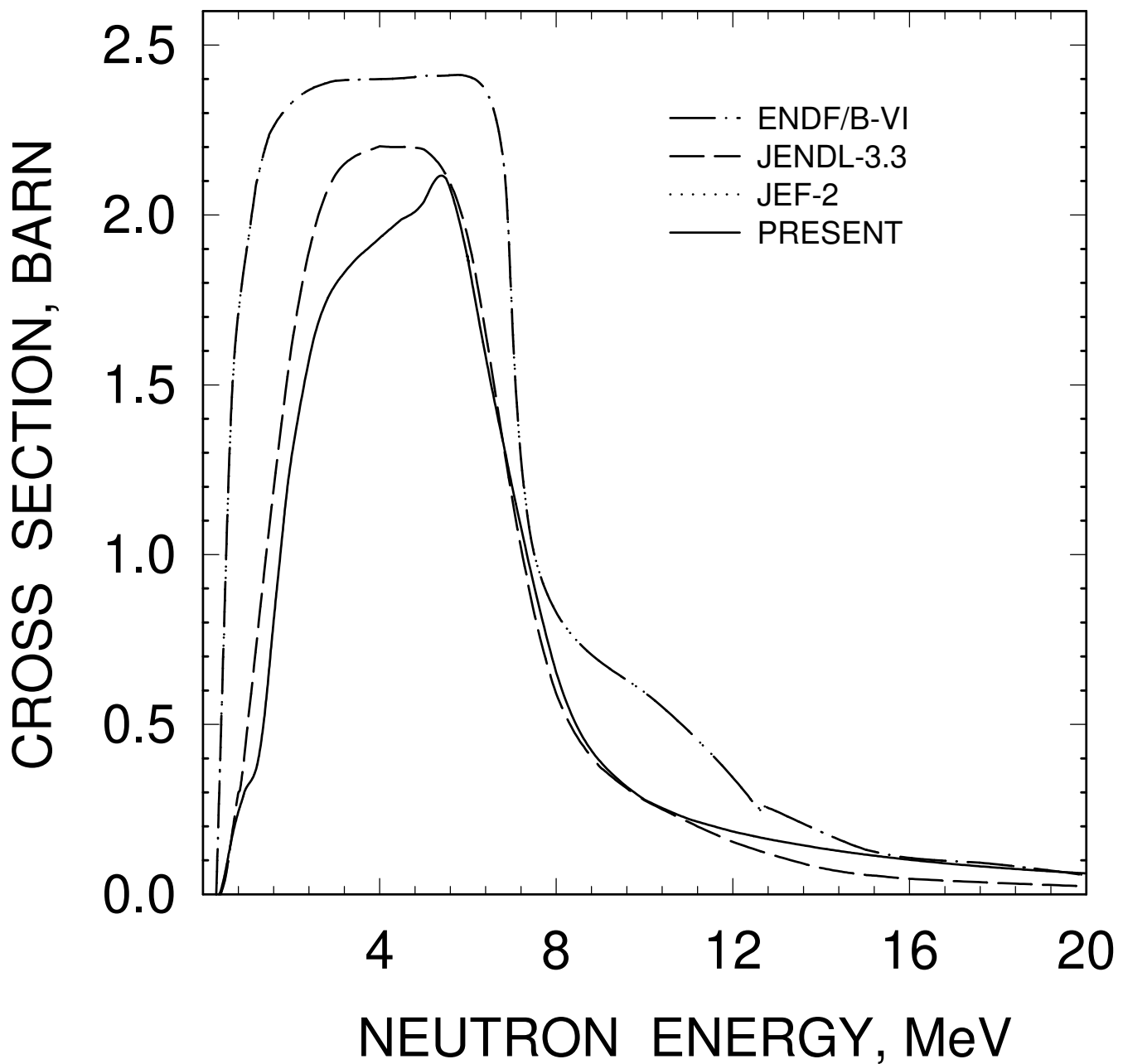


FIG. 52

^{231}Pa (n,γ) CROSS SECTION

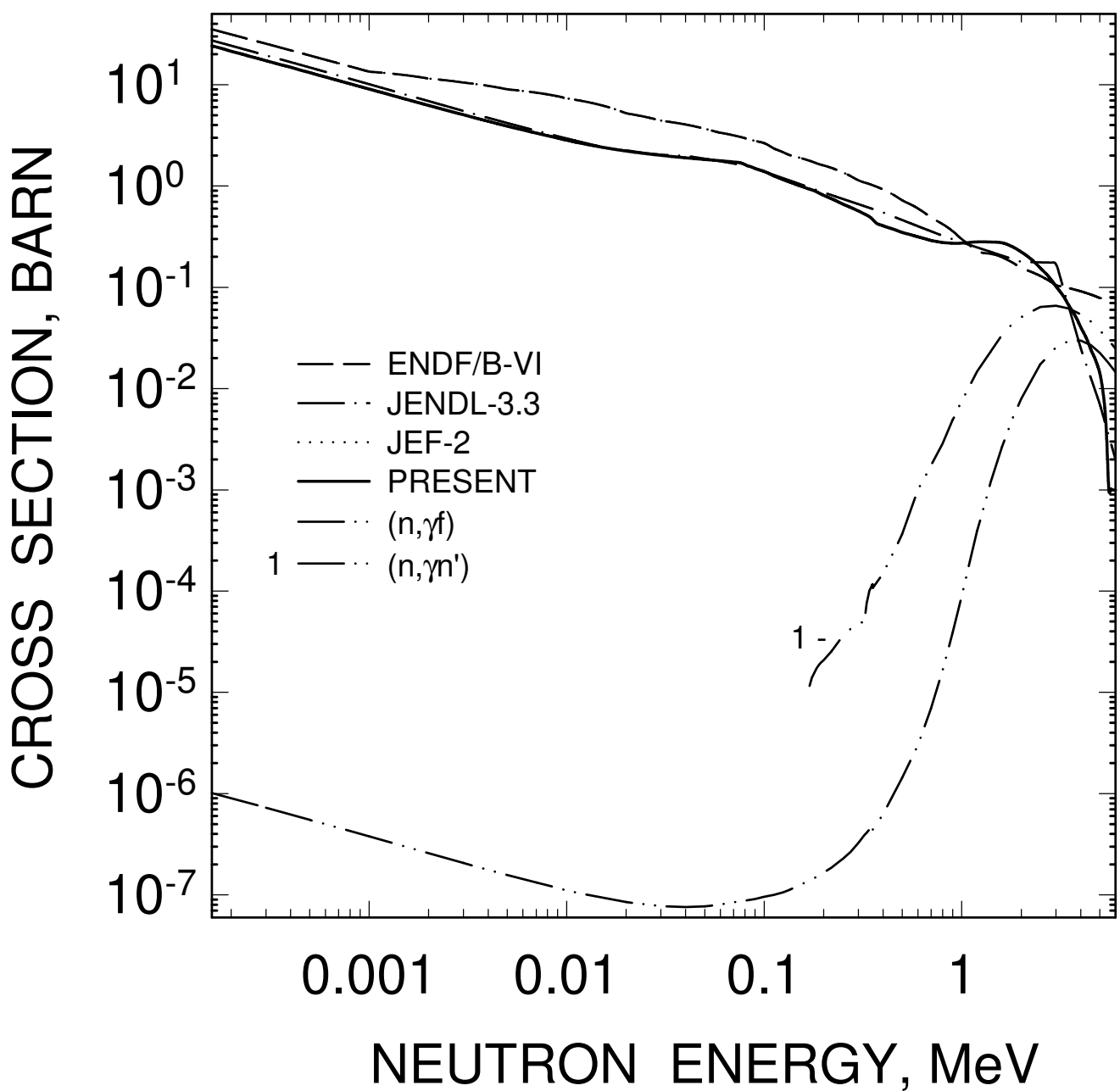


FIG. 53

^{231}Pa FISSION CROSS SECTION

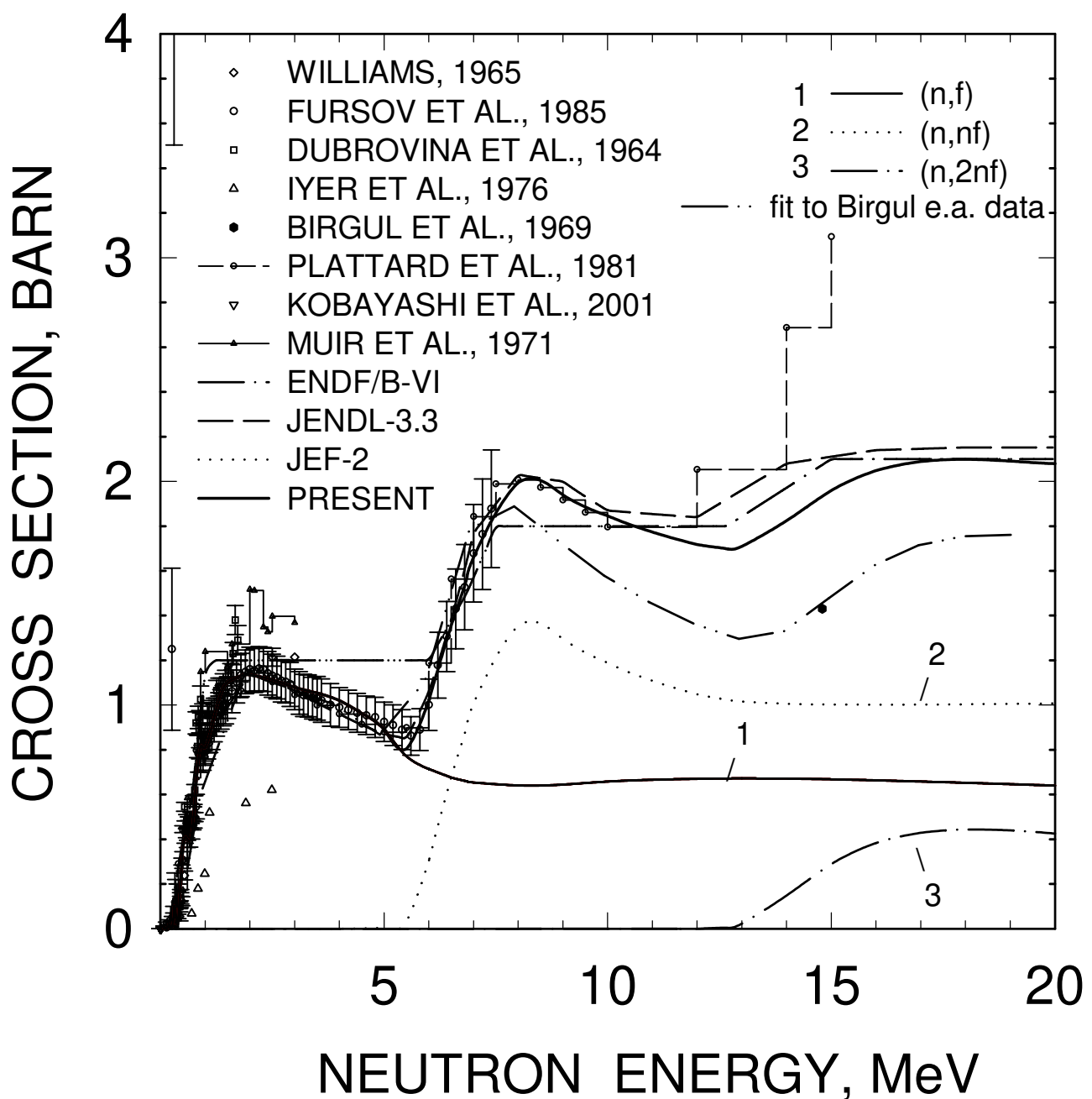


FIG. 54

$^{231}\text{Pa}(\text{n},\text{f})$ CHANCE FISSION CONTRIBUTIONS

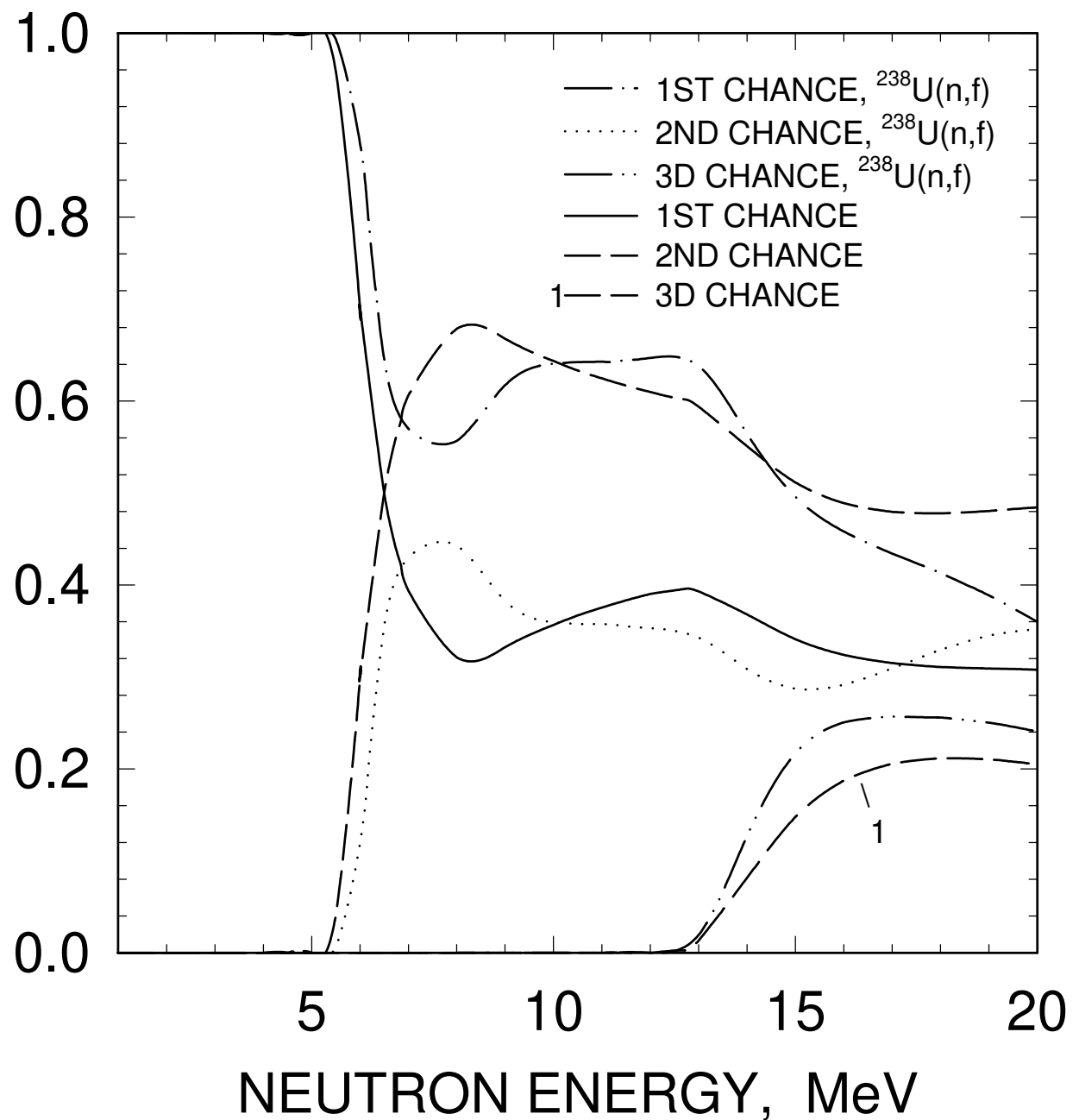


FIG. 55

$^{229}, ^{231}\text{Pa}$ FISSION CROSS SECTION

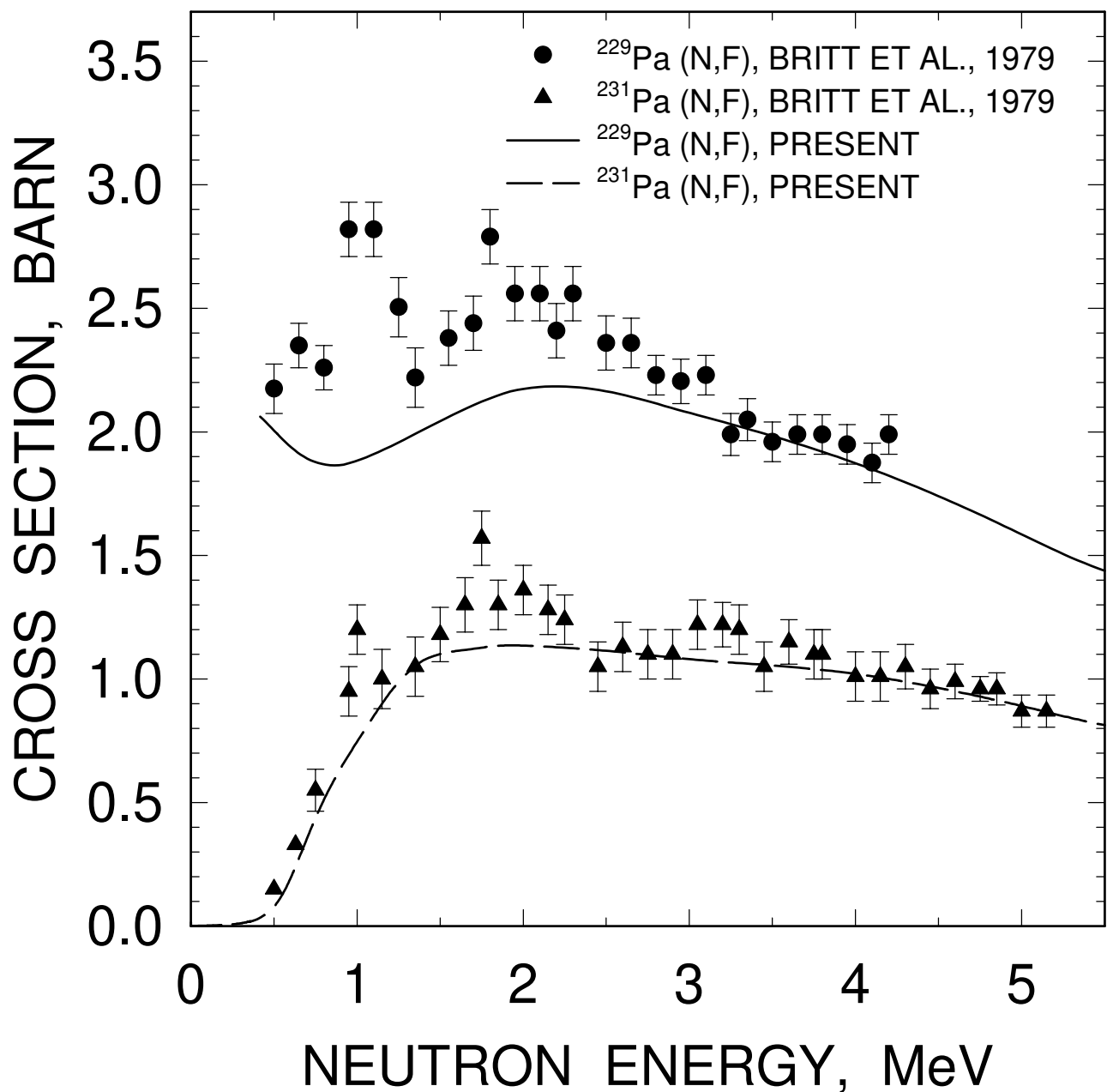


FIG. 56

^{230}Pa FISSION CROSS SECTION

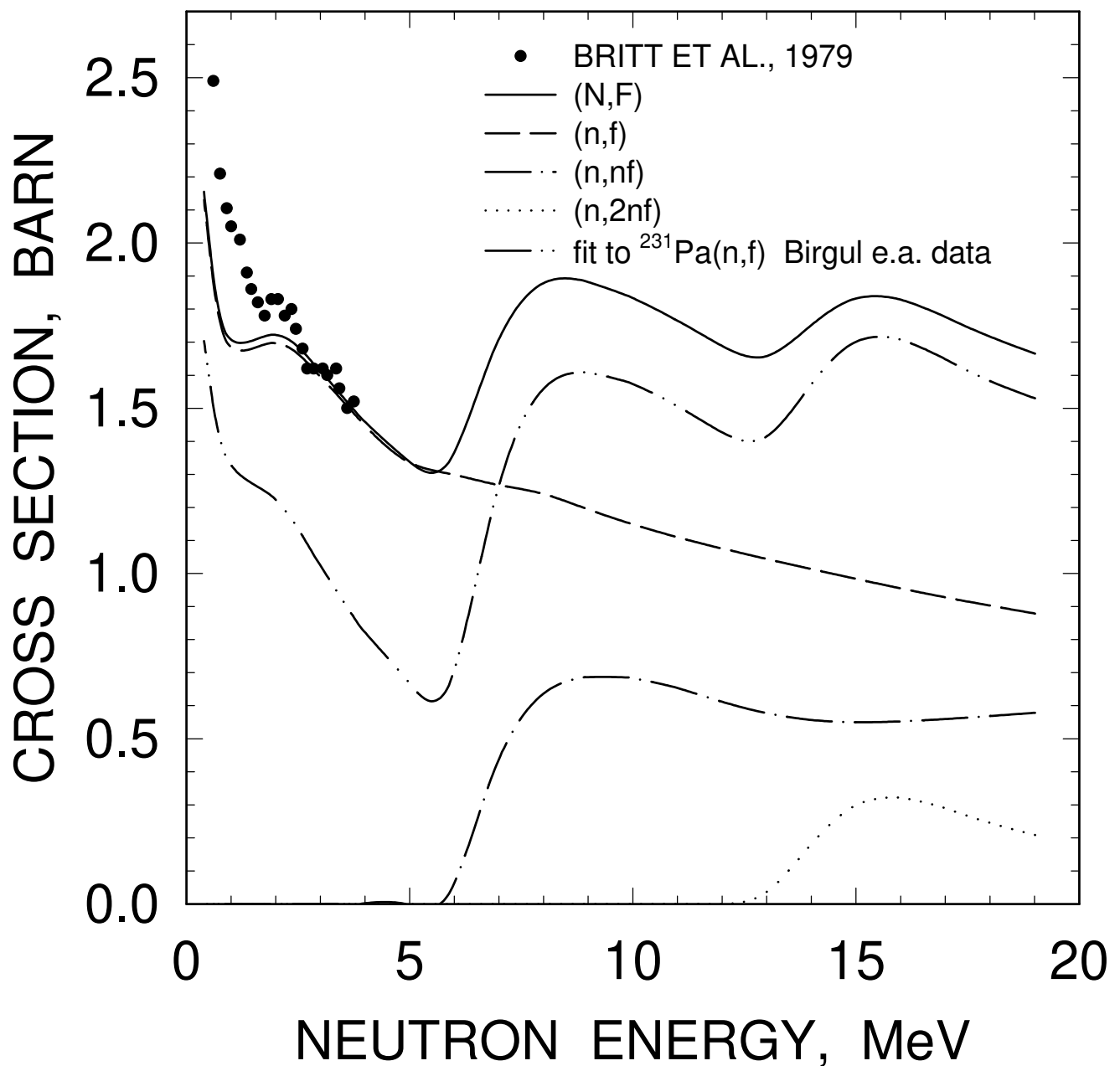


FIG. 57

^{231}Pa (N,2N) CROSS SECTION

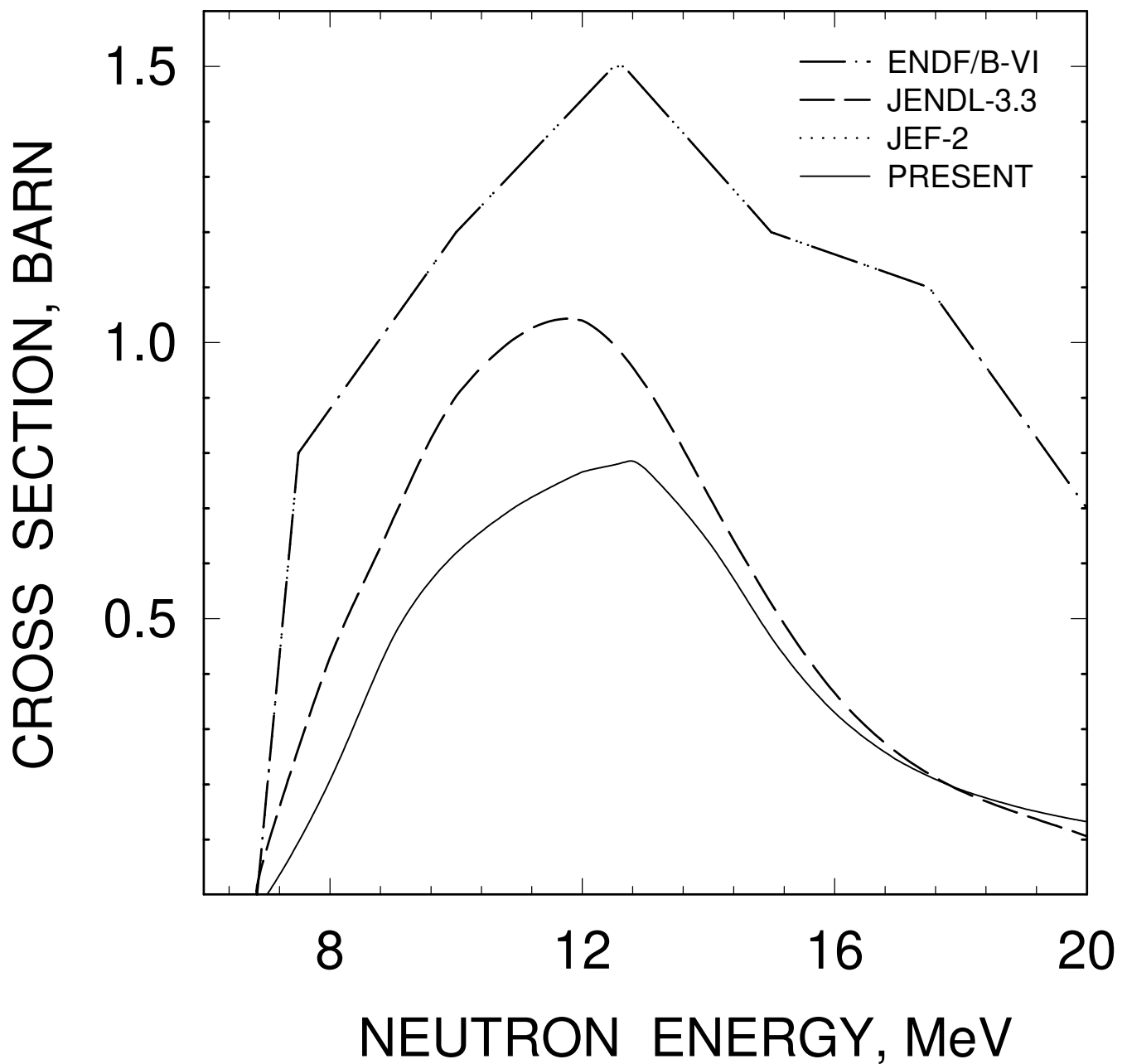


FIG. 58

^{231}Pa (N,3N) CROSS SECTION

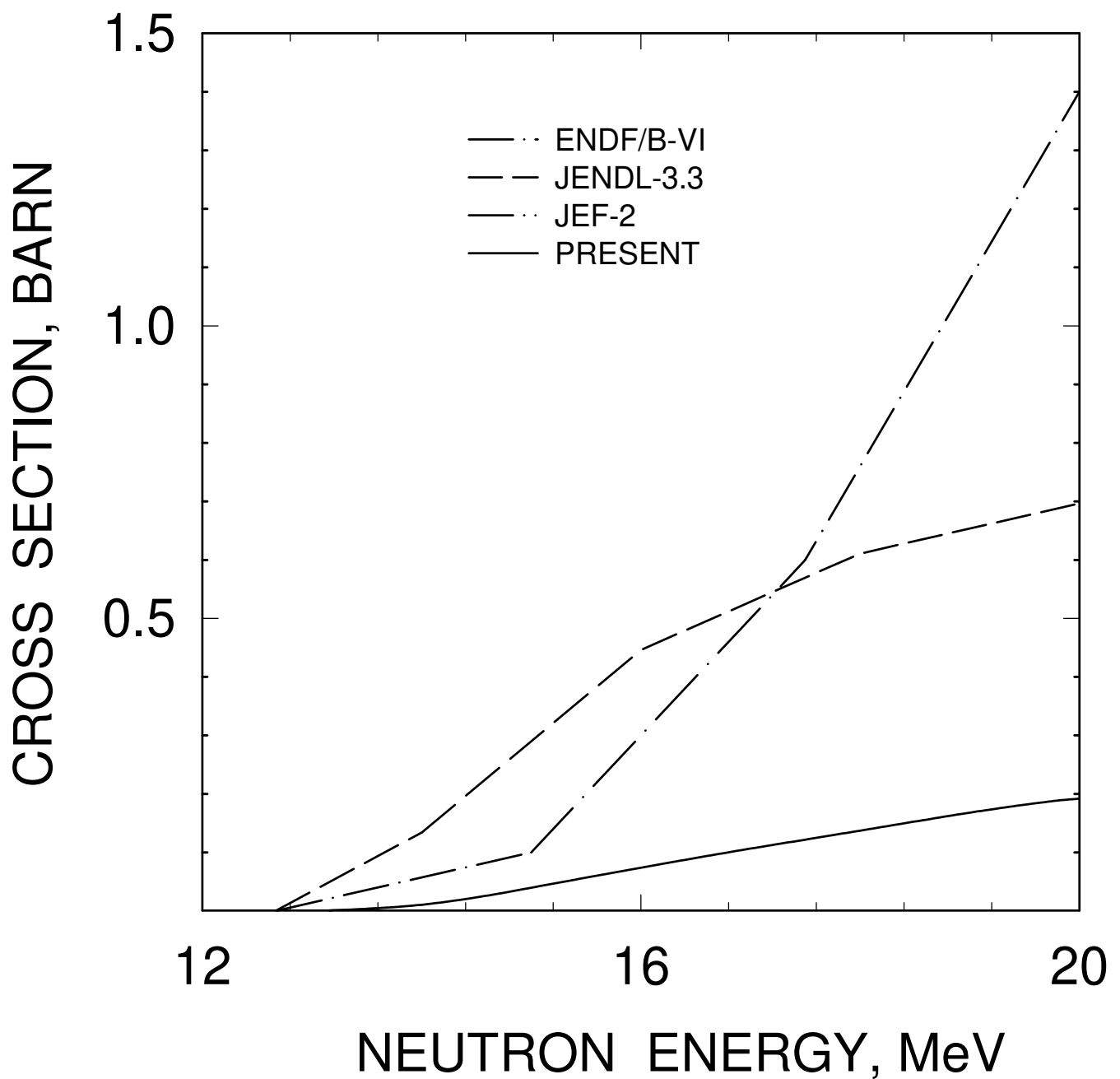


FIG. 59

^{231}Pa , NEUTRON MULTIPLICITY

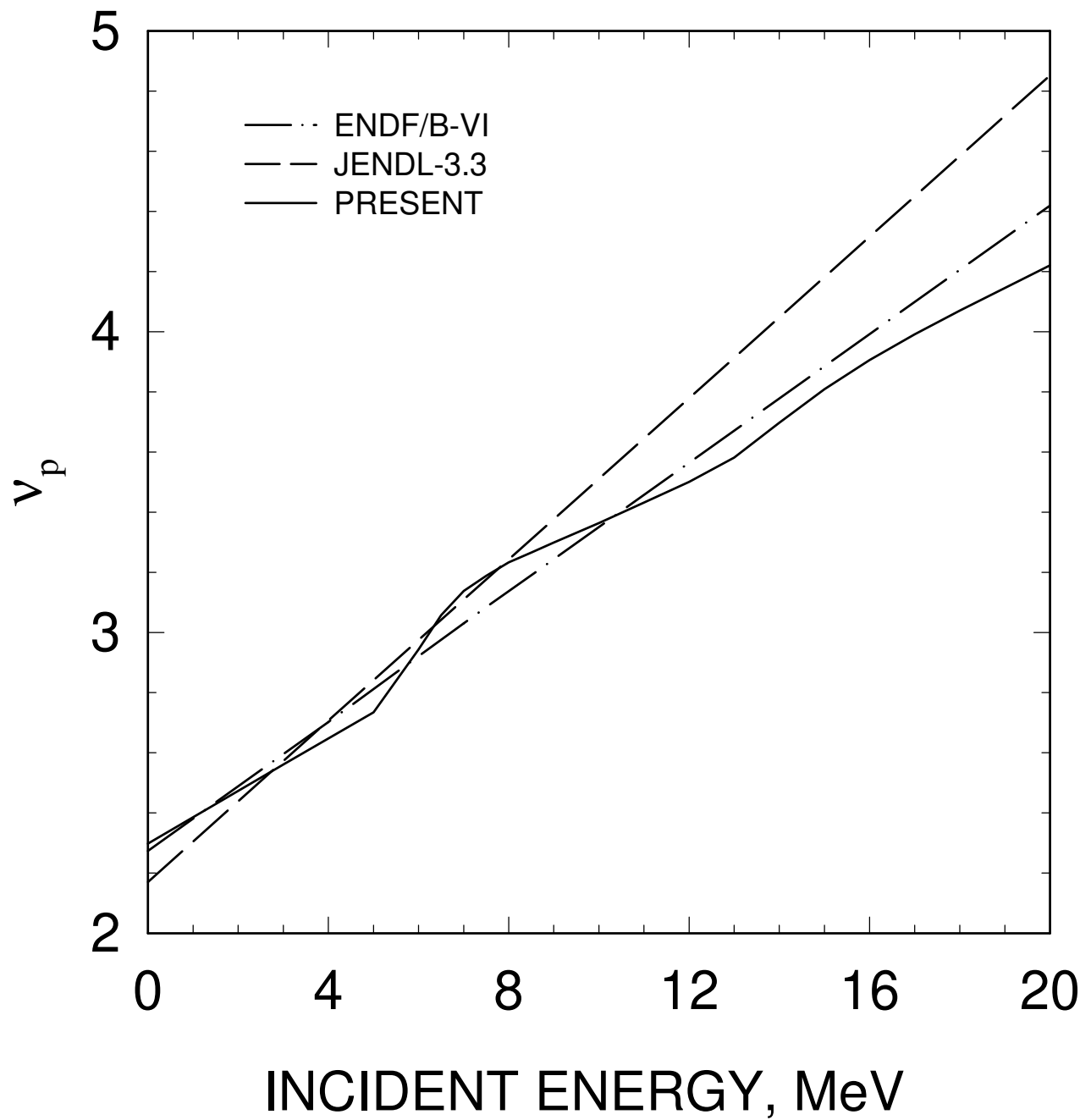
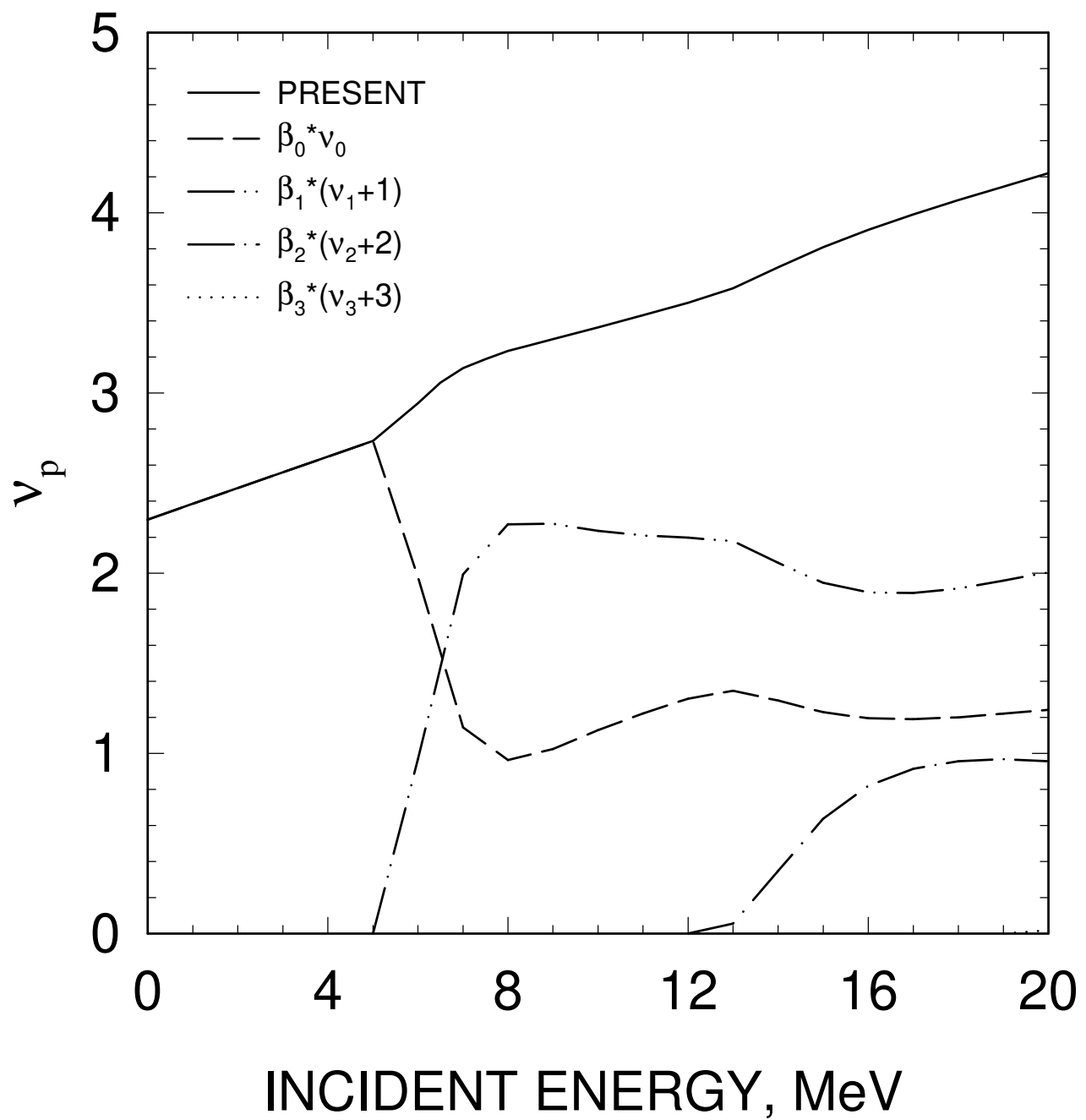


FIG. 60

^{231}Pa , NEUTRON MULTIPLICITY



INCIDENT ENERGY, MeV

FIG. 61

^{231}Pa $E_n = 20 \text{ MeV}$
COMPONENTS OF FIRST NEUTRON
SPECTRUM

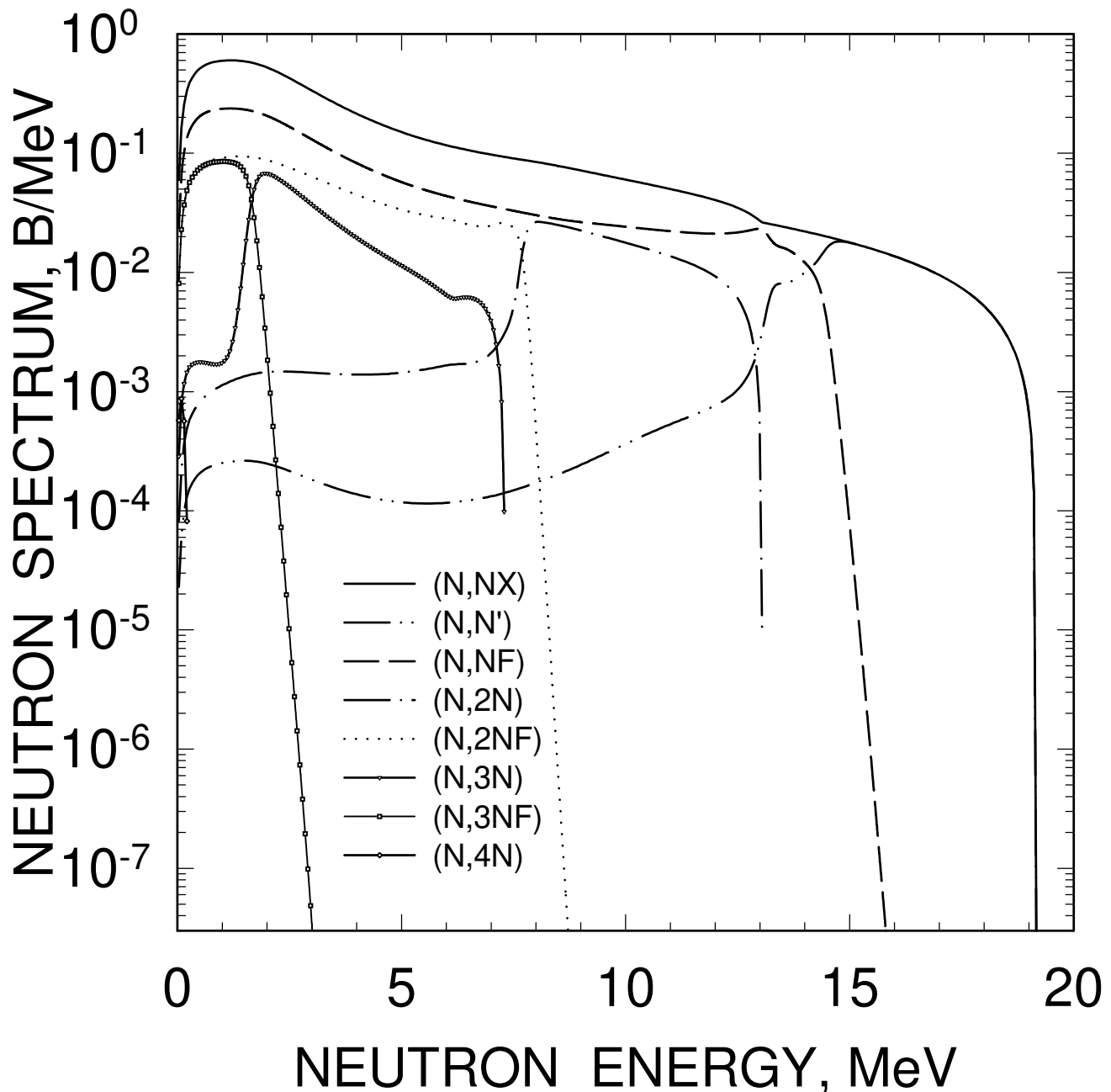


FIG. 62

^{231}Pa $E_n = 20 \text{ MeV}$
COMPONENTS OF SECOND NEUTRON
SPECTRUM

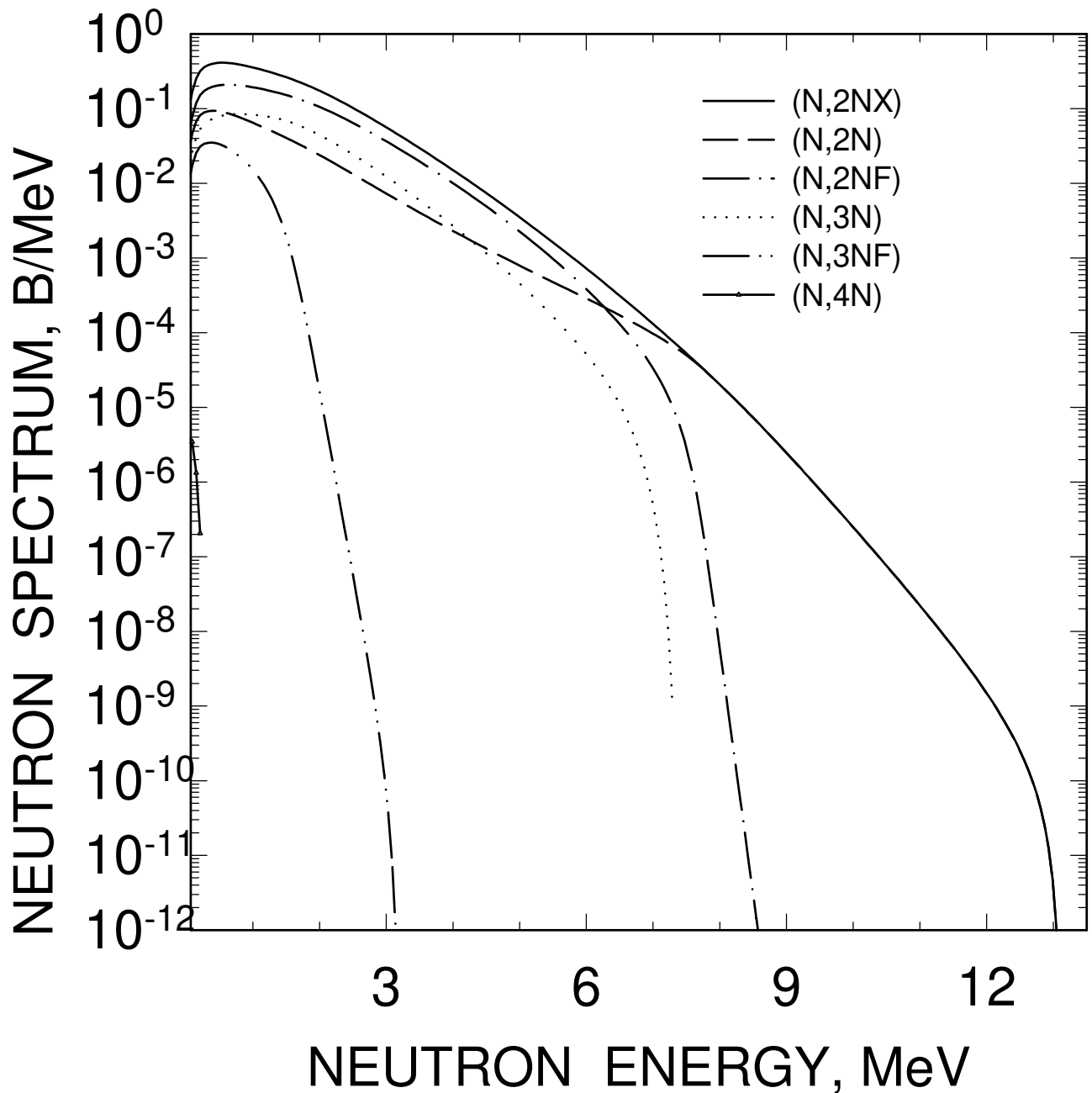


FIG. 63

^{231}Pa $E_n = 20 \text{ MeV}$
COMPONENTS OF THIRD NEUTRON
SPECTRUM

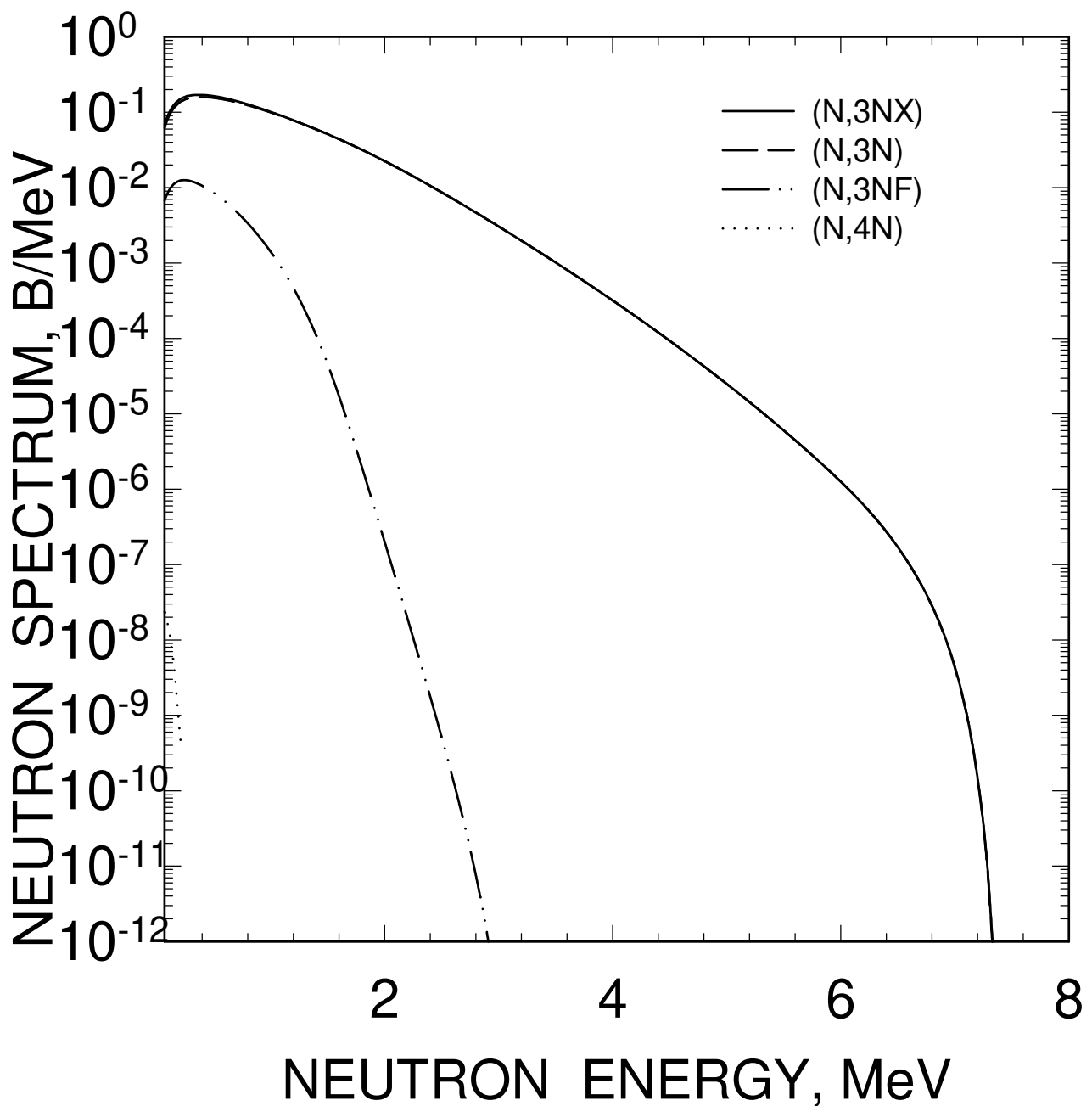


FIG. 64

^{231}Pa $E_n = 14 \text{ MeV}$

COMPONENTS OF FIRST NEUTRON SPECTRUM

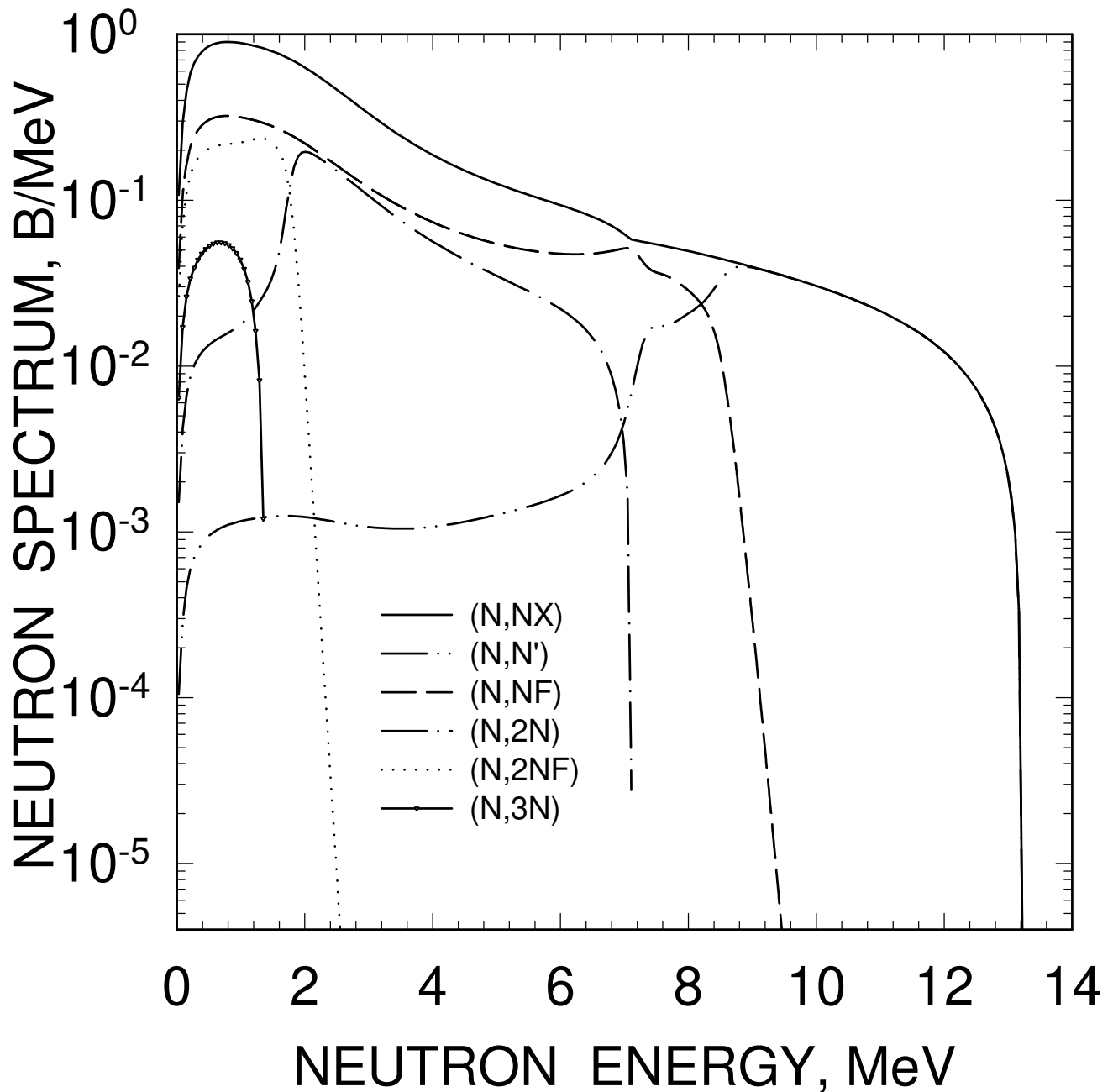


FIG. 65

^{231}Pa $E_n = 14 \text{ MeV}$
COMPONENTS OF SECOND NEUTRON
SPECTRUM

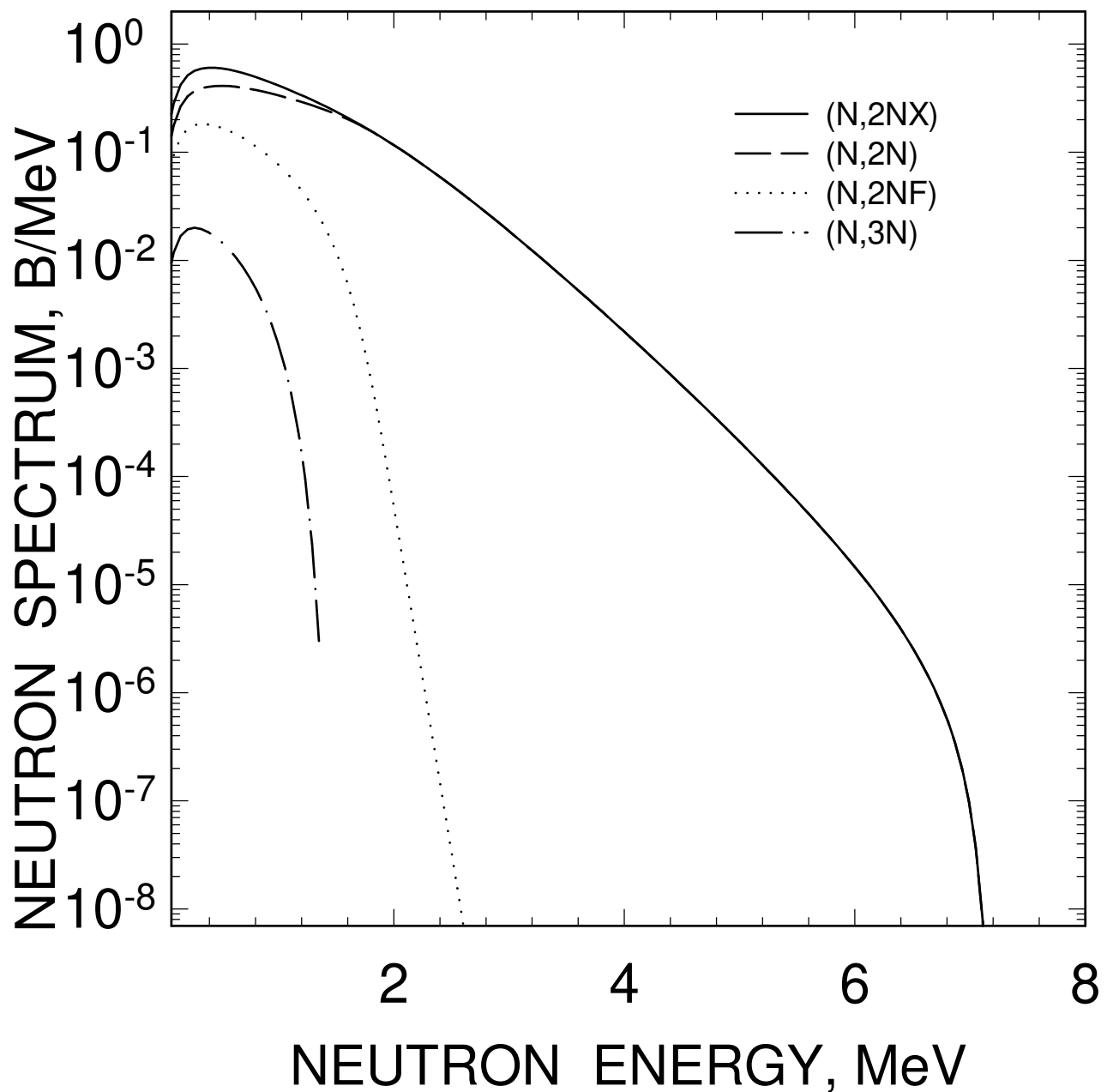


FIG. 66

^{231}Pa $E_n = 8 \text{ MeV}$

COMPONENTS OF FIRST NEUTRON SPECTRUM

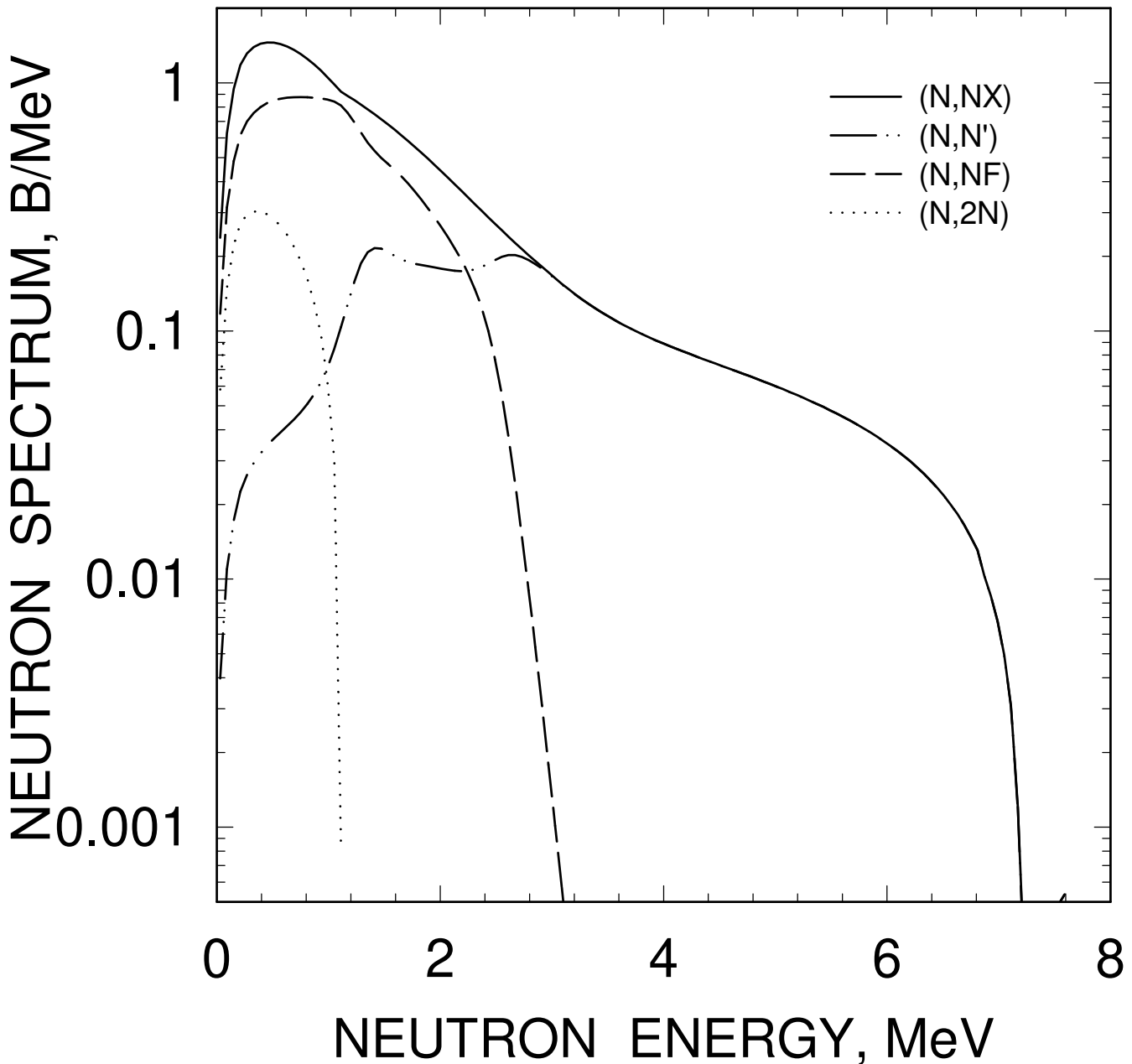


FIG. 67

^{231}Pa $E_n = 8 \text{ MeV}$
COMPONENTS OF SECOND NEUTRON
SPECTRUM

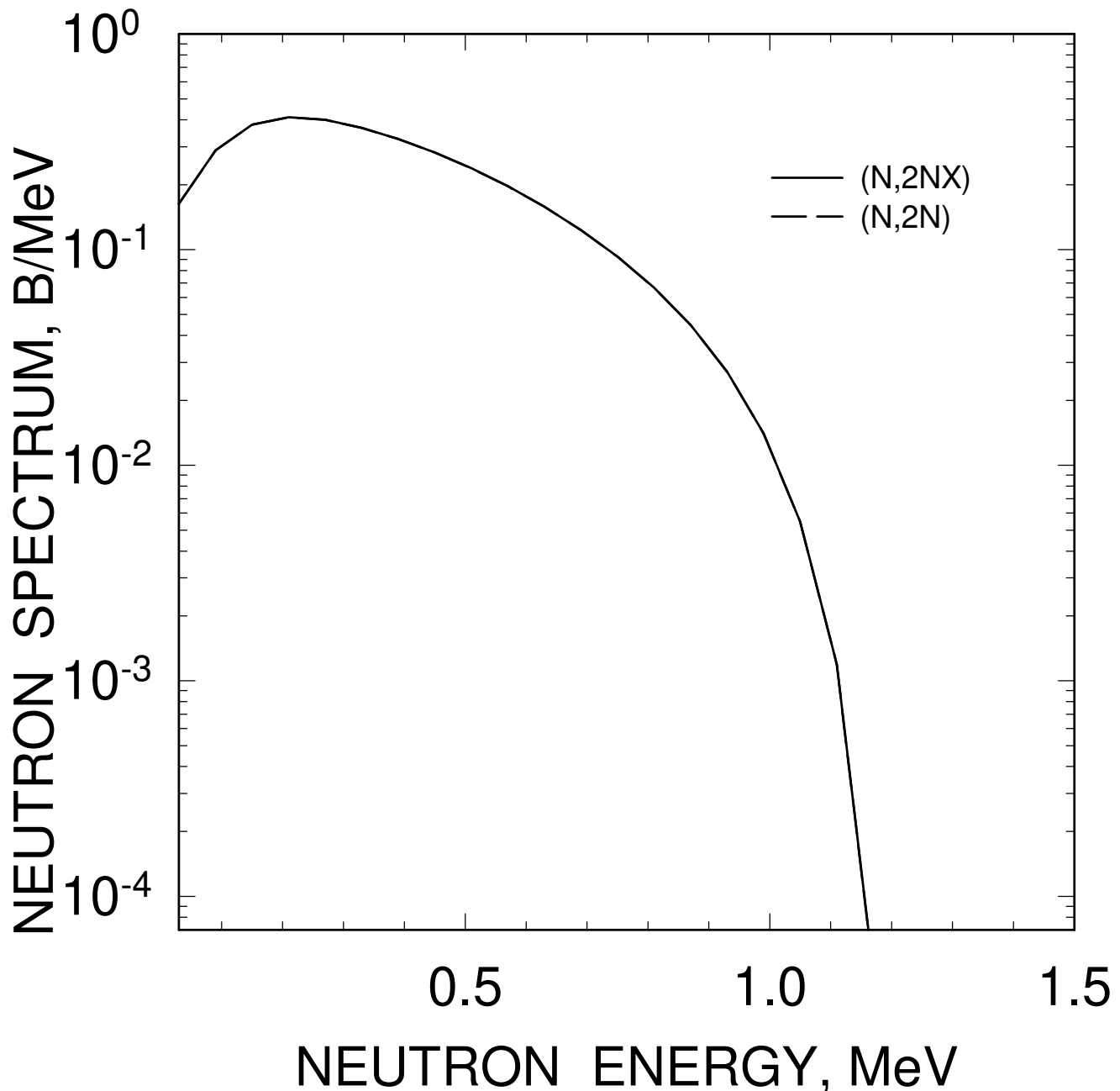


FIG. 68

^{231}Pa FISSION NEUTRON SPECTRUM
 $E_n=2 \text{ MeV}$

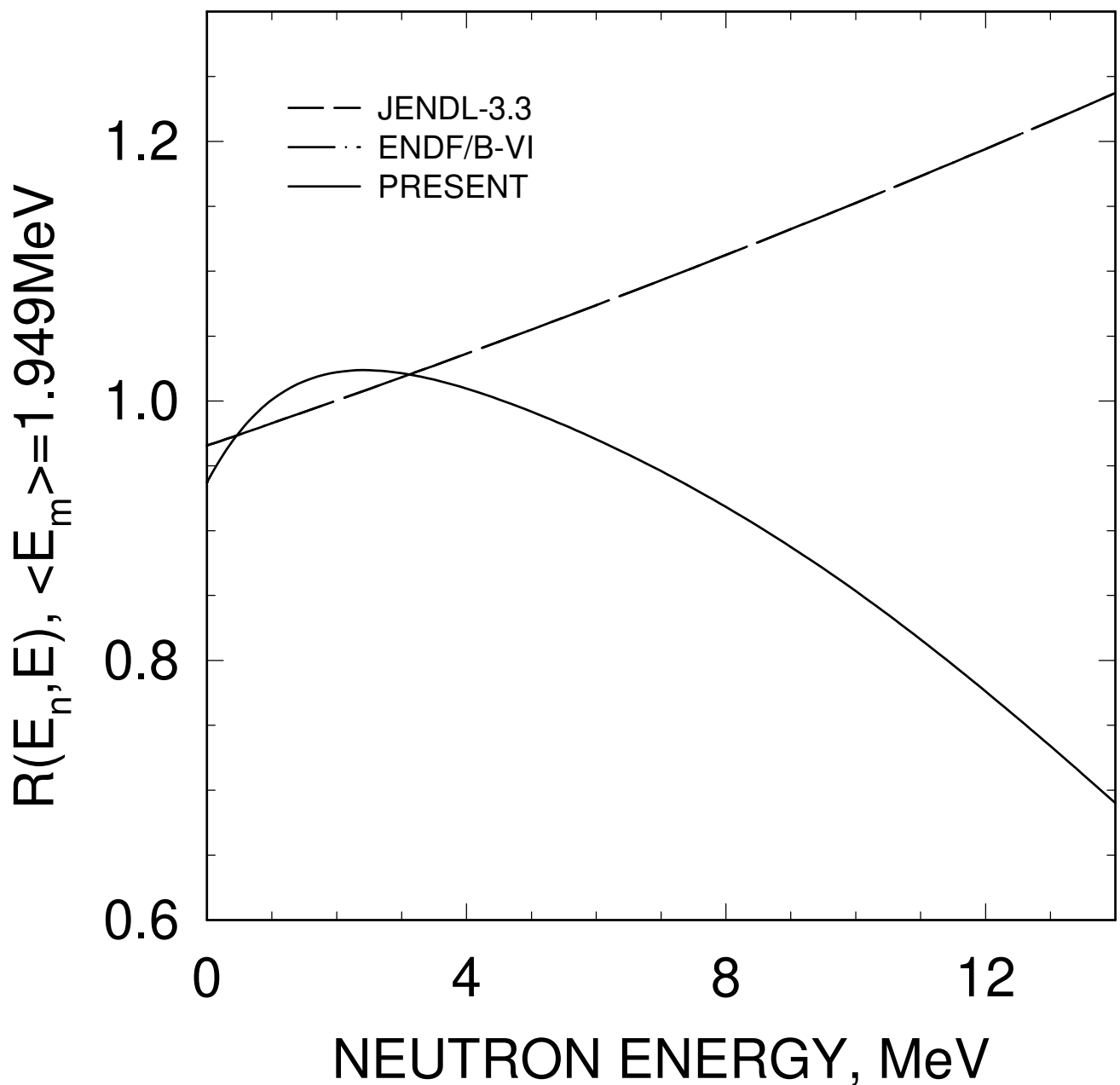


FIG. 69

^{231}Pa FISSION NEUTRON SPECTRUM
 $E_n = 7 \text{ MeV}$

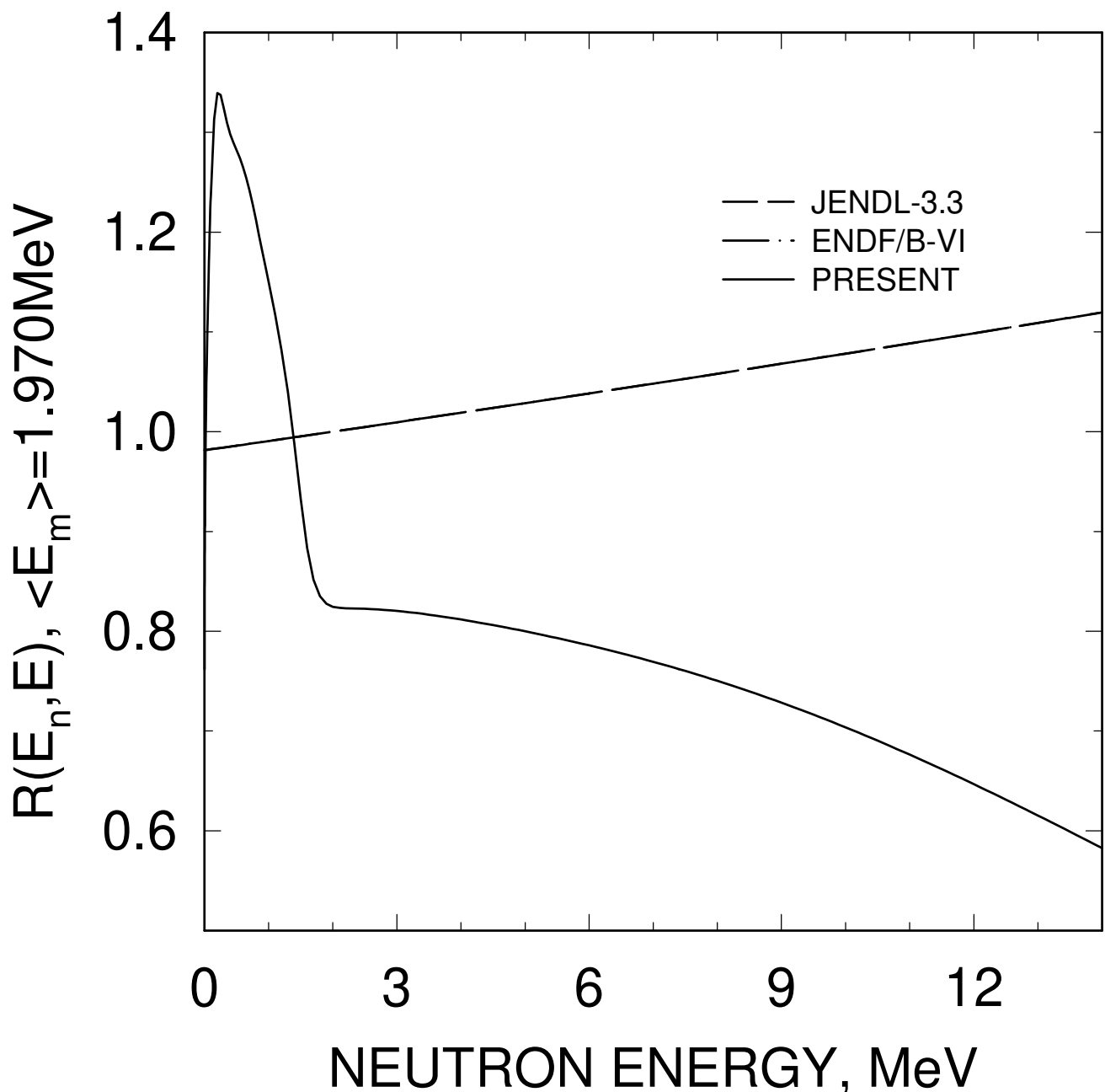


FIG. 70

^{233}Pa FISSION NEUTRON SPECTRUM
 $E_n=14$ MeV

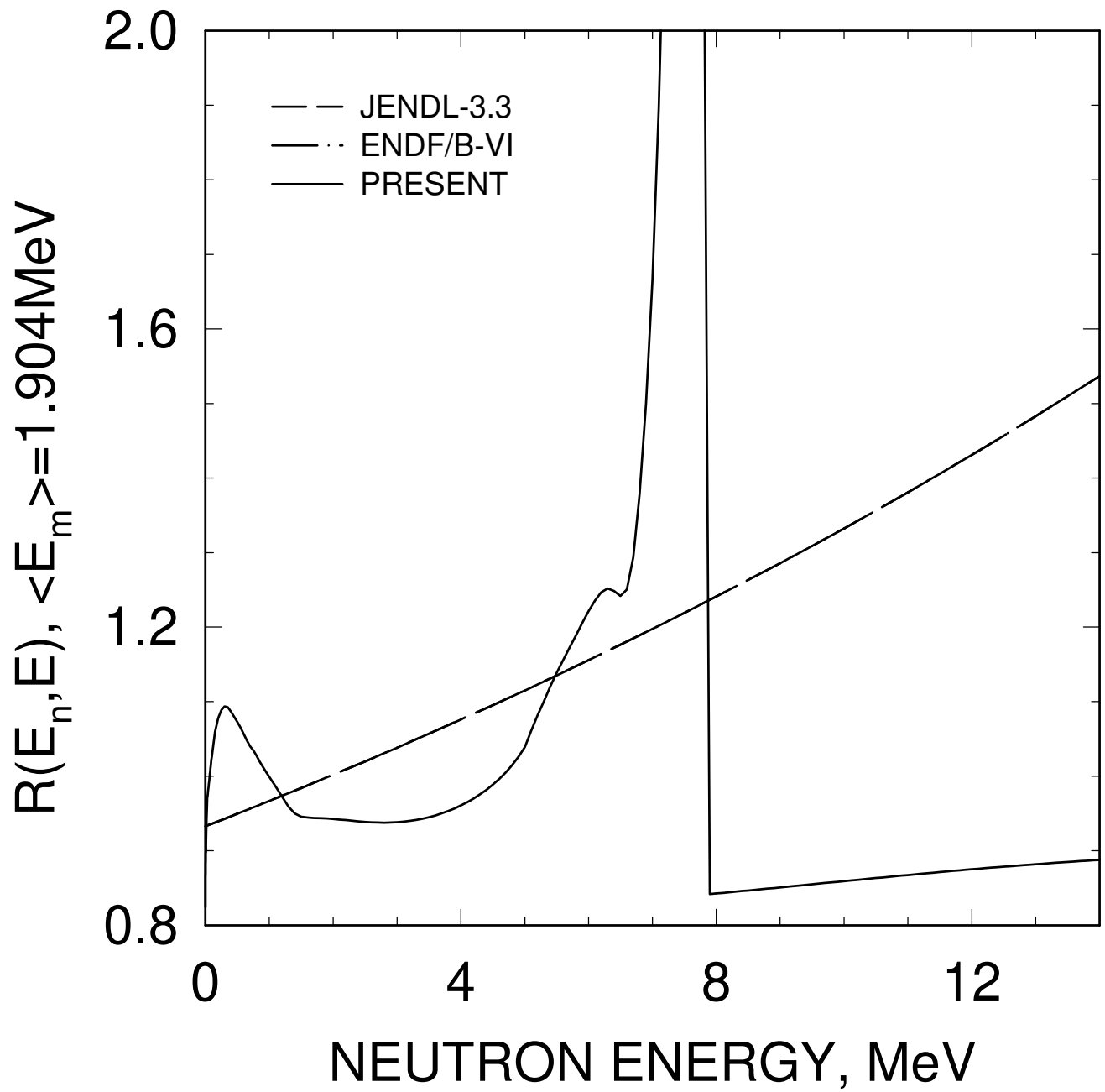


FIG. 71

^{231}Pa FISSION NEUTRON SPECTRUM
 $E_n=20$ MeV

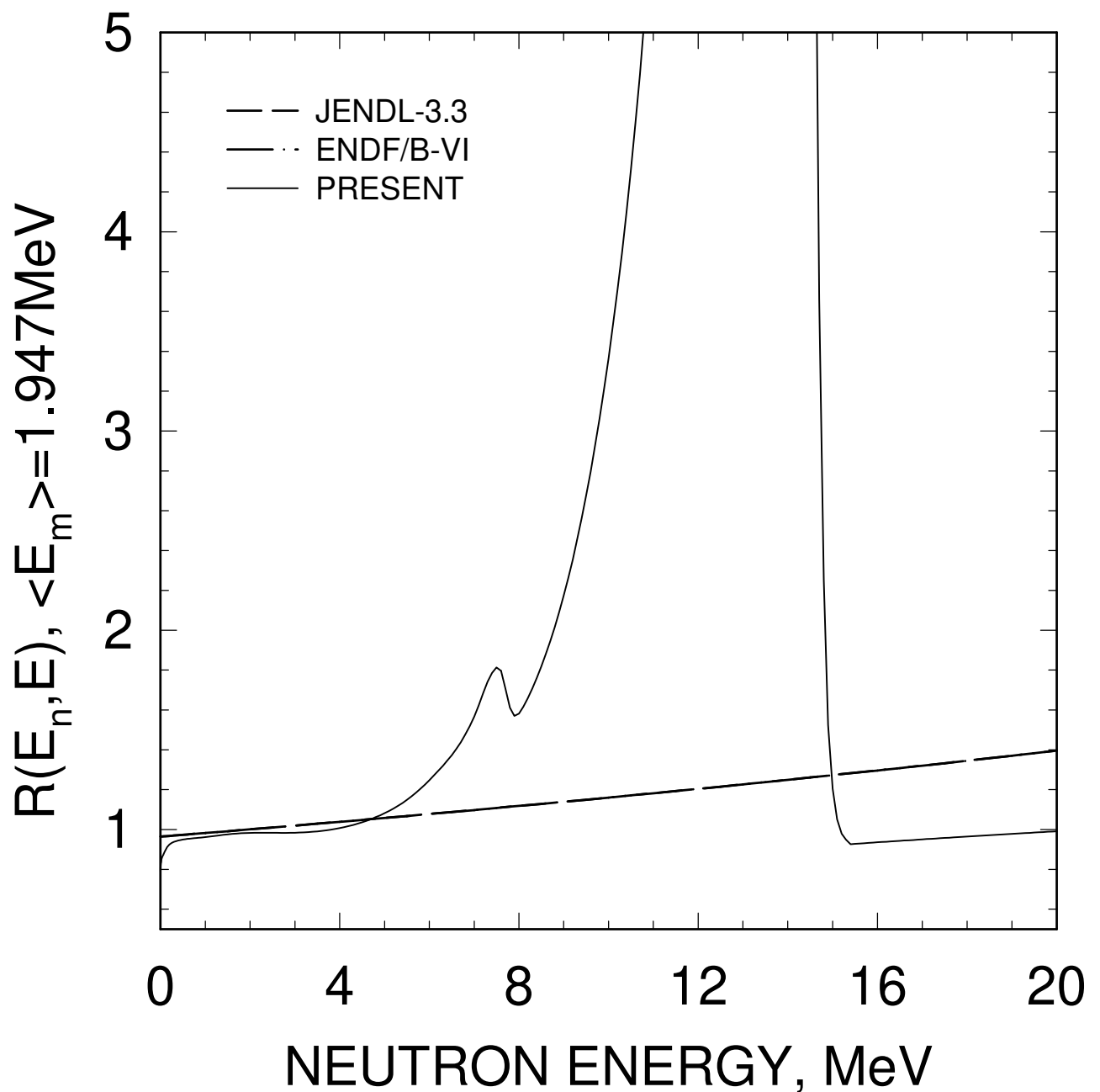


FIG. 72

^{231}Pa , AVERAGE NEUTRON ENERGY

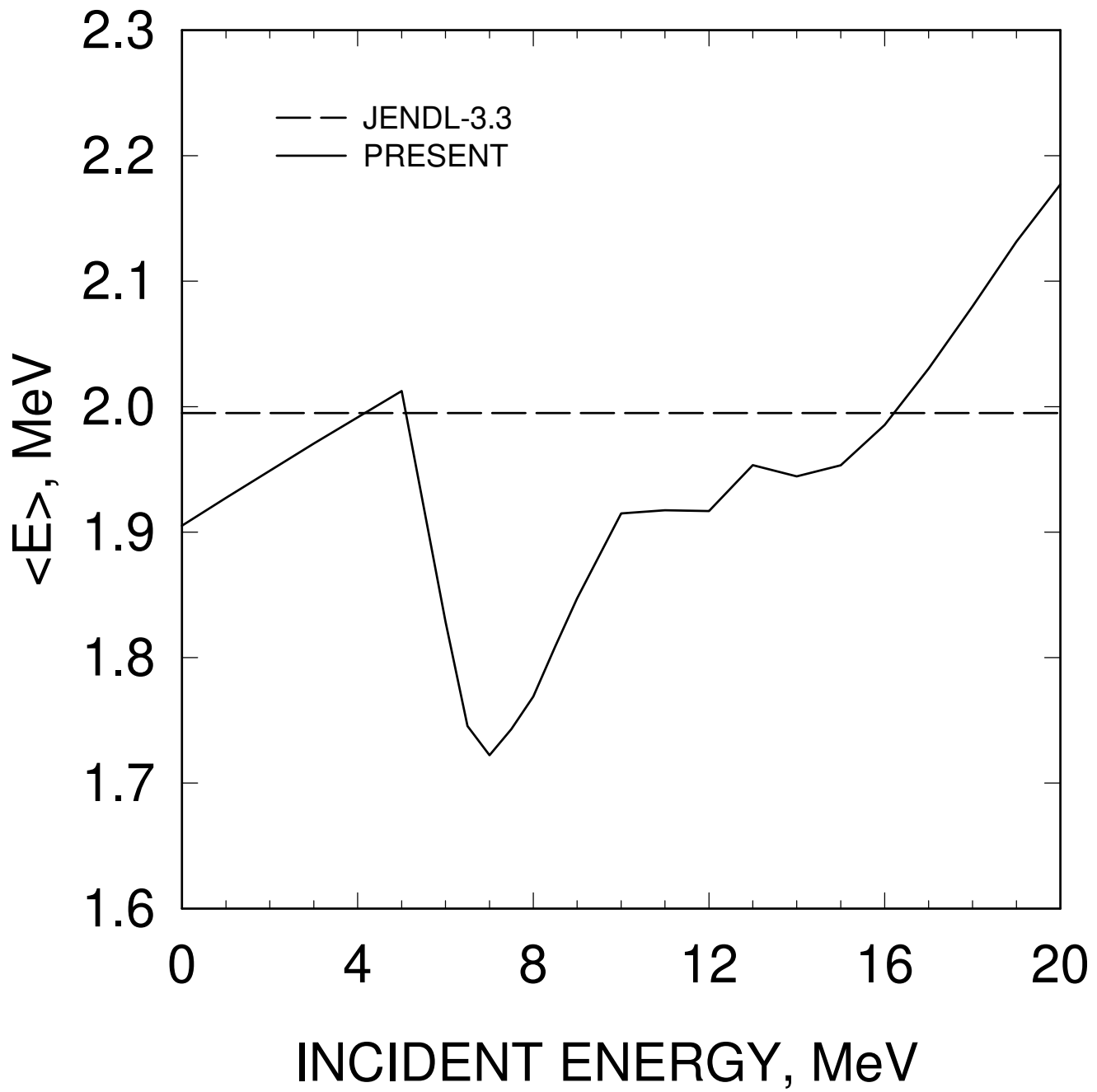


FIG. 73

^{231}Pa $E_n = 20 \text{ MeV}$
COMPARISON WITH JENDL-3.3
AND ENDF/B-VI

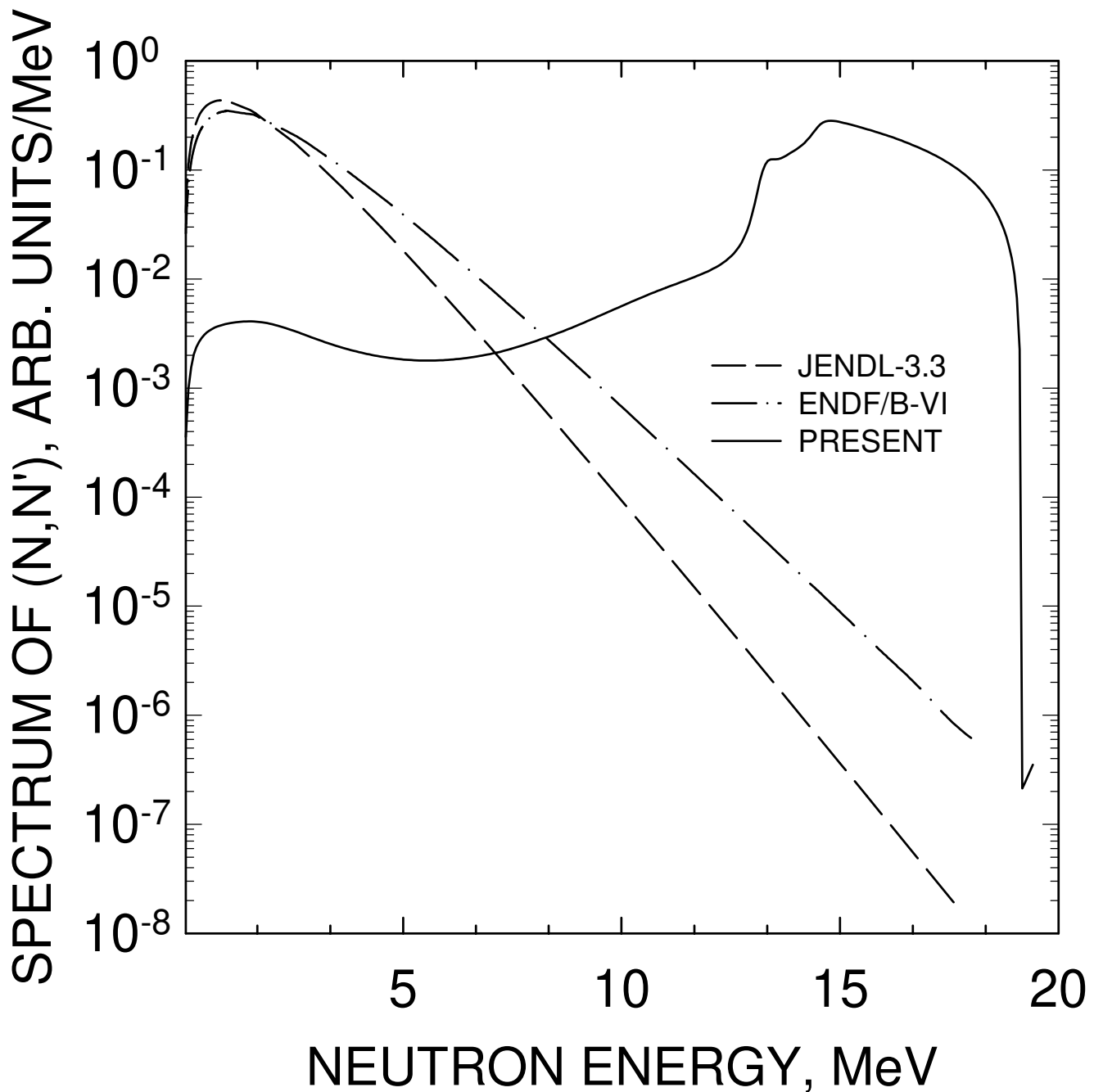


FIG. 74

^{231}Pa $E_n = 14 \text{ MeV}$
COMPARISON WITH JENDL-3.3

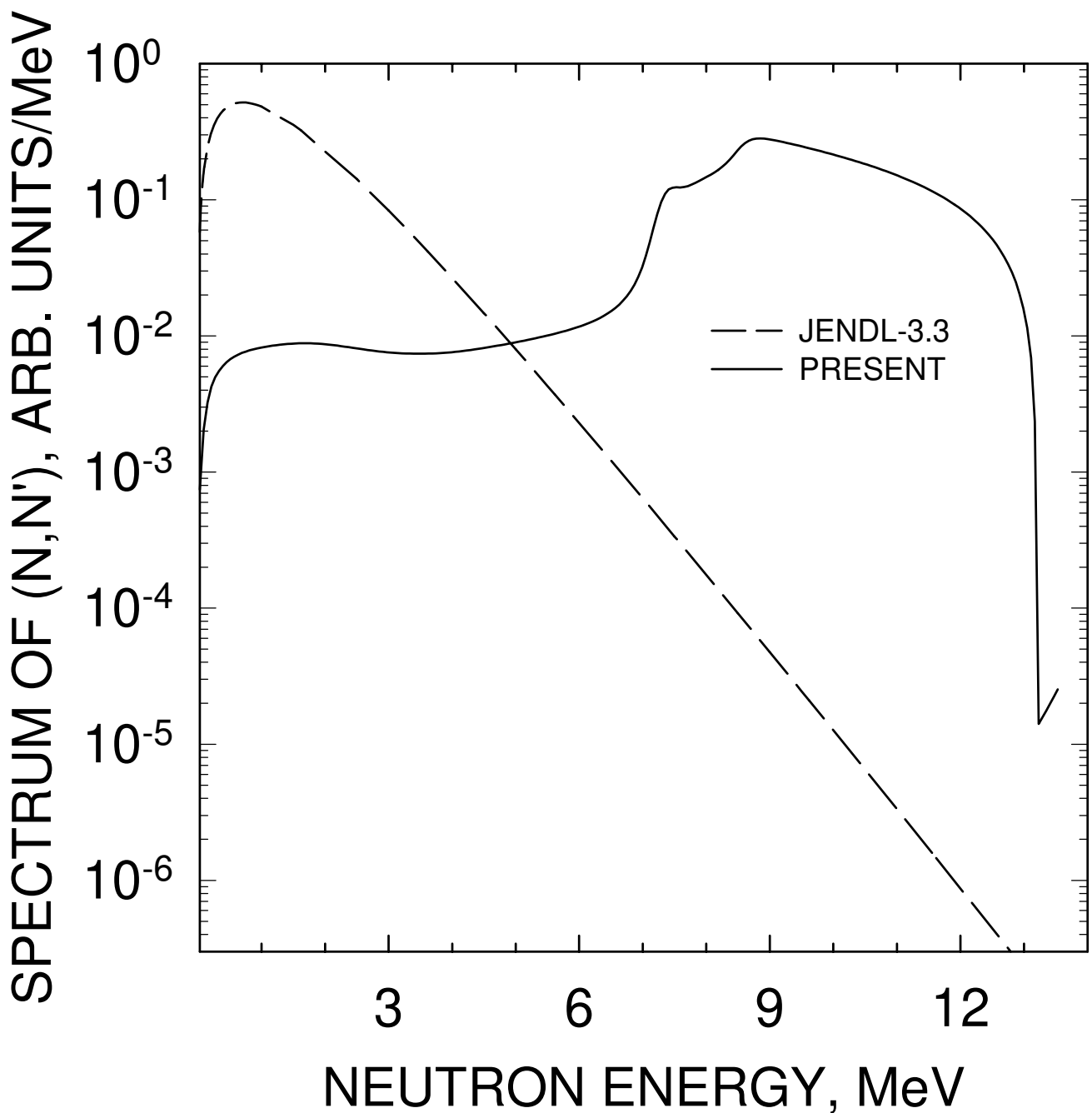


FIG. 75

^{231}Pa $E_n = 10 \text{ MeV}$
COMPARISON WITH JENDL-3.3
AND ENDF/B-VI

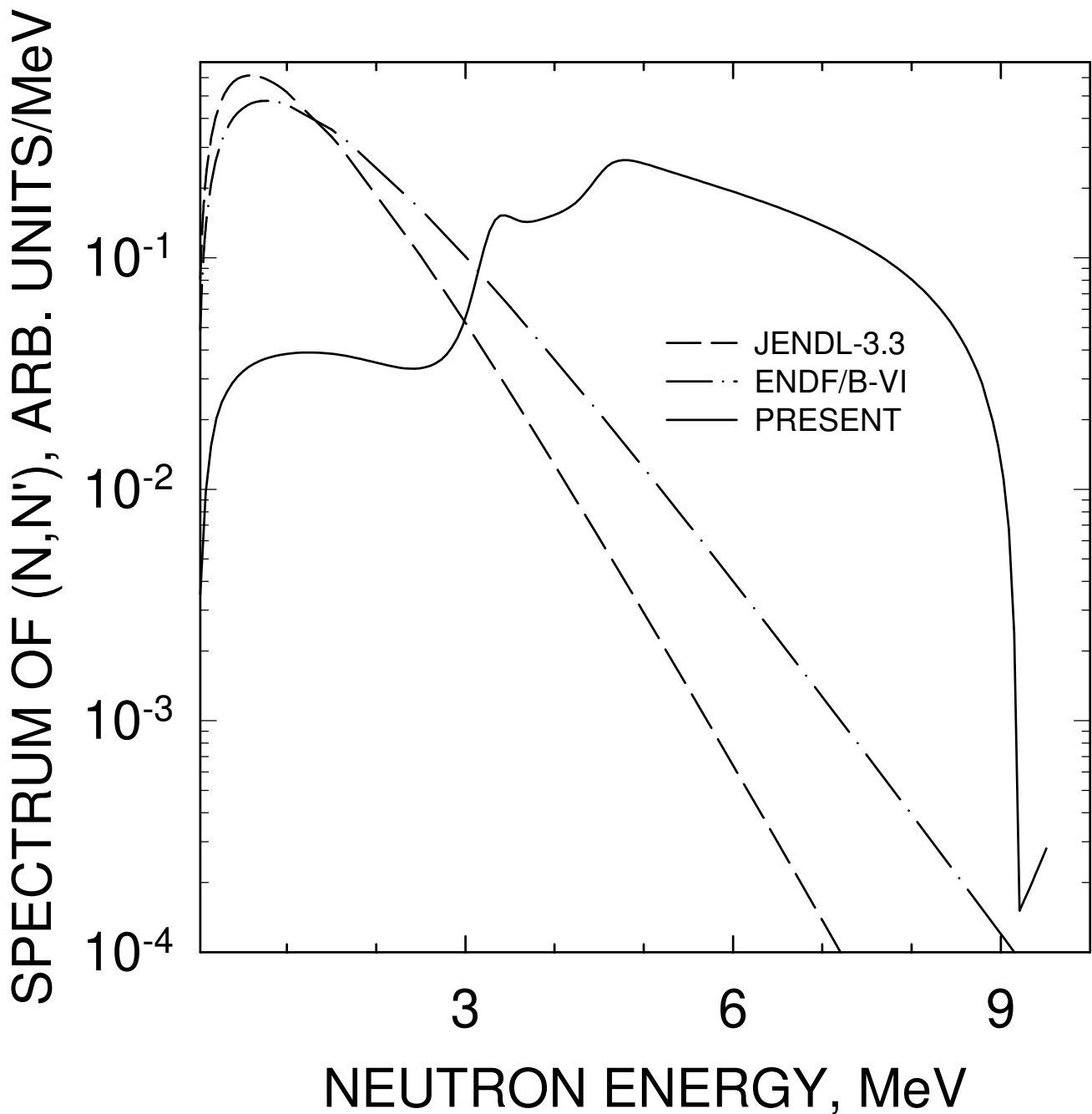


FIG. 76

^{231}Pa $E_n = 8 \text{ MeV}$
COMPARISON WITH JENDL-3.3

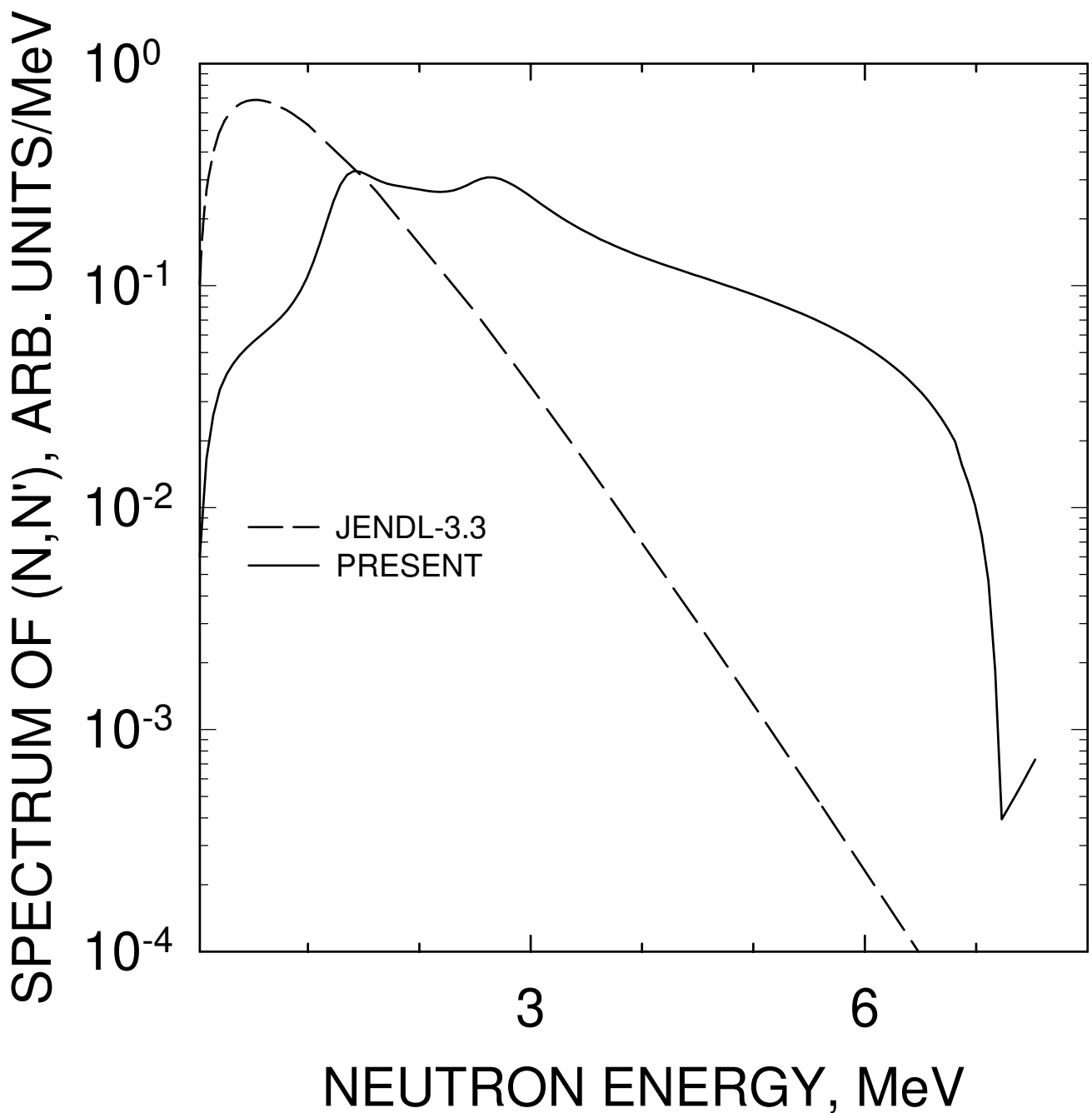


FIG. 77

^{231}Pa $E_n = 6 \text{ MeV}$
COMPARISON WITH JENDL-3.3
AND ENDF/B-VI

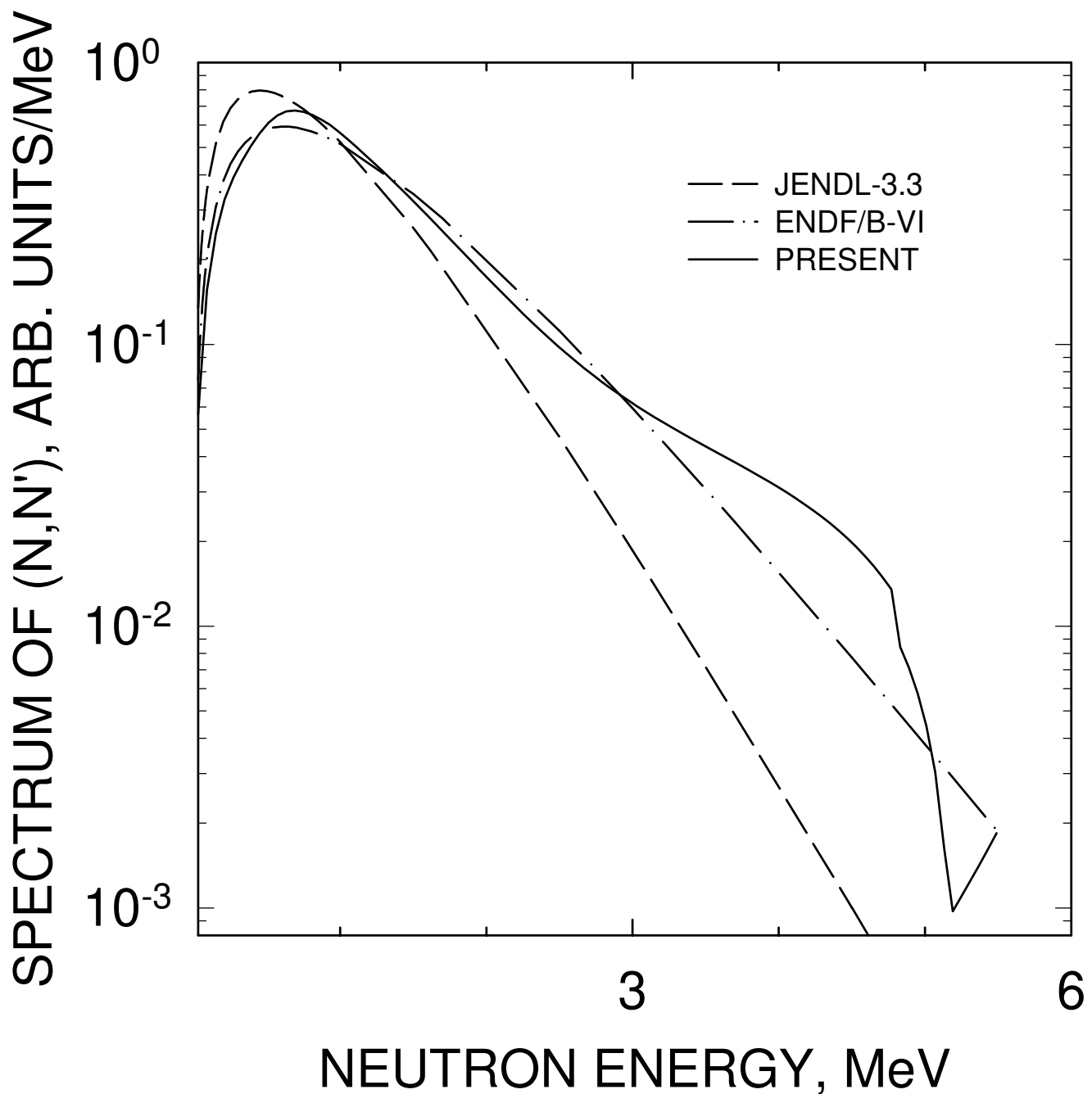


FIG. 78

^{231}Pa $E_n = 4 \text{ MeV}$
COMPARISON WITH JENDL-3.3
AND ENDF/B-VI

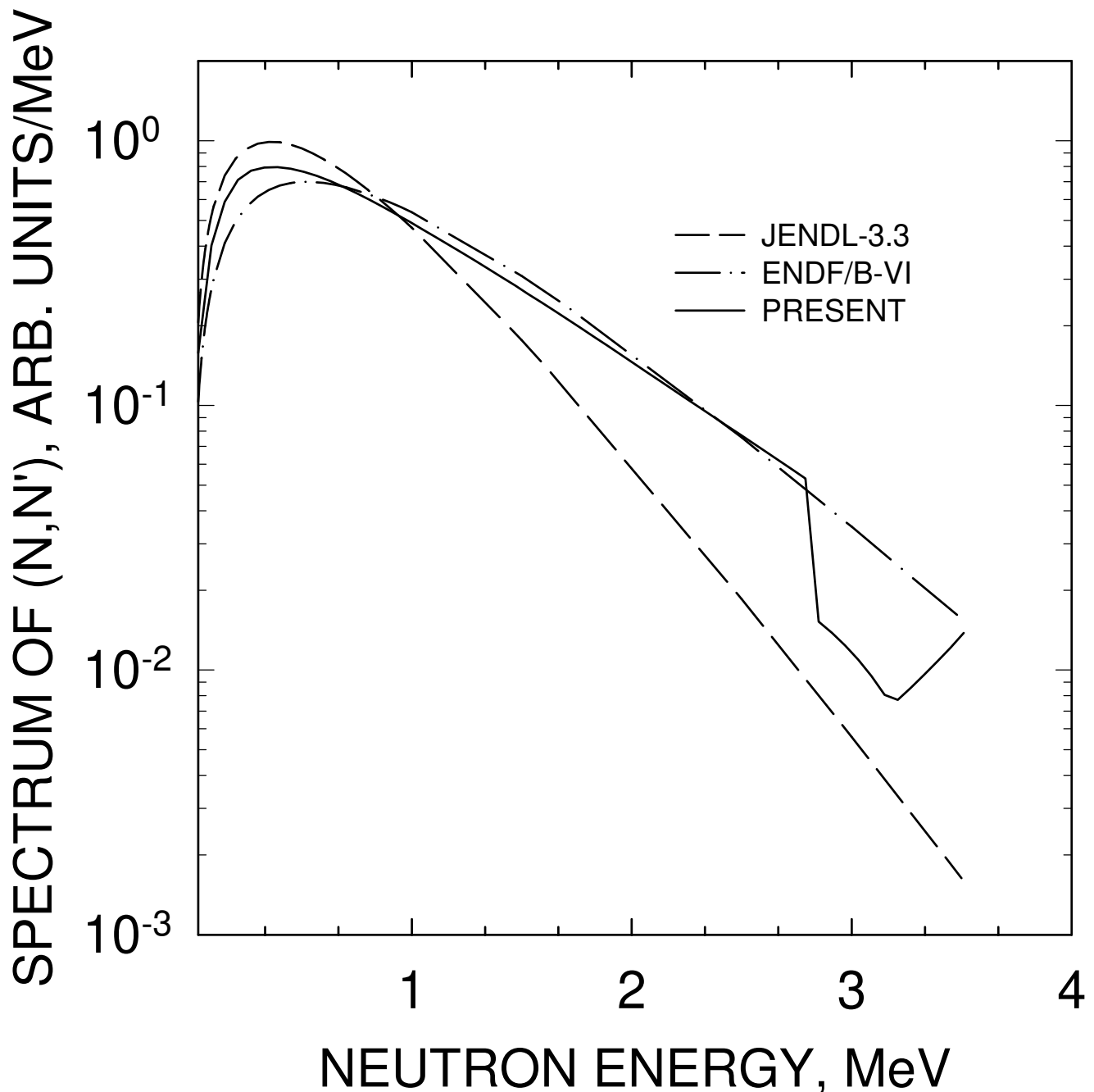


FIG. 79

^{231}Pa $E_n = 20$ MeV
COMPARISON WITH JENDL-3.3
AND ENDF/B-VI

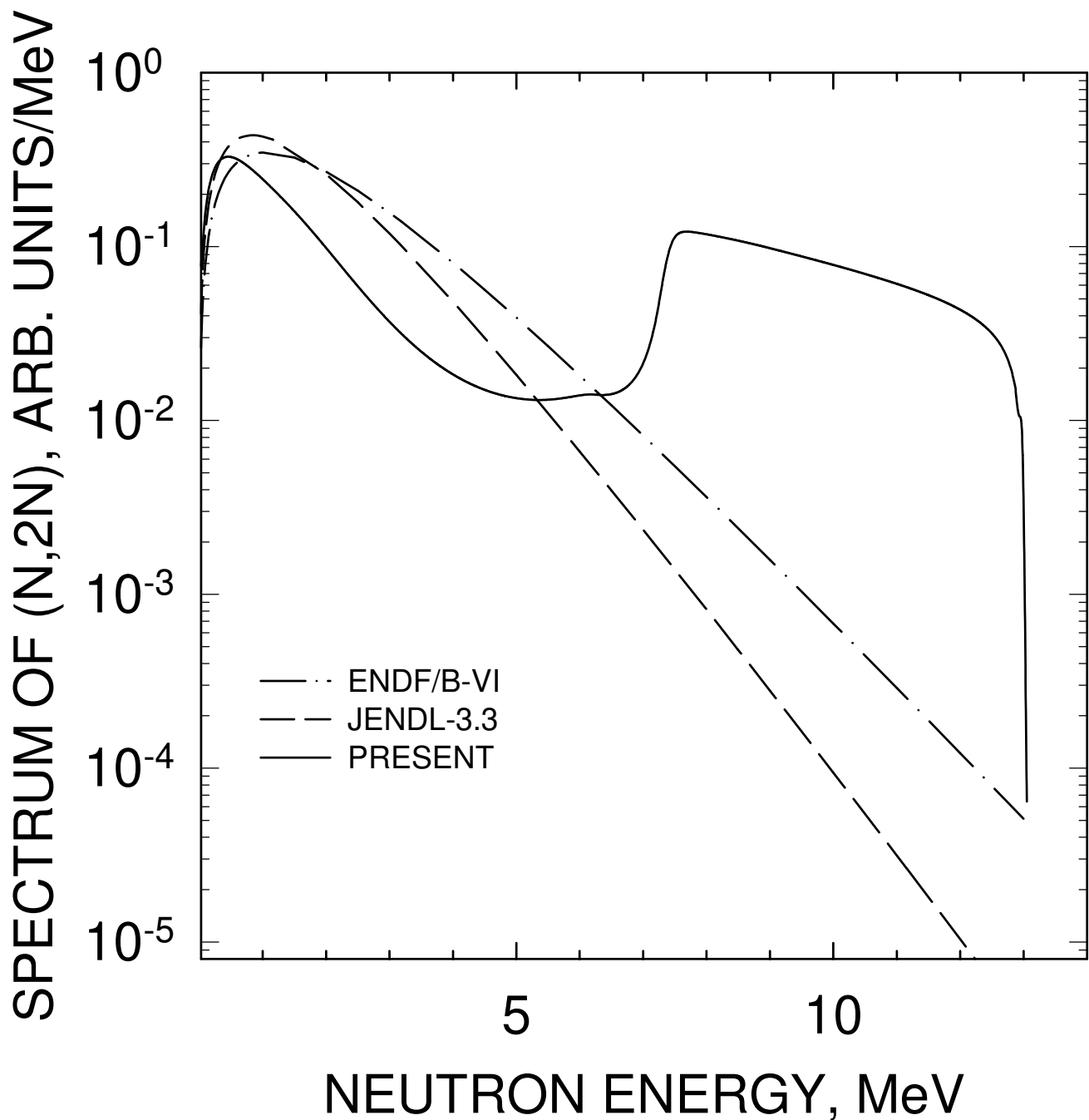


FIG. 80

^{231}Pa $E_n = 14 \text{ MeV}$
COMPARISON WITH JENDL-3.3

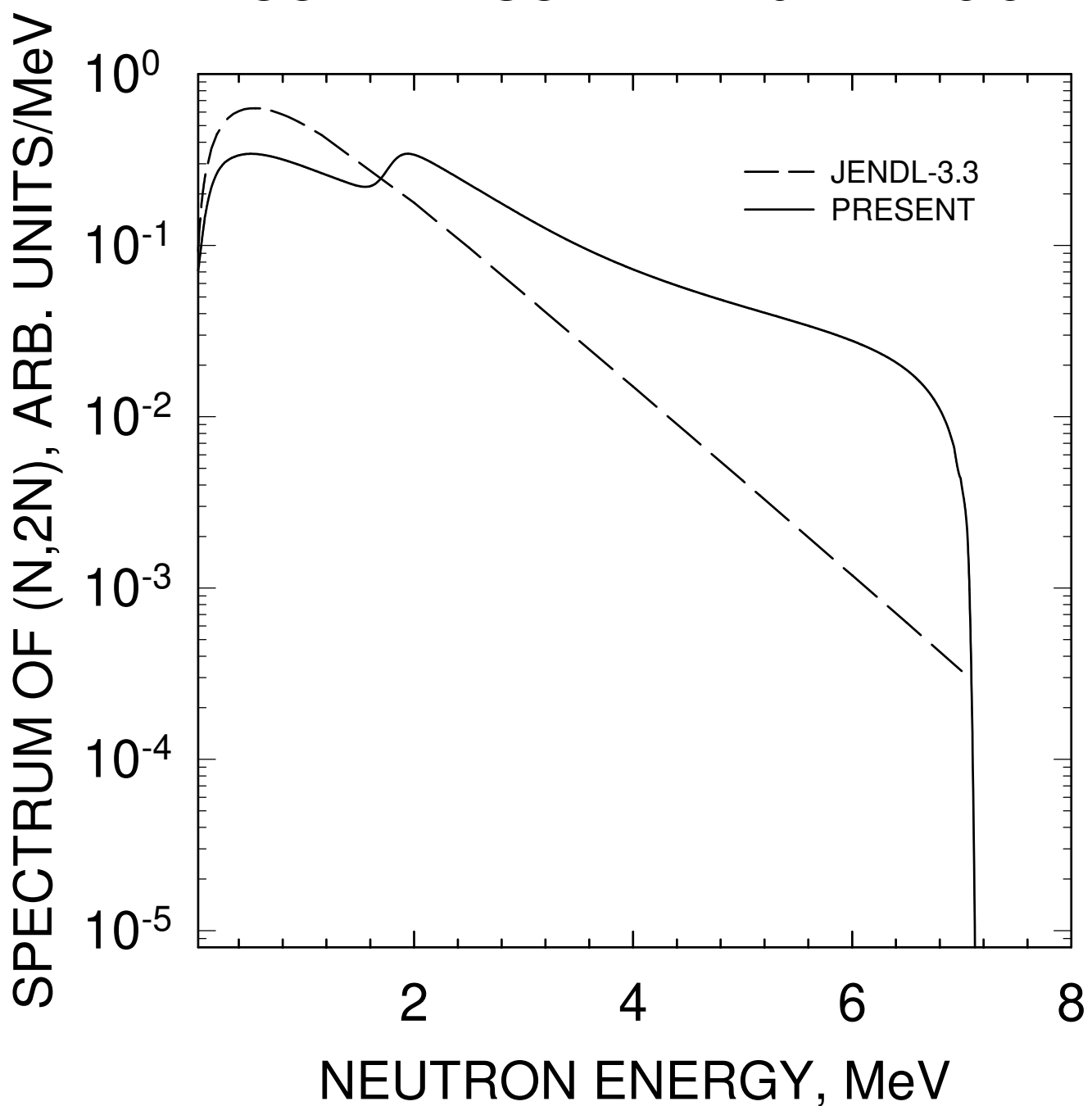


FIG. 81

^{231}Pa $E_n = 10 \text{ MeV}$
COMPARISON WITH JENDL-3.3
AND ENDF/B-VI

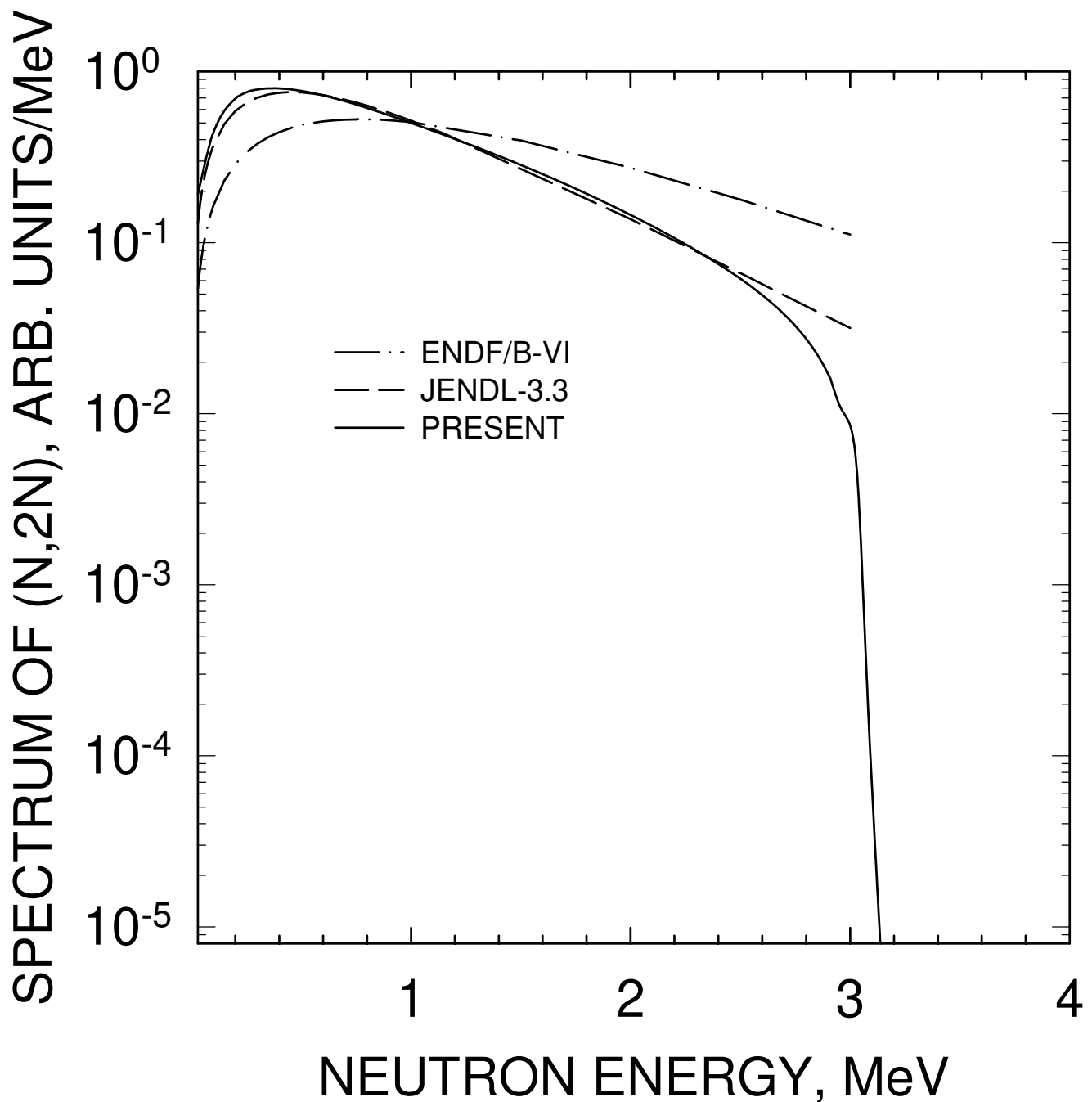


FIG. 82

^{231}Pa $E_n = 8 \text{ MeV}$
COMPARISON WITH JENDL-3.3

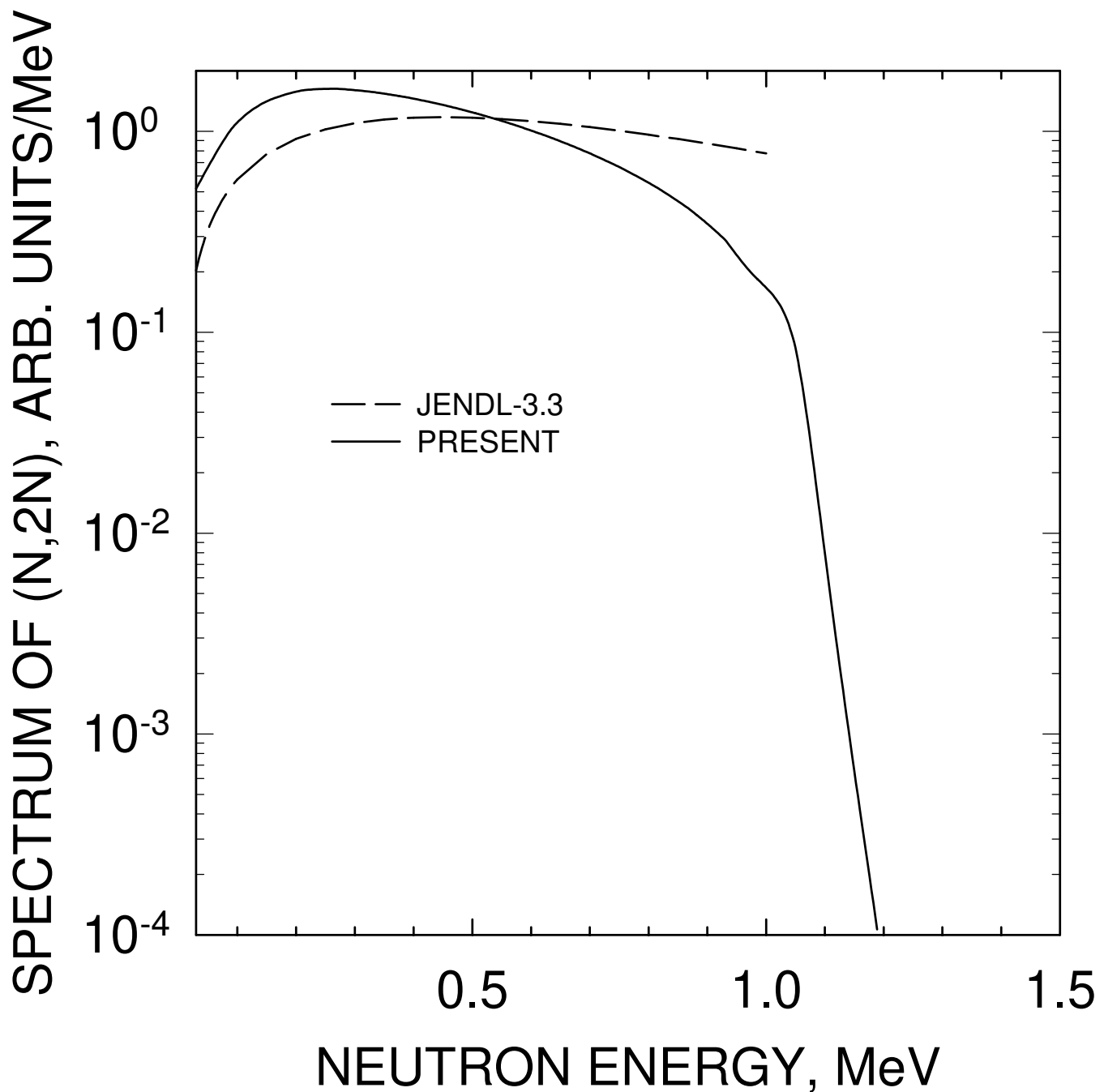


FIG. 83

^{231}Pa $E_n = 20 \text{ MeV}$
COMPARISON WITH JENDL-3.3
AND ENDF/B-VI

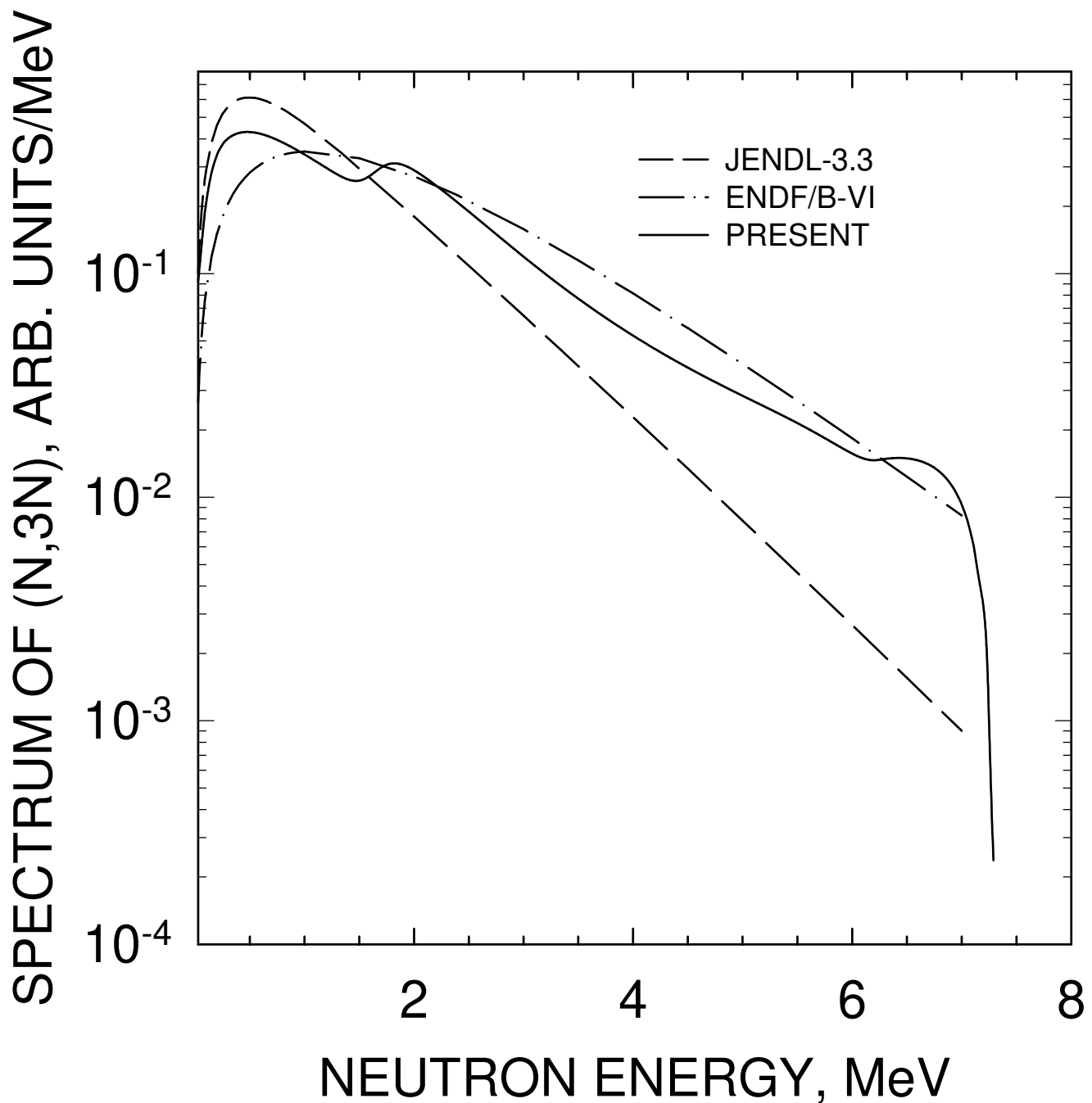


FIG. 84

^{231}Pa $E_n = 14 \text{ MeV}$
COMPARISON WITH JENDL-3.3
AND ENDF/B-VI

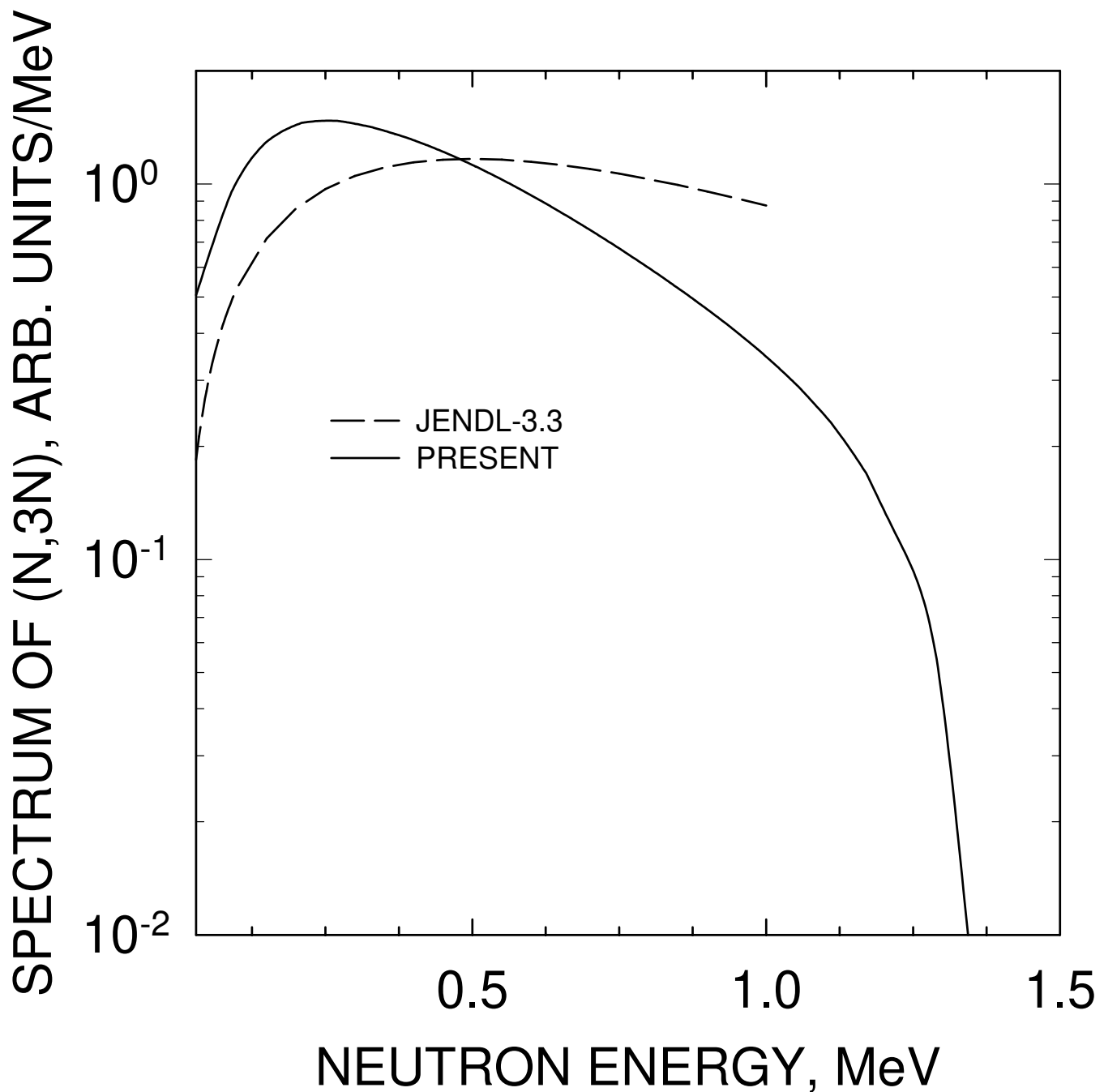


FIG. 85

Nuclear Data Section
International Atomic Energy Agency
P.O. Box 100
A-1400 Vienna
Austria

e-mail: services@iaeand.iaea.org
fax: (43-1) 26007
cable: INATOM VIENNA
telex: 1-12645
telephone: (43-1) 2600-21710

Online: TELNET or FTP: iaeand.iaea.org
username: IAEANDS for interactive Nuclear Data Information System
usernames: ANONYMOUS for FTP file transfer;
FENDL2 for FTP file transfer of FENDL-2.0;
RIPL for FTP file transfer of RIPL;
NDSOOL for FTP access to files saved in "NDIS" Telnet session.
Web: <http://www-nds.iaea.org>
